

# Modeling and experimentation of conductive and radiative transfer through heterogeneous insulators in high-flux environments

**Thèse N° 7273**

Présentée le 14 novembre 2019

à la Faculté des sciences et techniques de l'ingénieur

Laboratoire de la science et de l'ingénierie de l'énergie renouvelable

Programme doctoral en énergie

pour l'obtention du grade de Docteur ès Sciences

par

**Jérémy Raphaël MORA-MONTEROS**

Acceptée sur proposition du jury

Prof. D. Dujic, président du jury

Prof. S. Haussener, directrice de thèse

Dr J. Randrianalisoa, rapporteur

Prof. N. Ozalp, rapporteuse

Dr S. Mischler, rapporteur

2019





# Acknowledgements - Remerciements

First, I would like to thank my supervisor, Sophia, for helping me learn how to grow in the world of academics. Thank you for giving me the opportunity to do my research in your lab, especially with the nice piece of equipment that is the HFSS. I think it is fair to say that even though my time in your lab has been tough at times, I feel strong and ready to face what is coming next.

Pénélope, you gave me the chance to start this adventure in research. I had a really good time in your lab. You know how to choose colleagues, sometimes for the worse -but we laughed about it- sometimes for the better.

I would like to acknowledge the members of my thesis jury, Dr. Jaona Randrianalisoa, Prof. Nesrin Ozalp and Dr. Stefano Mischler and Prof. Drazen Dujic, who kindly read and evaluated my work, providing insightful feedback.

I would also like to thank my colleagues. Nikhil and Elise, even though you left the lab a while ago, I have been lucky to spend really nice times with you two. I remember when you were trying to hide that you were together in Paris. Now as a married couple, it looks like you guys are having an amazing journey together. Thanks to all my more recent colleagues, especially Nithin and Sarah for creating such a nice atmosphere in the lab. Sarah, thank you for supporting me emotionally when I needed it. Alexandre, I am sorry to have bothered you these last few months, I must have been really annoying. Sorry for that and thanks for the support. Clemens, thank you for everything. You helped me go through tough times as we worked together. You help me believe that I would succeed and finally bring the ship home!

I would like to acknowledge EPFL's support through the use of the facilities of its Scientific IT and Application Support Center. Alessandro Turchi, Bernt Helber, Vincent Leroy and Thierry Magin (the VKI team) for their support and collaboration on the AblaRadAbla project. Jean Lachaud for discussions about PATO. Valentine Magnin and Stefano Mischler for their work at the Tribology and Interfacial Chemistry group (TIC) on ZURAM material analyses for the AblaRadAbla project. de Cavis (Philip Sturzenegger and Urs Gonzenbach) for providing me with ceramic foams and the discussions for ceramic foams results analyses. Thomas Rothermel and Christian Zuber for providing the ZURAM material.

Je voudrais remercier ma belle famille, Sylvie, Jean-Phi, Guillaume et Damien. Vous avez été depuis plus de 12 ans d'un support inconditionnel dans la vie de tous les jours que je partage avec Delphine. Merci de m'avoir fait sentir que je faisais parti de la famille dès le début.

Je remercie aussi ma famille. Mes parents, Monica et Christophe, je serais loin d'être celui que je suis aujourd'hui sans vous. Vous m'avez donné tout l'amour et l'éducation qui m'ont forgé

## Acknowledgements - Remerciements

---

et mené à fonder une famille tout en poursuivant les étoiles. Mon frère, Loïc, et ma soeur, Maëlle, merci aussi à vous. Merci de me faire confiance, je serais toujours là pour vous.

Merci à mes amis, qui sont un peu comme ma famille aussi. Damien et Alevtina, les modèles. Charlène et Diede, toujours de bonne humeur pour nous recevoir à Bâle. Nos chers voisin, devenus aujourd'hui amis, Charlotte et Jean-Marc, merci pour les encouragements ces derniers temps. Noémie et Frank-Jourdan, même si vous êtes toujours à cent à l'heure, pour moi vous êtes un havre de paix.

Boris, Bobo, VZ, Bobby. Je ne sais pas qui supporte qui dans cette histoire. C'est sûrement à celui qui voudra avoir le dernier mot. Cela fait 25 ans qu'on se motive l'un l'autre pour atteindre des sommets. C'est pas si mal ce qu'on est arrivé à faire, non? Merci pour ton soutien, tes encouragements ces derniers temps. Merci d'être mon ami. Je te dois une bonne bouffe pour avoir si bien lu ma thèse! 25 ans et je n'ai qu'une chose à dire: Pourvu que ça dure!

Delphine, Maman. Ma réussite ne serait pas possible sans toi. Ton soutien est sans fin. Tout l'amour que tu déverse dans notre famille est inépuisable. Cette thèse est une réussite pour moi, mais la plus grande des réussites c'est tout ce qu'on a pu construire tous les deux. Notre fille est un soleil qui nous illumine chaque jour. Et je suis plus qu'heureux d'avoir rencontré notre fils Noam, qui a déjà pu nous gratifier de ses premiers sourires.

Et enfin, ma petite Éléna, ma puce d'amour, j'écris un petit mot pour toi pour quand tu sauras lire. Tu es la dernière que je remercie, alors Maman va être jalouse. Tu es la plus gentille des filles du monde. Je te remercie aussi car grâce à toi j'oublie tous mes soucis.

*Attalens, le 30 Septembre 2019*

Jérémy Mora-Monteros

This work is supported by the Swiss Commission for Technology and Innovation (CTI), the State Secretariat for Education, Research and Innovation and the European Space Agency through contract no. 4000113101/15/NL/RA with the von Karman Institute for Fluid Dynamics on "Ablation and Radiation in the presence of Light Ablators" (AblaRadAbla).

# Abstract

Heterogeneous materials are used in a wide range of applications involving high heat flux environments such as concentrated solar reactors, high-temperature furnaces, or thermal protection systems of space vehicles. The thermal response of heterogeneous materials is driven by coupled conduction, convection, and radiation heat transfer and, depending on the material composition, also by thermochemical processes. The thermal properties of such materials can be determined by using experimental methods. One challenge lies in the choice of the modeling approach to consider radiative transport. Modeling the heterogeneous media by an equivalent homogeneous media with an effective thermal conductivity (ETC) accounting for a radiative transport is computationally simple but requires accurate knowledge of the temperature-dependent ETC and can lead to errors. To provide more accuracy, models that solve the radiative transfer equation (RTE) separately from conduction are used. This type of method is computationally intensive and it is unclear in which condition one approach or the other is needed.

First, a novel combined experimental-numerical method, that allows for the determination of the ETC for a large temperature range (288 K to 1473 K) utilizing one experiment only, is implemented. The experiment includes transient and locally-resolved temperature measurements of porous ceramics samples with different porosities exposed to high radiative fluxes in EPFL's high-flux solar simulator (HFSS). The pseudo-inverse methodology uses the porous material analysis toolbox based on OpenFOAM (PATO).

Second, a more advanced thermal response model calculating the radiative contribution by the separate solution of the RTE and its contribution to the energy equation through a source term is implemented. The development of this PATORAC algorithm includes the implementation of a path-length based Monte-Carlo (MC) ray-tracing code. The MC solver was coupled to the energy equation solver through specifically coded boundary conditions and source terms. A quantitative comparison between the two methods is given as a function of the transport properties, morphology, and boundary conditions. Quantitative guidelines are established to provide recommendations for the choice of the most adapted approach.

Finally, the developed tools and guidelines are applied to a carbon-phenolic composite material (ZURAM) that is used as a thermal protection system in space applications. Tests performed with ZURAM samples in a high convective flux environment (VKI's Plasmatron) and in EPFL's HFSS are numerically rebuilt using the ETC method, providing information on the temperature-dependent thermal diffusivity.

The investigations show that the pseudo inverse approach developed for the determination of

## Abstract

---

the temperature-dependent ETC is useful for conditions that are not dominated by incoming radiation. It should be used to simulate the thermal behavior of heterogeneous materials that present relatively high conductivities and extinction coefficient. The coupled radiation-conduction approach, on the other hand, must be used in conditions with low-absorbing and low-conducting media in highly radiating environments. The comparison between tests in VKI's Plasmatron and the HFSS widens the testing possibilities of such materials. Indeed, facilities like the HFSS are easier to implement and prove to be an alternative for space composites testing.

KEYWORDS: effective thermal conductivity, radiation, Monte-Carlo, radiation-conduction coupling, high flux solar simulator, numerical simulations, space application composite materials.

# Résumé

Les matériaux hétérogènes sont utilisés pour un large panel d'applications impliquant des environnements à hauts flux de chaleur tels que les réacteurs à énergie solaire concentrée, les fours à haute température, ou les systèmes de protection thermique des véhicules pour l'exploration spatiale. Le transfert de chaleur dans les matériaux hétérogènes se fait par conduction, convection, et rayonnement et, en fonction de leur composition chimique, également par des réactions chimiques. Les propriétés thermiques de ces matériaux peuvent être déterminées grâce à des méthodes expérimentales. Un des défis se situe dans le choix de l'approche à adopter pour modéliser le transfert radiatif. La modélisation d'un milieu hétérogène par un milieu homogène équivalent ayant une conductivité thermique effective est numériquement simple mais elle nécessite la connaissance de cette conductivité thermique effective en fonction de la température. De plus, cette méthode peut conduire à d'importantes erreurs. Pour palier à cette incertitude, des modèles considérant la conduction et le rayonnement séparément sont utilisés. Le rayonnement est pris en compte en résolvant l'équation de transfert radiatif. Ce type d'approche est coûteux en ressources de calcul. La limite déterminant les conditions dans lesquelles l'une ou l'autre méthode devrait être utilisée est mal définie à ce jour.

Dans un premier temps, une méthode innovante combinant expériences et simulations numériques est développée. Elle permet de déterminer la conductivité thermique effective d'un matériau pour un intervalle de température considérable (288 K à 1473 K) en utilisant les données d'une seule expérience. Cette expérience intègre la mesure de la température en régime transitoire et à plusieurs positions à l'intérieur d'échantillons de mousses céramiques de porosités différentes exposés à de hauts flux de chaleur radiatifs dans le simulateur solaire à haut flux de l'EPFL. La méthode utilise PATO, un outil de simulation des matériaux poreux basé sur OpenFOAM.

Ensuite, un modèle plus avancé de la réponse thermique est implémenté. Il calcule la contribution du rayonnement au transfert de chaleur en résolvant séparément l'équation de transfert radiatif et en incorporant la solution dans l'équation de conservation de l'énergie via un terme source. L'implémentation de cet algorithme, appelé PATORAC, inclut le développement d'un code Monte-Carlo de tracé de rayons basé sur la longueur du trajet d'un rayon. Le solveur Monte-Carlo est couplé à l'équation d'énergie à l'aide d'un terme source et de conditions aux bords spécifiques. Une comparaison quantitative des deux méthodes est effectuée en prenant en compte les propriétés de transport et la morphologie du matériau, ainsi que les conditions aux limites. Cette analyse fournit des lignes directrices pour orienter le choix de la meilleure méthode à adopter pour la simulation du transfert de chaleur global.

Enfin, les outils et lignes directrices mis en place sont appliqués à un matériau composite de carbone et de résine phénolique, appelé ZURAM, qui est utilisé comme bouclier thermique dans des applications pour l'exploration spatiale. Des essais réalisés sur le matériau ZURAM dans un environnement à haut flux de chaleur convectif (le Plasmatron à l'institut von Karman (VKI)) et dans le simulateur solaire à l'EPFL sont reproduits numériquement en utilisant le modèle qui considère une conductivité thermique effective. Ces tests permettent d'élargir les connaissances sur la diffusivité thermique du matériau ZURAM en fonction de la température. Cette étude montre que la méthode pseudo inverse développée pour l'évaluation de la conductivité thermique effective en fonction de la température est adaptée pour des conditions qui ne sont pas dominées par le transfert de chaleur radiatif dû à l'illumination directe. La méthode utilisant la conductivité effective peut donc être utilisée pour simuler la réponse thermique des matériaux hétérogènes dont la conductivité intrinsèque et le coefficient d'extinction sont relativement élevés. A l'inverse, l'approche couplée, où le rayonnement et la conduction sont traités séparément, doit être utilisée dans le cas de milieux peu absorbants et peu conducteurs placés dans des environnements où le rayonnement est important. La comparaison entre les essais dans le Plasmatron du VKI et ceux effectués dans le simulateur solaire élargit les possibilités d'expérimentation de matériaux tels que ZURAM. En effet, les installations telles que le simulateur solaire sont plus facilement installés et elles présentent une alternative intéressante pour tester les matériaux composites notamment pour les applications spatiales.

**MOTS CLÉS :** conductivité thermique effective, rayonnement, Monte-Carlo, couplage rayonnement-conduction, simulateur solaire à haut flux, simulations numériques, matériaux composites pour les applications spatiales.

# Contents

<b>Acknowledgements - Remerciements</b>	<b>iii</b>
<b>Abstract/Résumé)</b>	<b>v</b>
<b>List of figures</b>	<b>xvii</b>
<b>List of tables</b>	<b>xix</b>
<b>Nomenclature</b>	<b>xix</b>
<b>1 Introduction</b>	<b>1</b>
1.1 Aim . . . . .	6
1.2 Objectives . . . . .	6
1.3 Scope . . . . .	7
1.4 Thesis Outline . . . . .	7
<b>2 Experimental tools</b>	<b>9</b>
2.1 High-Flux Solar Simulator testing . . . . .	9
2.1.1 HFSS principle and characteristics . . . . .	9
2.1.2 Flux measurements . . . . .	10
2.1.3 Sample holder . . . . .	14
2.1.4 Thermocouples measurements . . . . .	14
2.1.5 Surface temperature measurements: IR Camera . . . . .	16
2.1.6 Environmental chamber . . . . .	17
2.2 Convection flux testing . . . . .	18
2.3 Material Analyses . . . . .	19
2.3.1 Thermogravimetric analysis . . . . .	19
2.3.2 Scanning electron microscope . . . . .	20
2.3.3 X-ray Photoelectron Spectroscopy . . . . .	21
2.4 Materials . . . . .	21
<b>3 Numerical methods and models</b>	<b>23</b>
3.1 Energy conservation equation: Porous material Analysis Toolbox (PATO) . . . . .	23
3.1.1 Conservation of mass . . . . .	23
3.1.2 Conservation of momentum . . . . .	24

## Contents

---

3.1.3	Conservation of energy . . . . .	24
3.1.4	Simplifications for modeling ceramic foams thermal response . . . . .	25
3.1.5	Spatially resolved time dependent boundary condition . . . . .	25
3.2	Pseudo-inverse methodology for determining effective thermal conductivity (ETC) . . . . .	25
3.3	Radiative heat transfer: Monte-Carlo radiation code . . . . .	28
3.3.1	Implementation . . . . .	30
3.3.2	High performance computing considerations . . . . .	36
3.4	Radiation-conduction coupling algorithm: PATORAC . . . . .	37
<b>4</b>	<b>Effective conductivity of highly porous ceramics in a radiative environment</b>	<b>39</b>
4.1	Sample properties . . . . .	39
4.2	Methodology complements . . . . .	41
4.2.1	Boundary conditions . . . . .	42
4.2.2	Numerical considerations . . . . .	42
4.3	Results and discussion . . . . .	43
4.3.1	Validation of computational model . . . . .	43
4.3.2	Influence of porosity . . . . .	45
4.3.3	Influence of coating layer and magnitude of incoming radiative heat flux . . . . .	45
4.3.4	Material Comparison . . . . .	47
4.4	Conclusions . . . . .	50
<b>5</b>	<b>Coupled conduction-radiation modeling</b>	<b>53</b>
5.1	Methodology complements . . . . .	53
5.1.1	Initial and boundary conditions . . . . .	55
5.2	Results and discussion . . . . .	57
5.2.1	Comparison of ETC model to coupled model results . . . . .	57
5.2.2	Sensitivity study . . . . .	62
5.3	Conclusions . . . . .	67
<b>6</b>	<b>Numerical rebuilding of ZURAM high temperature tests</b>	<b>71</b>
6.1	VKI Plasmatron tested ZURAM samples . . . . .	71
6.1.1	ZURAM material . . . . .	71
6.1.2	Experimental results . . . . .	71
6.1.3	Material analyses . . . . .	73
6.1.4	Numerical rebuilding of experiments . . . . .	81
6.2	HFSS tested ZURAM . . . . .	90
6.2.1	Sample description and conditions . . . . .	90
6.3	Conclusions . . . . .	94
<b>7</b>	<b>Summary and Outlook</b>	<b>97</b>
7.1	Summary . . . . .	97
7.2	Achievements . . . . .	99
7.3	Outlook . . . . .	99



<b>Appendix</b>	<b>103</b>
A    Manufacturing drawings . . . . .	103
B    Temperature profiles for conduction-radiation modeling . . . . .	105
B.1    Temperature dependent bulk conductivity, 1449.5 kW m <sup>-2</sup> peak heat flux value . . . . .	105
B.2    Temperature independent thermal properties, 1449.5 kW m <sup>-2</sup> peak heat flux value . . . . .	110
B.3    Temperature dependent bulk conductivity, 2222.6 kW m <sup>-2</sup> peak heat flux value . . . . .	113
B.4    Temperature independent thermal properties, 2222.6 kW m <sup>-2</sup> peak heat flux value . . . . .	118
<b>Bibliography</b>	<b>121</b>
<b>Curriculum Vitae</b>	<b>131</b>



# List of Figures

2.1	Schematics of (a) the front view and (b) a cross-section view of the HFSS. (a) shows the numbering of lamps. (b) introduces the dimensions, the position of the focal plane and the CCD camera (see section 2.1.2), and the two main elements that compose one lamp of this facility. . . . .	11
2.2	Example of radiative flux calibration from (a) a GS image to (b) a full radiative heat flux map obtained using lamps 1, 2, and 3. . . . .	12
2.3	Photo of the water-cooled sample holder. . . . .	14
2.4	Borosilicate and aluminium chamber sections. . . . .	19
2.5	TGA set-up consisting of a furnace, a balance and a gas system which are computer controlled. . . . .	20
3.1	Iterative process flow chart utilizing experiments and computational model to determine the temperature-dependent ETC. . . . .	27
3.2	Path-length Monte-Carlo Algorithm. . . . .	33
3.3	TraceRay function algorithm. . . . .	35
3.4	PATORAC coupled transient algorithm. . . . .	38
4.1	SEM images of the studied samples surfaces: (a) U92, (b) U75, (c) U81, (d) U88, (e) C88. . . . .	40
4.2	Shape and size of the investigated samples. . . . .	41
4.3	Comparison between numerical data and thermocouple measurements at five different depths, for the sample U88 that was exposed to a $1 \text{ MWm}^{-2}$ peak radiative flux. . . . .	44
4.4	Comparison of the ETCs of Alumino-silicate samples U75, U81, and U88 in function of (a) the temperature, and (b) the solid fraction at six different temperatures. . . . .	46
4.5	Influence of the boundary condition on the effective conductivity. . . . .	47
4.6	Temperature-dependent bulk conductivity ranges for (a) pure alumina and (b) alumino-silicate. . . . .	48
4.7	Comparison of the ETC of (a) U92 sample and (b) U88 sample, exposed to the same levels of peak radiative heat flux ( $1 \text{ MWm}^{-2}$ ). . . . .	49
5.1	Bulk thermal conductivity and heat capacity of alumina . . . . .	54

## List of Figures

5.2	Radiative flux distribution on the 40x40 mm exposed surface for the study of radiation-conduction coupling. . . . .	56
5.3	BC types for comparison between the ETC and PATORAC models . . . . .	57
5.4	Comparison of results obtained with the ETC and the PATORAC model using flux and temperature BCs for a sample with a porosity of 95 % and a bulk conductivity factor $F_{k,bulk}$ of 0.125. . . . .	58
5.5	Comparison of results obtained with the ETC and the PATORAC model using flux and temperature BCs for a sample with a porosity of 95 % and a bulk conductivity factor $F_{k,bulk}$ of 1.0. . . . .	59
5.6	Comparison of results obtained with the ETC and the PATORAC model considering the radiative flux BC on the Monte-Carlo side for a sample with a porosity of 95 % and a bulk conductivity factor $F_{k,bulk}$ of 0.125. . . . .	60
5.7	Comparison of results obtained with the ETC and the PATORAC model considering the radiative flux BC on the Monte-Carlo side for a sample with a porosity of 95 % and a bulk conductivity factor $F_{k,bulk}$ of 1.0. . . . .	61
5.8	Pictures of a sample exposed in the HFSS to a high heat flux than induced the degradation of the sample. . . . .	62
5.9	Maps of $R^2$ values in function of the studied ranges of $F_{k,bulk}$ and $\beta$ , for porosities of (a) 95 %, (b) 90 %, (c) 85 %, (d) 80 %, and (e) 75 %. The peak value of incoming heat flux was $1449.5 \text{ kWm}^{-2}$ . . . . .	64
5.10	Comparison of $R^2$ values maps between the (a) temperature dependent and (b) constant bulk conductivity cases for a porosity of 85 %. The peak value of incoming heat flux was $1449.5 \text{ kWm}^{-2}$ . . . . .	65
5.11	Comparison of $R^2$ values maps between the (a) lower flux ( $1449.5 \text{ kWm}^{-2}$ ) and (b) higher flux ( $2222.6 \text{ kWm}^{-2}$ ) cases for a porosity of 75 %. . . . .	66
5.12	Comparison of (a), (c) and (e) $R^2$ values map obtained for a sample porosity of 75, 85, and 95 % respectively and an incoming peak heat flux value of $1449.5 \text{ Wm}^{-2}$ to (b), (d) and (f) respective radiation-to-conduction factor values maps. . . . .	67
6.1	Drawing and schematics showing (a) the sample shape and dimensions, (b) and (c) the TCs positions reported to the same plane. . . . .	72
6.2	Temperature profiles (a) at stagnation points in function of time and (b) along the surfaces in function of the distance to central axis at the end of the heating phases for ZU1 and ZU3 cases. The dots in (a) identify the times when the temperature profiles represented in (b) were taken. . . . .	73
6.3	Surface temperature distributions for (a) ZU1 and (b) ZU3 cases recorded at the end of the heating phase (82 s for ZU1, 10 s for ZU1). . . . .	74
6.4	(a) Slice of sample to be cut into 6 pieces for TGA measurements. (b) Cut of sample ZU1 (c) Cut of sample ZU3 and cutting location for TGA measurements. . . . .	75
6.5	TGA results for ZU3 test sample showing the evolution of the normalised weight in function of (a) the temperature and (b) the time. (c) gives the normalised weight time derivative in function of time. . . . .	76

6.6	(a) Resin content and (b) residual weight through the thickness of sample corresponding to slice on the red line of sample ZU3. . . . .	77
6.7	Atomic concentratio ratio in function of the distance from the surface of the model on the red line (see Figure 6.4). The dashed lines correspond to virgin values. . . . .	79
6.8	SEM images at low magnification (x50) of ZU3 sample along the sample depth on the red line defined in Figure 6.4. . . . .	79
6.9	Comparison of the TGA residual weight (in blue) and the XPS C/C+O (in light red) profiles through the thickness of sample ZU3 on the red line. The vertical black dashed line corresponds to the char thickness determined with SEM. . .	80
6.10	ZURAM material thermal properties. (a) Specific heat capacity for virgin and char states. (b) Effective thermal conductivity for virgin and char states. . . . .	83
6.11	Geometry and mesh of the test sample. (a) View of the wedge used for 2D-axisymmetrical simulations. . . . .	84
6.12	Comparison of thermocouple measurements in ZU1 sample (lines with symbols) to numerical temperature profiles (solid lines) at the corresponding depths, using the database thermal conductivity. . . . .	85
6.13	Comparison of thermocouple measurements in ZU1 sample (lines with symbols) to numerical temperature profiles (solid lines) at the corresponding depths, using the database thermal conductivity multiplied by a factor of 0.55. . . . .	86
6.14	Comparison of thermocouple measurements in ZU3 sample (lines with symbols) to numerical temperature profiles (solid lines) at the corresponding depths, using the database thermal conductivity. . . . .	88
6.15	Comparison of thermocouple measurements in ZU3 sample (lines with symbols) to numerical temperature profiles (solid lines) at the corresponding depths, using the database thermal conductivity multiplied by a factor of 0.55. . . . .	89
6.16	Comparison of numerical char degree values with normalised residual weight in TGA measurements for ZU3 case. . . . .	90
6.17	Flux distribution and magnitude to which the ZURAM was exposed in the HFSS	91
6.18	Temperature measurements of a ZURAM test in the HFSS at a peak heat flux of $1.004 \text{ MW m}^{-2}$ . . . . .	92
6.19	Comparison of numerical results (solid lines) to experimental TC data (in dashed lines), when a radiative heat flux BC with a peak heat flux of $1.004 \text{ MW m}^{-2}$ . . .	93
6.20	Comparison of numerical results (solid lines) to experimental TC data (in dashed lines), when a radiative heat flux BC with a peak heat flux of $1.004 \text{ MW m}^{-2}$ . Radiative heat fluxes BCs, which detailed values can be found in Table 6.7 were also applied on the side faces. . . . .	94
A.1	Technical drawing of holes to be machined in tested samples. The holes are arranged according to the thermocouples arrangement fixed by the thermocouple mounting block (see Section 2.1.3) . . . . .	103
A.2	Spherical chamber with ISO160 flanged ends and a KF40 flange window port .	104

## List of Figures

---

B.3	Temperature profiles obtained with the PATORAC algorithm with a peak value of incoming radiative heat flux of $1449.5 \text{ kW m}^{-2}$ through a 95 % porosity sample with temperature dependent thermal properties. . . . .	105
B.4	Temperature profiles obtained with the PATORAC algorithm with a peak value of incoming radiative heat flux of $1449.5 \text{ kW m}^{-2}$ through a 90 % porosity sample with temperature dependent thermal properties. . . . .	106
B.5	Temperature profiles obtained with the PATORAC algorithm with a peak value of incoming radiative heat flux of $1449.5 \text{ kW m}^{-2}$ through a 85 % porosity sample with temperature dependent thermal properties. . . . .	107
B.6	Temperature profiles obtained with the PATORAC algorithm with a peak value of incoming radiative heat flux of $1449.5 \text{ kW m}^{-2}$ through a 80 % porosity sample with temperature dependent thermal properties. . . . .	108
B.7	Temperature profiles obtained with the PATORAC algorithm with a peak value of incoming radiative heat flux of $1449.5 \text{ kW m}^{-2}$ through a 75 % porosity sample with temperature dependent thermal properties. . . . .	109
B.8	Temperature profiles obtained with the PATORAC algorithm with a peak value of incoming radiative heat flux of $1449.5 \text{ kW m}^{-2}$ through a 95 % porosity sample with temperature independent thermal properties. . . . .	110
B.9	Temperature profiles obtained with the PATORAC algorithm with a peak value of incoming radiative heat flux of $1449.5 \text{ kW m}^{-2}$ through a 85 % porosity sample with temperature independent thermal properties. . . . .	111
B.10	Temperature profiles obtained with the PATORAC algorithm with a peak value of incoming radiative heat flux of $1449.5 \text{ kW m}^{-2}$ through a 75 % porosity sample with temperature independent thermal properties. . . . .	112
B.11	Temperature profiles obtained with the PATORAC algorithm with a peak value of incoming radiative heat flux of $2222.6 \text{ kW m}^{-2}$ through a 95 % porosity sample with temperature dependent thermal properties. . . . .	113
B.12	Temperature profiles obtained with the PATORAC algorithm with a peak value of incoming radiative heat flux of $2222.6 \text{ kW m}^{-2}$ through a 90 % porosity sample with temperature dependent thermal properties. . . . .	114
B.13	Temperature profiles obtained with the PATORAC algorithm with a peak value of incoming radiative heat flux of $2222.6 \text{ kW m}^{-2}$ through a 85 % porosity sample with temperature dependent thermal properties. . . . .	115
B.14	Temperature profiles obtained with the PATORAC algorithm with a peak value of incoming radiative heat flux of $2222.6 \text{ kW m}^{-2}$ through a 80 % porosity sample with temperature dependent thermal properties. . . . .	116
B.15	Temperature profiles obtained with the PATORAC algorithm with a peak value of incoming radiative heat flux of $2222.6 \text{ kW m}^{-2}$ through a 75 % porosity sample with temperature dependent thermal properties. . . . .	117
B.16	Temperature profiles obtained with the PATORAC algorithm with a peak value of incoming radiative heat flux of $2222.6 \text{ kW m}^{-2}$ through a 95 % porosity sample with temperature independent thermal properties. . . . .	118

B.17 Temperature profiles obtained with the PATORAC algorithm with a peak value of incoming radiative heat flux of $2222.6 \text{ kW m}^{-2}$ through a 85 % porosity sample with temperature independent thermal properties. . . . .	119
B.18 Temperature profiles obtained with the PATORAC algorithm with a peak value of incoming radiative heat flux of $2222.6 \text{ kW m}^{-2}$ through a 75 % porosity sample with temperature independent thermal properties. . . . .	120





# List of Tables

2.1	Environmental chamber characteristic dimensions. . . . .	18
4.1	The list of experimentally investigated sample types, flux levels, densities, porosities, typical extinction coefficient $\beta$ , and the abbreviations used for the various sample types. . . . .	40
4.2	The experimental matrix investigated, indicating what sample comparison was done and what effect on ETC could therefore be investigated. . . . .	41
4.3	Summary of values representative of the goodness of fit for temperature analyses for the five other types of sample presented in this work. . . . .	44
6.1	VKI Plasmatron test conditions for the two studied samples: ZU1 (low flux, long exposure time) and ZU3 (high flux, short exposure time) . . . . .	72
6.2	Probes/thermocouple positions for ZU1 and ZU3 cases: first row distance from sample bottom, second row distance from centre axis. All values are in mm . . .	73
6.3	XPS Atomic concentrations at different distances from the surface. . . . .	78
6.4	Char layer thicknesses (in mm) in the red line of sample ZU3 according to each method. . . . .	80
6.5	Summary of the ZURAM material input data to run PATO cases. . . . .	82
6.6	Pyrolysis reaction data for ZURAM . . . . .	82
6.7	Flux magnitudes set on the sides faces of the ZURAM sample to account for irradiation on the sides due to the small size of the sample. . . . .	93



# Nomenclature

$A$	Arrhenius law pre-exponential factor	
$A_{\text{face}}$	Cell face area	$\text{m}^2$
$D_p$	Pore diameter	$\text{m}$
$E$	Arrhenius' law activation energy	$\text{J mol}^{-1}$
$F_i$	Mass loss fraction due to pyrolysis reaction $i$	
$F_{k,\text{bulk}}$	Bulk conductivity factor	
$I$	Volume averaged radiative intensity	$\text{W m}^{-3} \text{sr}^{-1}$
$I_b$	Volume averaged blackbody radiative intensity in vacuum	$\text{W m}^{-3} \text{sr}^{-1}$
$L$	Sample length	$\text{m}$
$L_{\text{ext}}$	Extinction length	$\text{m}$
$N_g$	Number of gaseous species	
$N_{\text{rays}}$	Number of rays	
$N_p$	Number of pyrolysis reactions	
$P$	Power	$\text{W}$
$P_{\text{el}}$	Electric power delivered to inductive torch	$\text{W}$
$R$	Random number	
$R^2$	Coefficient of determination, $R$ -squared	
$T$	Temperature	$\text{K}$
$\dot{Q}$	Heating power per unit length	$\text{W m}^{-1}$
$\hat{\mathbf{s}}$	Unit directional vector	
$\mathbf{k}_{\text{eff}}$	Effective conductivity tensor	$\text{W m}^{-1} \text{K}^{-1}$

## Nomenclature

---

$\mathbf{r}$	Position vector	
$\mathcal{Q}_k$	Effective diffusive heat flux	$\text{J m}^{-2} \text{s}^{-1}$
$\mathcal{R}$	Universal gas constant	$\text{J K}^{-1} \text{mol}^{-1}$
$\underline{\underline{\mathbf{K}}}$	Permeability tensor	$\text{m}^2$
$d$	Distance traveled by ray in cell in ray-tracing algorithm	$\text{m}$
$d_{\text{LFA}}$	Sample thickness in laser flash analysis	$\text{m}$
$e$	Specific energy	$\text{J kg}^{-1}$
$f_v$	Volume fraction	
$f_s$	Volume ratio of a strut to the total solid volume of a cell	
$h$	Specific enthalpy	$\text{J kg}^{-1}$
$k$	Absorptive index	
$k_a$	Thermal conductivity of air	$\text{W m}^{-1} \text{K}^{-1}$
$k_b$	Bulk thermal conductivity	$\text{W m}^{-1} \text{K}^{-1}$
$k_{\text{cond}}$	Thermal conductivity for pure conduction	$\text{W m}^{-1} \text{K}^{-1}$
$k_{\text{eff}}$	Effective thermal conductivity	$\text{W m}^{-1} \text{K}^{-1}$
$k_{\text{rad}}$	Radiative thermal conductivity	$\text{W m}^{-1} \text{K}^{-1}$
$m$	Complex index of refraction	
$n$	Refractive index Time iteration counter	
$p_d$	Dynamic pressure	$\text{Pa}$
$p_s$	Static pressure	$\text{Pa}$
$q_r$	Radiative heat flux	$\text{W m}^{-2}$
$t$	Time	$\text{s}$
$t_{1/2}$	Half temperature rise time in laser flash analysis	$\text{s}$
$x_i$	$i$ -th thermocouple position	
$C$	Structure parameter	

## Greek Symbols

---

$\alpha$	Thermal diffusivity	$\text{m s}^{-2}$
$\alpha_r$	Radiant heat transfer coefficient	$\text{W m}^{-2} \text{K}^{-1}$
$\beta$	Extinction coefficient	$\text{m}^{-1}$
$\epsilon$	2-norm relative error	
$\kappa$	Absorption coefficient	$\text{m}^{-1}$
$\lambda$	Wavelength	$\text{m}$
$\mu$	Dynamic viscosity	$\text{kg m}^{-1} \text{s}^{-1}$
$\Omega$	Scattering albedo	
$\Phi$	Scattering phase function	
$\phi$	Porosity	
$\Pi$	Pyrolysis production	$\text{kg m}^{-3} \text{s}^{-1}$
$\rho$	Density	$\text{kg m}^{-3}$
$\rho_{\text{face}}$	Face reflectivity	
$\rho_{\text{wall}}$	Wall reflectivity	
$\sigma_B$	Stefan-Boltzmann constant	$\text{W m}^{-2} \text{K}^{-4}$
$\sigma_s$	Scattering coefficient	$\text{m}^{-1}$
$\tau$	Optical thickness	$\text{m}$
$\varepsilon$	Emissivity	
$\varepsilon_{\text{slope}}$	Limit slope absolute error	
$\xi$	Advancement of pyrolysis reaction	

**Subscripts**

abs	Absorbed
amb	Ambiant
b	Blackbody
cell	Relative to mesh cell
conv	Convective
cw	Cold wall

## Nomenclature

---

d	Discrete
el	Electric
em	Emitted
exp	Experimental value
f	Fibers
g	Gas phase
inc	Incoming
IR	Relative to Infrared wavelength range
lim	Limit value
mv	Virgin polymer matrix
m	Pyrolyzing matrix
ray	Relative to ray
vis	Relative to Visible wavelength range
w	Wall
$i, j$	Phase index
p	Relative to a porous material
refl	Reflected
rerad	Re-radiation

## Acronyms

AS	Alumino-silicate
BC	Boundary condition
CCD	Charged-Coupled Device
CSP	Concentrated Solar Power
CT	Computed tomography
DSC	Differential Scanning Calorimetry
ETC	Effective Thermal Conductivity
GS	Grayscale

HFSS	High Flux Solar Simulator
HPC	High performance computing
IR	Infrared
LFA	Laser Flash Analysis
LHS	Left hand side
LWIR	Long Wave Infrared
MC	Monte-Carlo
MPI	Message passing interface
PATO	Porous material Analysis Toolbox
PICA	Phenolic Impregnated Carbon Ablator
RT	Ray Tracing
RTE	Radiative Transfer Equation
SEM	Scanning Electron Microscope
TC	Thermocouple
TGA	Thermogravimetric Analysis
TPS	Thermal Protection System
XPS	X-ray Photoelectron Spectroscopy





# 1 Introduction

This thesis deals with the study of heat transfer in porous media in practical systems involving extreme environments, defined as high-temperature (i.e. 1500 to 2000 K) and high-flux (i.e. 1 to 10000 kWm<sup>-2</sup>) environments, possibly under non-atmospheric pressures conditions. Conduction, radiation and convection are modes of heat transport in a porous material involving two or more phases. They occur concurrently, influence each other, and are affected by the thermal and morphological properties of the material. Thermochemical processes can take place in such material, additionally affecting the energy balance and temperatures. Modeling heat transfer in this type of medium is challenging as all phenomena must be accounted for simultaneously by solving non-linear coupled sets of equations. This work first focuses on assessing the interaction between conduction and radiation in porous media through experimental and numerical characterizations. It then explores the thermal transport in thermochemically reacting heterogeneous (carbon-phenolic) materials.

As part of the energy transition, harnessing solar energy has become crucial in the challenge of substituting the fossil energy sources by renewable and sustainable energy sources. Amongst these alternative sources are wind, hydroelectric, geothermal, biomass and solar. The solar resource is the one with the biggest potential<sup>(1-3)</sup>. Photovoltaic panels can be used to convert sunlight into electricity<sup>(4)</sup>. The electricity can, for example be used to perform electrolysis for hydrogen production, or can be stored in batteries. Concentrated solar irradiation can be used to drive concentrating photovoltaics<sup>(5-7)</sup>, which however poses the issue of thermal management of these cells<sup>(8)</sup>. Concentrated solar irradiation can also be used to heat up heat transfer fluids that can be used to drive traditional thermodynamic cycles. This approach is also called concentrated solar power (CSP). Furthermore, concentrated radiation can be used to drive thermochemical reactions to produce solar hydrogen or syngas via multi-step water-splitting redox cycles<sup>(1,9-12)</sup>. Solar thermochemical approaches convert solar radiation to chemical energy. The receivers used for solar thermal approaches and the reactors used for solar thermochemical approaches can be based on volumetric devices that use porous structures for enhanced heat and mass transfer<sup>(13-15)</sup>. They change the radiative flux into thermal energy. Solid-gas heterogeneous media are often key components of solar thermal

and thermochemical receiver and reactors. Considering the flux levels, radiative heat transfer plays an important role in conjunction with conduction and/or convection. Modeling coupled heat transfer can help to understand the coupled transport, and improve and optimize the engineering design of such receiver and reactors.

The design of a thermal protection system (TPS) of a space exploration vehicle is another application of thermochemically reacting heterogeneous materials. Recent and several future missions are considering ablative materials instead of reusable TPS. As the economics of a space mission have become very important, reducing the mass of the TPS to increase allocated payload weight is crucial. For this reason, high fidelity modeling of heat and mass transfer through TPS materials is needed. The chemical complexity of pyrolysing ablative materials make the modeling task more difficult, as it involves conduction, convection, chemistry and radiation through a heterogeneous multi-phase material<sup>(16)</sup>.

The characterization of temperature-dependent thermal properties of high-temperature heterogeneous materials, and more specifically of their effective thermal conductivity (ETCs), is essential for the accurate prediction of the heat transfer in these high-temperature environments. The ETC is a conductivity that accounts for contributions of conduction, convection and radiation. The ETC depends on the bulk properties and the morphology of the porous medium<sup>(17–19)</sup>, and also on the (macroscopic, i.e. outer walls of system, as well as microscopic, i.e. between the different phases) boundary conditions. There are various experimental methods to determine ETCs. They can be separated into two categories, namely steady-state and transient techniques. Steady-state methods, like the hot guarded plate method<sup>(20)</sup>, have traditionally been used because of their mathematical simplicity. They are accurate methods but they require well-engineered setups and long test times<sup>(21)</sup>. Transient methods have the advantage of determining directly the thermal diffusivity and they are widely used to measure the effective thermal conductivity of porous ceramics, which are of interest in this work. However, transient are not fully suited to determine ETCs because a relatively small temperature differential is needed, which means that many measurements must be done to determine the ETC for a large temperature range.

The Laser Flash Analysis (LFA) is such a transient method and allows determining the thermal diffusivity, thermal conductivity and heat capacity of a material. A laser pulse on one side of a thin sample heats it up. The analysis of the time-dependent temperature measured on the opposite side of the sample allows for determining the thermal diffusivity of the specimen<sup>(22)</sup>. The half rise time,  $t_{1/2}$  (time taken by the measured temperature to reach half of its maximum value) allows to deduce the thermal diffusivity  $\alpha$ , using Equation (1.1).

$$\alpha = 0.139 \frac{d_{\text{LFA}}}{t_{1/2}} \quad (1.1)$$

where  $d_{\text{LFA}}$  is the sample thickness. The typical measurement uncertainty is expected to be under 3%<sup>(23)</sup>.

The hot wire method, another transient method, is based on Fourier's diffusion law and is also a widely used approach for the measurement of ETCs. A constant current is applied to

---

a heating wire, which heats up the sample. The temperature of the wire is measured and its temperature variation allows to calculate the thermal conductivity of the sample as per Equation (1.2).

$$k_{\text{eff}} = \frac{\dot{Q}}{4\pi} \frac{\ln(t_2) - \ln(t_1)}{T_2 - T_1} \quad (1.2)$$

where  $k_{\text{eff}}$  is the ETC of the sample,  $\dot{Q}$  is the heating power per unit length,  $T_1$  and  $T_2$  the temperatures of the wire measured at times  $t_1$  and  $t_2$  respectively. This method is theoretically only applicable to opaque materials but it has been used by Gross and Tran<sup>(24)</sup> and Coquard et al.<sup>(25)</sup> to determine ETCs of semi-transparent media. They showed that this method remains valid for low absorbing media if the measurement time is long enough (more than 600 seconds).

The transient plane source method, or hot-disk method, uses a double resistive spiral mounted in sandwich between to samples of the material to be characterized<sup>(26–28)</sup>. It is therefore simple and easy to use, especially since no specific sample shape is needed and the size can be quite small (few mm)<sup>(27)</sup>. It has the advantage of determining the thermal diffusivity and conductivity at the same time. The measurement time is relatively short, typically under 600 seconds. Problems with the measurement of thermal conductivity arise if the thermal inertia of the studied material is orders of magnitude lower than that of the probe<sup>(27)</sup>.

As alternatives, or complements, to experimental measurements, numerical methods have been extensively proposed to evaluate ETC of porous metallic and ceramic materials. Numerical investigations of ETCs, neglecting convection and radiation, have been previously reported. Mendes et al. have solved the 3D steady-state heat transfer for pure conduction in open-cell foam-like structures with adiabatic boundary conditions<sup>(17)</sup>, and then proposed a simplified ETC model using only one semi-empirical parameter, which is derived from dimensionless bounds of the thermal conductivity under vacuum conditions. This model has been improved by using two adjustable semi-empirical parameters for the estimation of the ETC based on an additional numerical prediction of the ETC relatively to a reference fluid<sup>(29)</sup>. Coquard et al.<sup>(30)</sup> have evaluated ETCs using a finite volume method to simulate pure conduction heat transfer on the pore-level through idealized cellular structures and through structures obtained by 3D computed tomography (CT). Petrasch et al.<sup>(19)</sup> also utilized 3D CT-scans with a finite volume method and compared the resulting ETC to predictions with semi-empirical ETC models using optimized model parameters. Bracconi et al.<sup>(31)</sup> have studied the influence of geometrical properties on the ETC of open-cell foams, using virtually reconstructed 3D structures. Nevertheless, at high temperatures, ETCs are affected by thermal radiation. To quantify the effect of radiation on the ETC, Mendes et al.<sup>(32)</sup> have used an approach including accurate modeling of the radiation coupled to conduction and calculated ETCs of open-cell ceramic foams<sup>(28,32)</sup>. The prediction of ETCs has been done by simulating the heat transfer through a given sample and using the averaged Fourier's law of conduction. The heat transfer equations have been solved and the divergence of the radiative heat flux as a source term has been included, obtained through the solution of the radiative transfer equation (RTE). Scattering has been considered in the RTE and the extinction coefficient has been calculated using image

processing of the 3D CT-scan images presented by Loretz et al.<sup>(33)</sup>. Some of the predicted ETCs have also been compared to experimental data using the transient plane source technique<sup>(28,34)</sup>, or the panel test technique<sup>(35)</sup>. These comparisons have shown a reasonable agreement, concluding that ETCs of ceramic foams with specific morphology can be quantified and are highly temperature dependent.

Coquard et al.<sup>(18)</sup> have investigated the coupled conduction-radiation heat transfer, by direct simulation of laser flash measurements. The ETC, extinction coefficient, and scattering albedo have been identified as main drivers for the thermal behavior of metallic and ceramic foams. The minimization of the discrepancy between experimental and numerical temperature profiles have allowed for the estimation of the ETC and radiation properties up to 693 K. This technique has also been used to determine thermal conductivities of lightweight alumina and alumino-silicate up to 1400 K<sup>(36)</sup>. The ETC has been shown to be affected by the sintering temperature of the tested samples.

One of the challenges is to overcome the need of doing multiple experiments to determine the ETC for a range of temperatures, like with laser flash analysis. The experimental techniques involve very specific environments like a laser pulse with adiabatic boundary conditions, fixed temperatures. These conditions are not close to conditions for real engineering applications. The use of exact, real or artificial, structures allows to model the heat transfer at the pore-level but it is very costly if the goal is to evaluate the macroscopic thermal behavior of a material.

In the case of semi-transparent heterogeneous material, the use of ETC has its limits, as previously indicated for experimental methods. Conduction and radiation have to be considered separately as they can interfere with each other. Coupling effects in conduction-radiation heat transfer problems have been extensively investigated. The first studies of such problems were done by Viskanta and Grosh<sup>(37)</sup> and Lick<sup>(38)</sup>. Viskanta and Grosh considered a one-dimensional system consisting of two diffuse, nonblack, isothermal, parallel plates separated by an absorbing medium. Those early works were motivated by astrophysics and re-entry heating problems. Several investigations were done for several nongray media such as aerogels<sup>(39)</sup> and combustion gases<sup>(40)</sup>. Tan et al.<sup>(41)</sup> investigated the effect of isotropic scattering for a one-dimensional problem using the control volume method and exact radiation formulation. The radiative heat flux can be evaluated using the  $P_N$  approximation and its variations<sup>(42–47)</sup>, and several other approximate methods such as the two-flux method<sup>(48–54)</sup>, the diffusion method<sup>(55–57)</sup>, the discrete ordinates method<sup>(58–68)</sup>, the exponential kernel approximation<sup>(52,69,70)</sup> or the zonal method<sup>(71)</sup>. With the recent increase of computational power, one method of interest is the Monte-Carlo (MC) method, which was used by Abed and Sacadura<sup>(72)</sup> to calculate the radiative heat flux using the finite-difference approach, and by others<sup>(73,74)</sup>. The Monte-Carlo ray-tracing (RT) method has been used more recently by Petrasch et al.<sup>(75)</sup> and Haussener et al.<sup>(76)</sup> to determine the thermal effective radiative properties based on the exact sample morphologies obtained by computer tomography (CT) measurements. Randrianalisoa and Baillis<sup>(77)</sup> also used the RT method to evaluate effective radiative properties of densely packed spheres in semi-transparent media. Perraudin et al.<sup>(78)</sup> studied coupling effects for radiation-conduction heat transfer in macroporous media using a pore-level MC RT

---

method. They showed that the ETC is affected by the presence of thermal radiation. Upscaling of the radiation-conduction coupling was investigated using the volume averaging method by Leroy and Taine<sup>(79)</sup>. Volume averaging of the RTE only has been investigated by Lipiński et al.<sup>(80)</sup> and Petrasch et al.<sup>(81)</sup>. They compared discrete and continuum scale approaches using the RT technique and showed that the two models were in good agreement within statistical errors. The continuum scale method allowed to reduce the computational by approximately one order of magnitude, which makes it an attractive method to model radiative heat transfer in coupled multi-mode heat transfer problems.

The influence of external irradiation has also been studied. Most works have focused on the effect of pulsed irradiation. Wendlandt<sup>(82)</sup> derived an expression for time-varying spatially uniform pulsed irradiation. Viskanta and Hirleman<sup>(83)</sup> proposed an analytical solution for a one-dimensional semi transparent material irradiated on one side by a collimated beam in the steady-state regime. During laser flash analyses on ceramics, in order to ensure that radiation is absorbed, the sample are coated with a strongly absorbing material (i.e. graphite), or a laser that emits in the strong absorption region of the ceramic must be used (i.e. CO<sub>2</sub> laser with  $\lambda = 10.6\mu\text{m}$ )<sup>(84)</sup>. In the latter case, radiation penetration during a laser-flash analysis must be taken into account. Tan et al.<sup>(85)</sup> investigated the one-dimensional transient and steady-state coupled conduction-radiation heat transfer in a non-gray semi-transparent slab. They evaluated the influence of the slab thickness and its thermal and radiative properties. They showed that the laser flash method may give inaccurate results if the heat transfer model does not take into account conduction-radiation coupling effects. Hahn et al.<sup>(84)</sup> confirmed the relevance of the radiation contribution to heat transfer in a laser flash experiment depends on the sample thickness of the considered material. Liu et al.<sup>(86)</sup> showed that non-Fourier effects can result in significant errors in the thermal diffusivity measurement using the laser flash analysis.

TGA measurements are usually used to determine chemical kinetic properties of carbon-phenolic ablative materials that are generally used as the TPS of space vehicles, as presented by Duffa<sup>(87)</sup> and Natali et al.<sup>(88)</sup>. Differential Scanning calorimetry (DSC) is used to estimate the pyrolysis energy as a function of temperature. The virgin material thermal conductivity and specific heat, can be determined using the laser flash technique<sup>(89)</sup> and DSC respectively, but only for low temperatures. Indeed, as the pyrolysis reactions start at temperatures as low as 200 °C, any test at a higher temperature would involve a partially pyrolyzed state of the material. Therefore, the quantification of partially pyrolyzed or charred state thermal conductivities and specific heat is usually done by adjusting uncertain key material parameters that influence the thermal response of the ablative material to fit experimental data. This was achieved in the late 60's as described by Sykes<sup>(90)</sup> and April et al.<sup>(91)</sup>. More recently, Covington et al.<sup>(92)</sup> fitted numerical predictions to experimental arc-jet data by tuning materials thermal properties. Mars Science Laboratory measurements, detailed by Cheatwood et al.<sup>(93)</sup>, have been widely used in literature and Meurisse and Mansour<sup>(94)</sup> recently used a multi-objective genetic algorithm to estimate key parameters of PICA (Phenolic Impregnated Carbon Ablator) using the Porous material Analysis Toolbox (PATO) to model its thermochemical response.

Effective radiative properties of TPS materials have also been characterized by Banerji et al.<sup>(95)</sup> using the 3D exact morphology obtained by CT.

The characterization of TPS materials relies on their testing and thermochemical response modeling. Gathering experimental data for this type of materials, which has been done in arc-jet testing facilities<sup>(96)</sup>, during actual atmospheric entry<sup>(93)</sup> or in a radiative environment<sup>(97)</sup>, is equally crucial for the validation of these complex models. Many codes involving varying complexity models have been developed to predict the thermochemical behavior of TPS materials. Lachaud et al.<sup>(98)</sup> provided a comprehensive review of the available codes. New multi-dimensional high fidelity programs such as PATO, have been developed to predict accurately the thermal behavior of current and future generation of TPS materials.

### 1.1 Aim

The overall aim of this thesis is to determine the thermal behavior of heterogeneous porous materials in high-flux environments, focusing on conduction and radiation heat transfer modes. The thermal properties of ceramic foams are determined using an innovative engineering approach involving the High-Flux Solar Simulator (HFSS) at EPFL. The limits of applications of an ETC model in the presence of strong irradiation are investigated by separately treating conduction and radiation. Carbon-phenolic materials being generally tested in conventional arc-jet testing facilities, the HFSS is evaluated as an alternative for such space applications materials testing.

### 1.2 Objectives

The aims of this work are achieved by completing the following objectives.

- O.1 Reproducible HFSS testing of different porosities and bulk material ceramic foams models.
- O.2 Development of experimental-numerical approach to retrieve ETC of highly porous ceramic foams from HFSS experiments.
- O.3 Implementation of MC algorithm to compute the divergence of radiative flux throughout a sample, given a temperature field.
- O.4 Development of advanced approach using an algorithm coupling the Porous material Analysis Toolbox based on OpenFOAM (PATO) to the MC solver.
- O.5 Use of coupled conduction-radiation approach to perform sensitivity study to assess the limits of applications of an ETC model or in which conditions it should be replaced by the advanced approach.
- O.6 Comparison of tests in the HFSS to others in an arc-jet facility, and the numerical

rebuilding of both type of tests using PATO, in order to assess the HFSS as an alternative to arc-jet facilities for space-application materials testing.

### 1.3 Scope

In this thesis, the HFSS at EPFL is used as a central tool to develop methods to evaluate material properties of heterogeneous insulators. The HFSS reproduces a solar-like environment that allows testing materials in realistic conditions. Modeling tools are also developed to work closely -and to be validated- with experimental data provided by experiments in this facility. The HFSS capability at producing high magnitude heat flux allows to test space application materials, which makes it a relevant alternative to arc-jet ground testing facilities.

### 1.4 Thesis Outline

In Chapter 2, the HFSS and all experimental tools are described. The HFSS operational procedure and radiative flux measurement technique are introduced. As temperature measurements are crucial for exploiting experiments with numerical models, the assumptions and limitations relative to thermocouple and infrared camera measurements are detailed. The design of an environmental chamber is described. This chamber widens the testing capabilities of the HFSS as it offers the possibility to test materials in a controlled, low-pressure atmosphere. It is particularly interesting for space applications materials, since those encounter low pressures during atmospheric entry. The VKI Plasmatron, which was used to provide experimental data in a convective flux environment, is briefly introduced. Three materials analysis devices are also discussed, namely TGA, scanning electron microscopy (SEM) and X-ray photoelectron spectroscopy (XPS).

Chapter 3 details the numerical models and algorithms. The model implemented in the PATO code is explained. A new boundary condition is developed for the rebuilding of experiments in the HFSS and the Plasmatron. A method to estimate the ETC is proposed. It relies on the minimization of the differences between numerical and experimental temperature profiles. The path-length based MC code solving the RTE is described. The workflow of the PATORAC algorithm, which was developed using PATO and the MC code to perform radiation-conduction coupled simulations, is also explained. Material from this chapter has been accepted for publication in *Ceramics International*.

The results for the ETC estimation using the method introduced in Chapter 3 are presented in Chapter 4. The ETC of five different samples of varying porosity and material are quantified. The influences of the porosity, of the magnitude of the incoming radiative flux, and of a coating layer are evaluated. Material from this chapter has been submitted for publication.

Chapter 5 presents the results of a study involving fully coupled radiation-conduction simulations of a medium composed of two semi-transparent phases, exposed to a HFSS-like radiative flux. The porosity, thermal bulk conductivity, and effective extinction coefficient are varied to

evaluate the range of application of the ETC model. Indeed, the ETC model exhibits limitations when the thermal bulk conductivity and effective extinction coefficient reach values below a given threshold. Material from this chapter has been published in a conference proceeding<sup>(99)</sup> and is in preparation for submission to the *Journal of Quantitative Spectroscopy and Radiative Transfer*.

Chapter 6 deals with the modeling of the thermochemical response of ZURAM, a carbon phenolic material developed by the Deutsche Zentrum für Luft- und Raumfahrt (DLR, Germany). Experimental results and post-test material analyses of samples tested in the VKI Plasmatron are numerically rebuilt using PATO. The ETC model is used, given the material's thermal and effective radiative properties. The thermal properties were measured by the VKI and reported in an ESA project (AblaRadAbla). The effective radiative properties are taken equal to a similar carbon phenolic material studied by Banerji et al.<sup>(95)</sup>. Experiments of ZURAM in the HFSS are also numerically modeled in order to show that the HFSS testing capabilities can be used as an alternative to arc-jet facilities for space applications.



## 2 Experimental tools

This chapter describes the experimental facilities and methods that were used in this thesis. The operation of the High-Flux Solar Simulator (HFSS) at EPFL is detailed, including the equipments that allowed to record crucial experimental temperature data. A convective flux environment, Von Karman Institute's Plasmatron, is briefly introduced. Three material analysis machines, namely, TGA, SEM, and XPS, that permitted material characterization are discussed.

### 2.1 High-Flux Solar Simulator testing

In the context of this thesis, the HFSS is used to test different sample in a concentrated solar-like environment, in order to reproduce conditions of practical systems. As a device capable of delivering high-magnitude heat fluxes, it is also utilized to test ablative TPS materials for space-like environments.

#### 2.1.1 HFSS principle and characteristics

The HFSS at EPFL is a 45 kW<sub>el</sub> multi-source artificial solar flux testing facility. It was designed by Bader et al. <sup>(100,101)</sup>. An identical HFSS was installed at the Australian National University. It can be used for high-temperature, high-flux solar research or material testing and processing.

The HFSS consists of 18 identical modules of 2.5 kW<sub>el</sub> (termed lamps) arranged in two concentric circles, around a virtual sphere of a radius of 1933 mm shown in Figure 2.1. Each module is composed of a short-arc xenon bulb coupled to a truncated ellipsoidal reflector. The ellipsoidal reflector allows to concentrate the radiation emitted by the bulb from the first focal point of the ellipse in the second focal point, which corresponds to the focal plane of the HFSS. Details on the geometry of such a module were presented by Bader et al. <sup>(101)</sup>.

The HFSS was characterised by Leveque et al. <sup>(102)</sup> using a technique that will be described in Section 2.1.2. The facility can deliver a peak heat flux of  $1.0\text{-}1.5 \pm 0.1 \text{ MW m}^{-2}$  per lamp and a maximum of  $21.7 \text{ MW m}^{-2}$  with all 18 lamps in operation at their nominal power. A measured

optical arc-to-target power efficiency of 42 % was measured<sup>(102)</sup>.

In general, having 18 lamps allows to improve the versatility of such a high radiative flux source. It offers the possibility to have a more uniform flux on a wider area than HFSS with fewer lamps, or to get many more peak flux values within a wider range of fluxes. The power delivered to each lamp can be varied by changing the input current for an increased flexibility in flux magnitude. The range of input current is 70-110 A, while the nominal value is 90 A. An input current of 70 A can produce fluctuations in flux values, and values over 90 A can lead to a much faster degradation of the xenon bulbs. Flux magnitudes down to  $10 \text{ kW m}^{-2}$  can be obtained in off-focal planes, showing the lower limit extent of the flexibility offered by the HFSS.

The emission spectrum of xenon lamps at nominal power is very close to the American Society for Testing and Materials Terrestrial Reference Spectra as shown by Bader<sup>(101)</sup>. A change in the power delivered to the lamps would affect the temperature of the xenon plasma created by the short arc. Temperature increases and decreases would shift the emission spectrum towards the lower wavelengths region (higher energy radiation) and towards higher wavelengths (lower energy radiation). In the context of this thesis, when incoming radiation is treated separately (see Chapter 5) the media are considered grey and the spectral dependence does not matter.

### 2.1.2 Flux measurements

The method described by Leveque et al.<sup>(102)</sup> is used in this thesis, and detailed and extended in this section.

The fluxes are measured using a system that couples a water-cooled Lambertian<sup>1</sup> target to a CCD (charged-coupled device) camera. It uses a common approach described by Krueger et al.<sup>(103)</sup> and Sarwar et al.<sup>(104)</sup>. The Lambertian target provided by Haueter Engineering GmbH, is made of a water-cooled aluminium body plasma spray-coated with aluminium oxide. The CCD camera (Basler scA 1400-17 gm, 1.5 MP, resolution 1393 x 1040, 12 bit pixel depth) is equipped with a manual zoom lens (Computar M6Z1212,  $f = 12.5\text{--}75 \text{ mm}$ , Fujinon HE20-1 2 × extender) and a neutral density filter (Midwest ND400, optical density 4). The approach assumes that the camera's response is linear and uniform with respect to the incident radiative flux on the target. The grayscale (GS) maps recorded by the camera are calibrated with a heat flux gauge (Vatell Corporation, TG1000-0, colloidal graphite coated, range  $0\text{--}10 \text{ MW m}^{-2}$ , active area  $1.82 \text{ mm}^2$ , repeatability  $< 3 \%$ ), setting a GS-to-radiative flux factor. There are three other assumptions on which the method is based: *i*) the radiative flux is additive; *ii*) the calibration of the flux gauge is adapted to the spectrum of the light source; *iii*) the radiation spectrum is uniform over the target area. The additive property of the radiative flux is unconditional for the evaluation of fluxes above the range of the heat flux gauge.

---

<sup>1</sup>A Lambertian surface is characterised by a perfectly diffuse reflection, meaning that the apparent brightness of the surface to an observer does not depend on the observer's angle of view.

## 2.1. High-Flux Solar Simulator testing

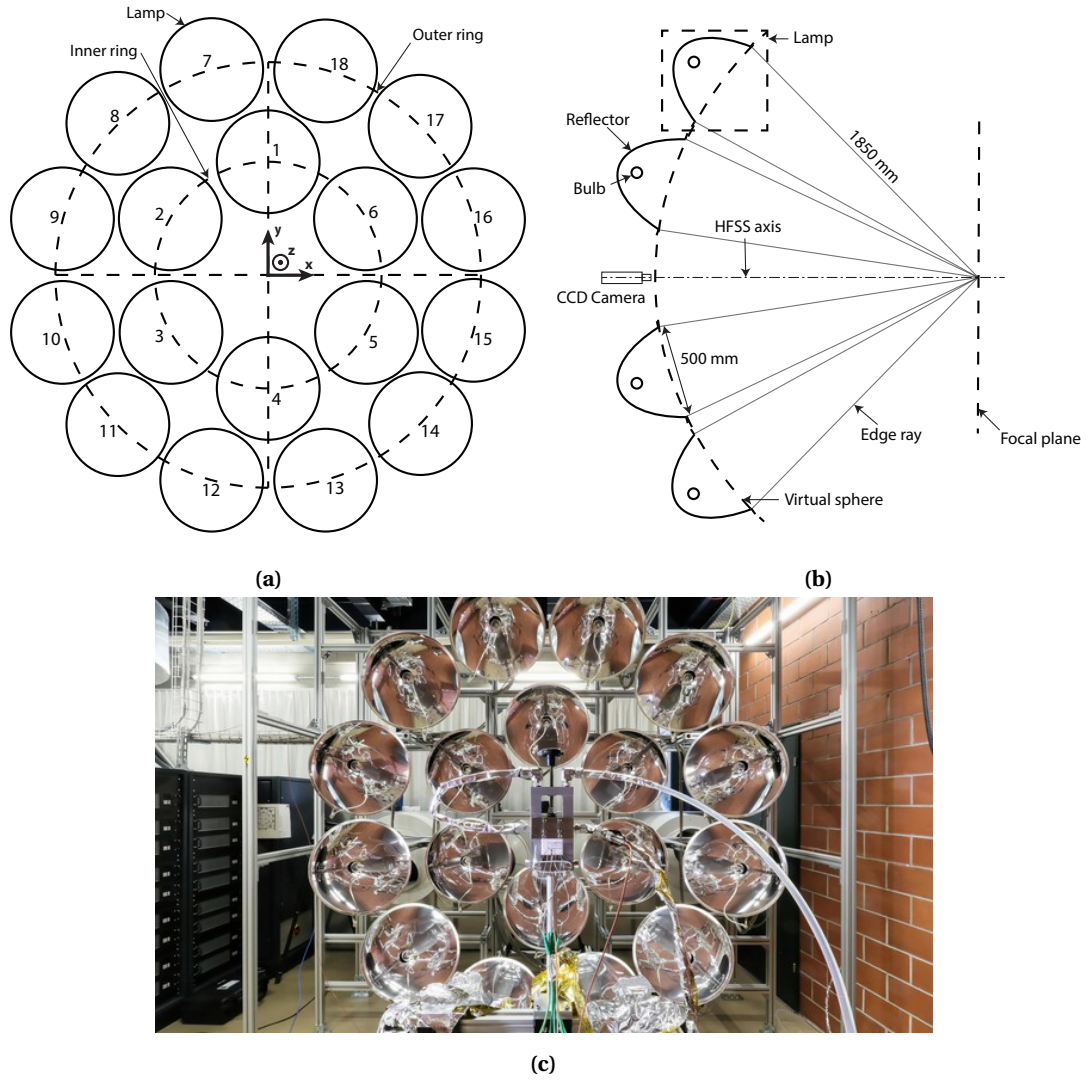


**Figure 2.1** – Schematics of (a) the front view and (b) a cross-section view of the HFSS. (a) shows the numbering of lamps. (b) introduces the dimensions, and the position of the focal plane and the CCD camera (see section 2.1.2), and the two main elements that compose one lamp of this facility. The two schematics were extracted from Leveque et al. <sup>(102)</sup> and modified by the author. (c) shows a photo of the front view with the sample holder without the thermocouple mounting block (see Section 2.1.3), mounted in the focal plane of the HFSS.

### Data acquisition

A Labview interface was developed by Leveque et al. <sup>(102)</sup> to control the CCD camera exposure time, record images and heat flux gauge measurement data. The flux images correspond to an average of 30 images ideally, in order to average out peak flux magnitude fluctuations. They should be recorded when the steady-state regime of the lamps in operation is reached, which occurs between 2 and 5 minutes after the lamp ignition. The CCD camera exposure time is set to avoid over-exposure and hence data loss. The appropriate exposure has to be adapted in function of the peak heat flux. For instance, it needs to be increased when measuring fluxes off-focal plane. The voltage signal recorded using the heat flux gauge is converted to flux

## Chapter 2. Experimental tools

values in  $\text{MW}\cdot\text{m}^{-2}$  by applying the manufacturer's linear calibration curve.

### Flux maps calibration

The calibration of flux maps is done by comparing values measured using the heat flux gauge to GS values recorded by the CCD camera on the Lambertian target. The flux level is recorded by the heat flux gauge at the center of a Lambertian target, which was machined to introduce and support the gauge. The gauge is then replaced by the Lambertian target and GS images are recorded with the same combination of lamps in operation.

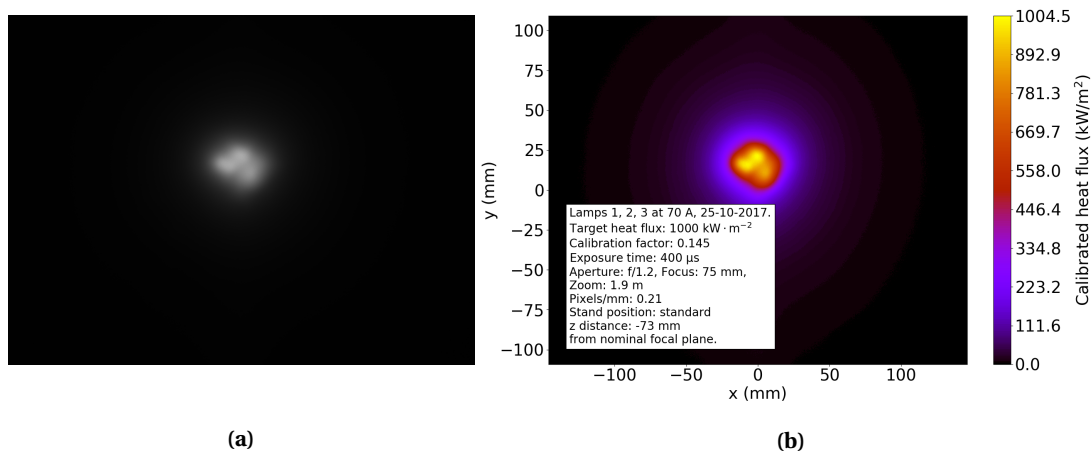


**Figure 2.2** – Example of radiative flux calibration from (a) a GS image to (b) a full radiative heat flux map obtained using lamps 1, 2, and 3 (see Figure 2.1 (a)) operating at 70 A, on the Lambertian target placed 73 mm behind the nominal focal plane. (a) shows a  $1392 \times 1040$  pixel raw GS image. (b) gives details on the size of the calibrated flux area and the GS-to-radiative flux calibration factor. CCD camera parameters described in the next paragraph are also specified.

### CCD camera parameters

Since the CCD camera is located at the center of the HFSS and aligned with its axis, there is no need for digital geometrical corrections of the GS images, as the Lambertian target is oriented orthogonally to the HFSS axis. The zoom, focal length, and aperture of the CCD's manual zoom lens can be adjusted depending on the spatial flux resolution needed, and on the area where the flux has to be determined. A change of aperture is the consequence of a change of the two other parameters. The GS values are also function of the aperture. Therefore, the GS-to-radiative flux factor depends on the configuration of the manual zoom lens installed on the CCD camera. As a consequence, the GS images must be re-calibrated with the flux gauge when a new flux measurement campaign is performed. The spatial resolution in the  $xy$  plane (see Figure 2.1(a)) is also a function of the three CCD camera's parameters and must be re-evaluated too.

### Linear stage

Thanks to an automated linear stage mounted on the experimenting table, the search of focal plane can be done in one HFSS run instead of multiple runs. This feature enhances the flexibility of the HFSS since it has to be turned off to move the target manually for safety reasons. The spatial resolution is below 0.1 mm in the  $z$  axis (see Figure 2.1(a)). The linear stage could also be used for different purposes, like moving a shadowing device in and out of the optical high flux path in the case of thermal fatigue tests, for instance.

### Procedure for repeatability of flux conditions

The reproducibility of specific flux conditions relies on the accurate positioning and alignment of the desired target. The main axis of the experimenting table ( $z$ -axis) is always set parallel to the HFSS axis using a laser tool. This way, a specific position can be first defined by its off-focal ( $x,y$ )-plane distance to focal plane. Then, the distance to one of the wall of the HFSS room and to the ground are enough to define the exact position in the off-focal ( $x,y$ )-plane.

The most consistent way to record an exact position is to evaluate the absolute distance to fixed elements of the test room. The focal plane position, once measured, can be marked on the ground with the help of the laser tool. The linear stage and experimenting table are then used to bring the target to the desired position away from the focal plane. The position in the ( $x,y$ ) off-focal plane can be evaluated by deducing a px/mm factor from raw GS images of the target and images showing the target dimensions. Any pixel can therefore be located using the px/mm factor. The absolute distance to the walls and ground can be deduced from the distance from the target edges to these fixed elements.

### Range of fluxes, identification of combination of lamps for different applications

The flux magnitude can be varied depending on the application. As already specified in Section 2.1.1, the HFSS can deliver a radiative flux as high as  $21.7 \text{ MW m}^{-2}$ . Nevertheless, this flux level is obtained on a very small area (less than 0.5 cm in diameter). Multiple lamps can be used in off-focal planes to generate fluxes from  $100 \text{ kW m}^{-2}$  to several  $\text{MW m}^{-2}$  on much wider areas for highly concentrated solar applications. On the other hand, radiative heat flux levels down to  $5 \text{ kW m}^{-2}$  can be obtained, giving the possibility to perform thermal cycling tests on devices and materials for lower-orbit space applications, for example<sup>(105)</sup>.

The lamp combinations can also be of importance for testing in the HFSS, especially in highly concentrated radiation tests. The irradiation coming from two lamps with a similar angle of incidence (like lamps 5 and 6, see Figure 2.1(a)) can cause important degradation of the tested sample in the direction corresponding to that angle of incidence, whereas the use of diametrically opposed lamps (like lamps 3 and 6) would attenuate the degradation effect for similar flux levels<sup>(106)</sup>. In the case of low flux applications, the use of diametrically opposed lamps is also beneficial in order to obtain an uniform flux distribution, which would occur

between the higher flux regions created by the chosen lamps.

### 2.1.3 Sample holder

Figure 2.3 shows the water-cooled sample holder that was designed for high temperature experiments in the HFSS. It can clamp samples up to 7 cm in height. To guarantee good conduction of the heat coming from the tested sample to the water-cooled volume, aluminium inserts have been added on the clamping edges of the sample holder. A thermocouple mounting block was also designed to fix the position of the tested sample in the  $(xy)$  plane once the position of the sample holder was set. It ensures the reproducibility of the position for experiments with different samples. Indeed, preliminary experiments showed that inaccurate positioning of the sample by 1 mm only could already induce differences in the measured temperatures of up to 100 K between two successive tests with identical conditions. At least one thermocouple has to be used to take advantage of the mounting block. A hole should be machined in the tested sample for each thermocouple (see Section 2.1.4).

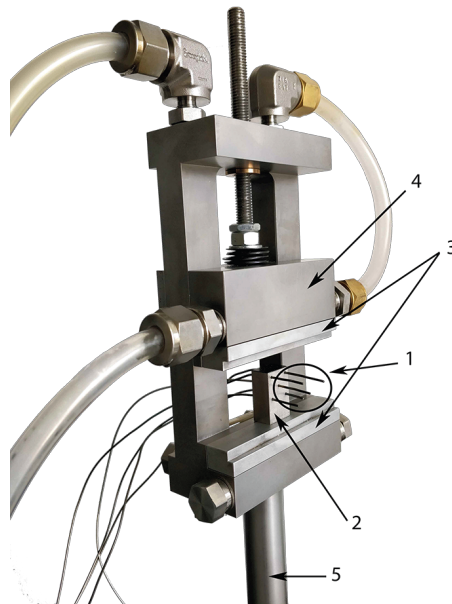


**Figure 2.3** – Photo of the water-cooled sample holder. The holders clamps are 7 cm. The holder includes a thermocouple mounting block, guaranteeing an accurate positioning of the thermocouples relatively to the heat flux distribution (1: Thermocouples, 2: Thermocouple mounting block, 3: Aluminum clamps, 4: Water-cooled body, 5: Holding rod). The picture is extracted from a submitted article by the author (Mora-Monteros et al.)<sup>(107)</sup>

### 2.1.4 Thermocouples measurements

Thermocouples (TC) were used for the measurement of temperature within the sample. Figure 2.3 shows the arrangement of the five 1mm-diameter inconel-steel shielded probes

containing K-type thermocouples (RS-components, standard tolerance TC type K class 1) that were used to record temperatures of the bulk material at several positions inside the sample. The technical drawing of the holes to be machined in the tested samples according to this thermocouple arrangement is shown in Appendix A. The thermocouples are inserted in the sample such that they appear at 3, 4, 5, 8, and 15 mm from the surface. The thermocouple at 4 mm is centered, while the other four are arranged as a 1 cm<sup>2</sup> square centered on the sample.

In principle, the best approach should be positioning the TCs perpendicular to the main temperature gradient. However, in this particular case the TCs would have been directly irradiated if they were inserted from the side of the sample, which corresponds to a worse situation.

### Assumptions and limitations

As this work deals with highly porous materials placed in a high radiative flux environment, the use of in-depth K-type thermocouples poses two problems.

First, it is necessary to evaluate whether the inconel-steel probes are directly irradiated by radiation coming from the HFSS. Direct irradiation is problematic because the temperature measured by the TCs would not correspond to the material temperature. The materials tested are assumed to be semi-transparent, gray and diffuse participating media. As discussed in Chapters 4 and 6, they also present extinction coefficients with lowest values of around 2500 m<sup>-1</sup>. The shallowest TC is placed at 3 mm from the surface. Considering the lower value of extinction coefficient, the typical penetration length is 400 μm. This indicates that the thermocouples are not directly irradiated.

The second problem is to assess which temperature is actually measured by an inconel-steel shielded TC inserted in such a highly porous, thermally insulating material. It is assumed that the solid and gas phases are in local thermal equilibrium. This is verified in the studied materials and it will be discussed in Section 3.1. Moreover, the potential heat sink effect created by the relatively highly conducting TC is not important enough to significantly affect the TC measurements. Indeed, given the thermal conductivity of inconel (about 15 W m<sup>-1</sup> K<sup>-1</sup>), the diameter of the TCs (1 mm), and the difference in sample and TCs cross-sections, a simple application of Fourier's law of conduction shows that the heat flux transported through one thermocouple is about 2 orders of magnitude smaller than the heat flux through the ceramic foam sample.

The thermocouple mounting block was used to prevent discrepancies in the position of the TCs in the (*x,y*) plane. However, another source of error corresponds to the uncertainty of the TC in the axial (*z*-axis, HFSS axis) direction. To limit this uncertainty, a good contact of the TCs at the bottom of the holes that were drilled in the samples was ensured. The thermocouple mounting block was also used to prevent any movement of the thermocouples out of their longitudinal position.

### 2.1.5 Surface temperature measurements: IR Camera

An Infrared (IR) camera (FLIRA655sc) was used to measure the surface temperature of the samples during tests. It was installed in the place of the CCD camera, to also avoid the need for any geometrical corrections. The IR camera's detector is an uncooled microbolometer and operates in the longwave infrared (LWIR) range (8-14  $\mu\text{m}$ ). The resolution was 640x480 with 17  $\mu\text{m}$  pixels, the frame rate was up to 50Hz for a full window, and the temperature measurement accuracy was  $\pm 2\%$  by the camera's specifications.

### Emissivity and reflected temperature

The temperature measurement by the IR camera required the knowledge of the apparent emissivity ( $\epsilon=0.95$ ) of the material and the reflected temperature ( $T_{\text{refl}}=293\text{ K}$ ). The calibration was done with the alumina and alumino-silicate (AS) samples with a known maximum operation temperature, i.e. the temperature before sintering starts. Several peak radiative fluxes (ranging between  $800\text{ kW m}^{-2}$  and  $1600\text{ kW m}^{-2}$ ) were used in order to quantify the emissivity and source reflected temperature. Once a limit was found, the settings were adjusted accordingly, for the maximum temperature to correspond to the maximum operation temperature of the samples. The emissivity found with this approach is consistent with the values found in Touloukian<sup>(108)</sup> for alumina in the IR wavelength range.

The reflected temperature corresponds to ambient radiation in the IR wavelength range that is reflected onto the sample. The experimental room is at a temperature around 293 K. The emission of the xenon bulbs in the IR camera wavelength range due to xenon radiation is negligible since the cut-off wavelength of quartz, of which the bulbs are made, is at around 4  $\mu\text{m}$ . Given the emissivity of the samples in the IR range, the reflectivity is very small and the influence of the IR radiation at relatively low temperatures by the hot quartz was negligible.

### Measurement errors

The IR camera was a source of errors because of the uncertainties on the emissivity of the sample and the reflected temperature. Changing the emissivity between 0.9 and 0.95 yielded errors in the temperatures up to  $\pm 5\%$ . Another source of error originated from the spatial resolution of the measured surface temperature. Due to the position of the IR camera (same as CCD camera, see Figure 2.1(a)) and its fixed field of view (fixed focal length), the size of the region of interest (sample of size of  $40\times 40\text{ mm}^2$ , see Chapter 4) corresponded to  $41\times 41$  pixels, yielding a resolution of 0.975 mm for the surface temperature measurements. The consequence of this relatively coarse resolution is that the measured temperature position can be shifted by an absolute distance of up to 0.5 mm (half a pixel). The effect of such a shift can induce temperature differences up to 3 % at steady-state.



### 2.1.6 Environmental chamber

An environmental chamber was designed in collaboration with a colleague at the Laboratory of Renewable Energies and Science Engineering (LRESE) to enable HFSS tests in a controlled (non-air and/or low pressure) atmosphere. The goal is to have the possibility to reproduce conditions from different testing facilities or applications, like atmospheric entry where the pressure at the surface of the heat shield is lower than atmospheric lab pressure or where the composition of the atmosphere is dominated by other gases (for example, the Venus or Mars atmospheres are dominated by CO<sub>2</sub>). The objectives to be met by the environmental chamber were:

- Enable the incoming irradiation from inner and outer ring lamps to reach a test specimen, without undesirable attenuation of the lamp wavelengths or concentration of the radiation (as the convex surface can act as a focusing device).
- Ensure that materials would not heat up beyond a safe limit.
- Ensure an optimised size, including sufficient distance between test specimen and walls to limit deposition of ejected hot particles on chamber surface, and easy accessibility, balanced with a small volume to bring to lower pressures, and low weight to be easily moveable and compatible with mounting system in the laboratory.
- Ensure that ports for water cooling, thermocouples, gas flow-through, and a window suitable for use with the IR camera can be introduced.
- Aim at a low-cost, compatible with an existing base and water-cooled model mount, and standard flanges design.

The major advantage of a chamber made of pyrex (made of borosilicate) for experiments in the HFSS is that the light from the radiation modules can pass through all sides of the chamber and excess light can be transmitted out, while the borosilicate absorbs very little. Therefore, at high incoming fluxes, the chamber walls remain adequately cool without the need for insulation. Outside of the focal plane but still with high incoming fluxes, this reduces the issue of absorbing radiation in parts not designed for that purpose. Without the need to consider insulation, the sizing of the spherical chamber would be more straightforward, with only the sample holder to consider. The CCD camera can image through the borosilicate walls and only one port is required for imaging with the IR camera (wavelengths 7 to 14  $\mu\text{m}$ ). The main danger is damage to the borosilicate from heated particulate matter that is ejected from samples inside the chamber. However this can be mitigated by gas flow through the entire chamber. The spherical chamber was the more cost-effective option. The manufacturers rate their components for high vacuum applications<sup>(109)</sup>. Standard flanges can be fitted for connecting to other standard components and a pressure down to 1 mbar could be maintained with the setup shown in Figure 2.4. Two of the most expensive components of the system are the IR transmitting window and the vacuum pump.

As the borosilicate does not transmit in the necessary wavelengths for the IR camera, a window port was necessary. The selected window is made from zinc selenide (ZnSe), which transmits in the IR camera-compatible range of 600 to 16000 nm. The maximum available diameter for such a window was 20 mm, corresponding to a KF40 flange. Although significantly reducing the imaging area, it is still extremely beneficial to be able to monitor the surface temperature at the centre of the front face of the sample.

The design iterations progressed from initial designs with arbitrarily sized inlet, outlet and window ports and sphere dimensions to a fully dimensioned, refined concept. The detailed design was completed by investigating standard sizing of vacuum components available from VACOM and possible flange sizes, wall thickness and diameters with the manufacturer Verre & Quartz Technologies SA. The spherical chamber was adapted to an existing small cylindrical aluminium chamber, which set the inlet and outlet flange dimensions and enabled the use of existing o-ring assemblies and ports for thermocouples, and water and gas flow. This also allowed for the use of an existing water cooled sample holder, with only slight changes to the post height and the orientation of tube connectors. The detailed drawing is provided in Appendix A. An assembly view of the new borosilicate spherical section, the existing aluminium section and the existing water-cooled sample holder is shown in Figure 2.4(a). Figure 2.4(b) shows a picture of the final setup in the HFSS room.

The characteristic dimensions of the chamber are listed in Table 2.1.

**Table 2.1** – Environmental chamber characteristic dimensions.

Sphere outside diameter	260 mm
Wall thickness	5 mm
Inlet/outlet flange	ISO160
Window port flange	KF40

## 2.2 Convection flux testing

Experimental results in a convection flux environment presented in Chapter 6 were obtained in the Plasmatron facility at VKI, Belgium. The Plasmatron is a high enthalpy wind tunnel. The plasma is generated by electromagnetic induction and blown as a jet inside a test chamber at sub-atmospheric pressure<sup>(110)</sup>.

The facility uses a high frequency, high power, high voltage (400 Hz, 1.2 MW, 2 kV) solid state generator. The torch is mounted on a water-cooled test chamber, which is 1.4 m in diameter and 2.5 m long. The chamber is equipped with view ports that allow unrestricted optical access to the test section. The vacuum pumping system is capable of extracting  $3900 \text{ m}^3 \text{ h}^{-1}$ , to reach an ultimate pressure of 0.04 mbar. The facility is computer controlled and can deliver heat fluxes between  $0.3$  and  $4.6 \text{ MW m}^{-2}$ .

The testing conditions specific to the studied samples are described in Chapter 6.

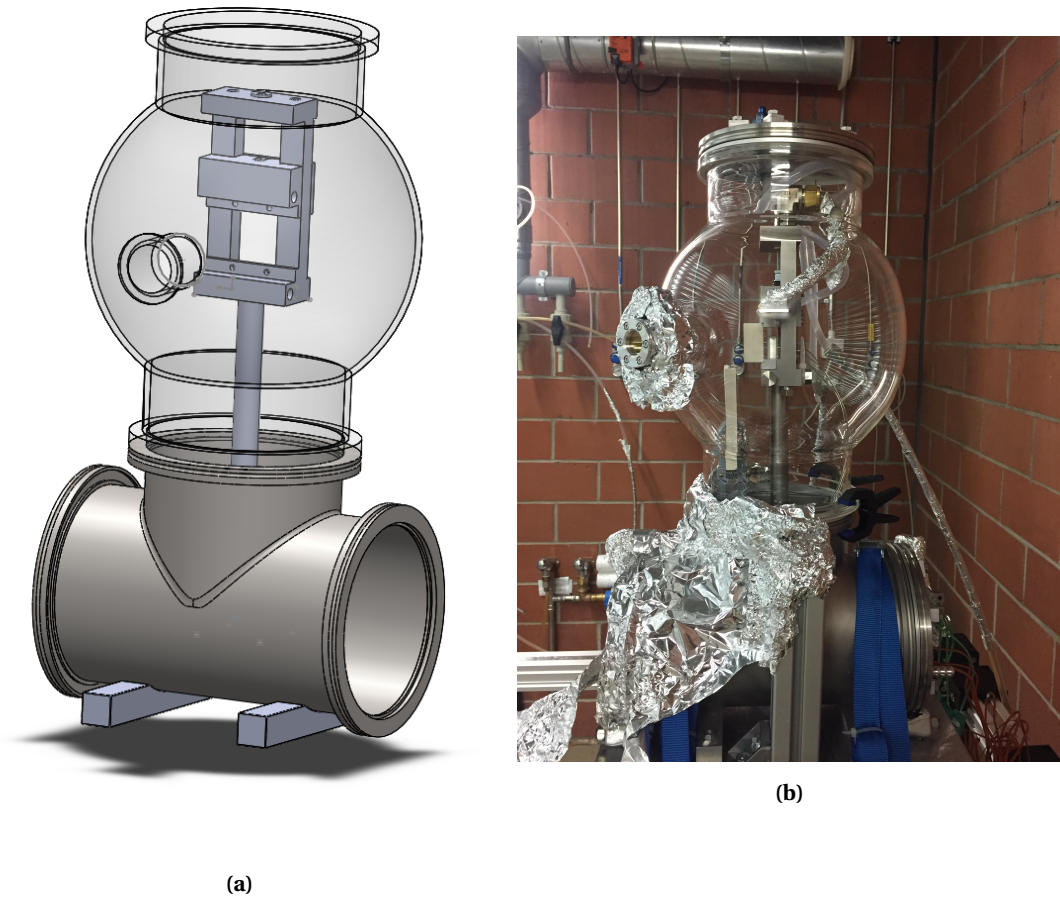


**Figure 2.4** – Borosilicate and aluminium chamber sections. (a) Final design. (b) Picture of the final setup before test.

## 2.3 Material Analyses

### 2.3.1 Thermogravimetric analysis

The Thermogravimetric Analysis (TGA) is a technique which gives the evolution of the weight of a sample with the temperature in the controlled atmosphere. This machine contains a sample pan which is supported by a balance and the pan is placed in a furnace during the experiment. The weight of the sample and the temperature are monitored and then plotted. The sample environment is controlled by a sample purge gas which can be either inert or reactive. This gas flows over the sample and exits through an exhaust.

TGA analyses the presence of chemical or physical reactions by measuring the evolution of mass loss with increasing temperature in controlled atmosphere. TGA can provide information about chemical and physical properties such as vaporisation, absorption, sublimation, decomposition or also solid-gas interaction. Two gas atmospheres are available with this device: nitrogen or air. Analyses were done with TGA 4000 from Perkin Elmer located at EPFL

(Figure 2.5) equipped with an autosampler, which capacity is 45 samples. The temperature range is from 15 to 1000 °C. As there is a hole in the lid of the machine, the measurements are done at atmospheric pressure. The heating rate could go up to 40°C/min. In this specific case, TGA was used to quantify the amount of resin left in the tested samples. Therefore, the heating rate did not affect the results.

The protocol to quantify the charring degree of VKI tested sample with the TGA and corresponding results are described in Chapter 6.

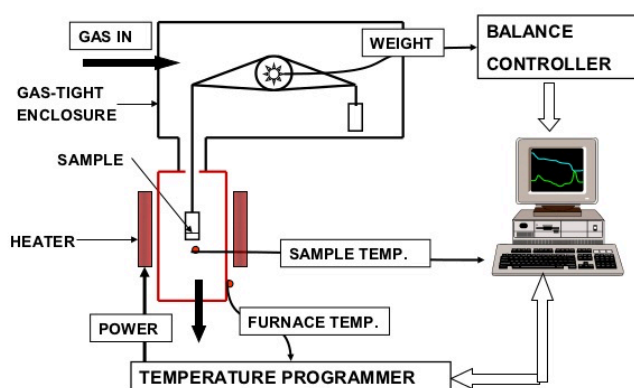


**Figure 2.5** – TGA set-up consisting of a furnace, a balance and a gas system which are computer controlled.

### 2.3.2 Scanning electron microscope

The SEM (Scanning Electron Microscope) produces images of the sample's structure by projection of a focused beam of high-energy electrons on the sample which generates a variety of signals. A 2-dimensional image is then acquired.

The principle behind the SEM is as follows: Electrons are accelerated and focused on the sample with a certain kinetic energy. The electrons are then decelerated when hitting the sample surface. This will produce a signal including secondary and backscattered electrons that are used to display the SEM images.

The most common SEM mode is detection of secondary electrons emitted by atoms excited by the electron beam. The number of secondary electrons that can be detected depends, among other things, on specimen topography. By scanning the sample and collecting the secondary electrons that are emitted using a special detector, an image displaying the topography of the surface is created.

Depending to the application, the SEM may require minimal sample preparation consisting of cutting the sample fixing it on the sample holder. The samples must not outgas during manipulation as they will be in a vacuum chamber (around  $10^{-5}/10^{-6}$  torr) during operation. For electrically insulating samples, an electrically conductive coating has to be applied.

SEM was used to evaluate the ceramic foam sample pore sizes in Chapter 4 and to measure the char thickness of VKI tested samples, which methodology is presented in more details in Chapter 6.

### 2.3.3 X-ray Photoelectron Spectroscopy

To identify which compounds are still present in the samples after plasma exposition, the X-ray photoelectron spectroscopy (XPS) characterisation of each plasmatron exposed sample is made. XPS also known as electron spectroscopy for chemical analysis (ESCA), is a technique for analysing the surface chemistry of a material. XPS can measure the elemental composition, chemical state and electronic state of the elements within a material. XPS spectra are obtained by irradiating a solid surface with a beam of X-rays while simultaneously measuring the kinetic energy of electrons that are emitted from the top 1-10 nm of the material being analysed. A photoelectron spectrum is recorded by counting ejected electrons over a range of electron kinetic energies. Peaks appear in the spectrum from atoms emitting electrons of a particular characteristic energy. The energies and intensities of the photoelectron peaks enable identification and quantification of all surface elements (except hydrogen).

Preliminary analysis was performed using monochromatic Al K $\alpha$  X-ray source with a beam size of 100  $\mu\text{m}$ . The analyser is set at 45° angle from the sample surface. The XPS system PHI Versa at EPFL was used to quantify the char thickness and charring degree profile of VKI tested samples. The methodology and results are presented in Chapter 6.

## 2.4 Materials

In this thesis, two types of materials are considered. Ceramic foams, made of pure alumina and of alumino-silicate, are tested in the HFSS. Their characteristics are detailed in Chapter 4. The other material is a carbon-phenolic composite called ZURAM, which is described in Chapter 6.



## 3 Numerical methods and models

This chapter presents the numerical methods and models developed in this work. A model including the conservation of energy, mass and momentum in a material in which thermochemical processes occur is described. Some simplifications can be made when materials without chemical process are investigated. Radiative heat transfer through porous materials is modeled using a Monte-Carlo ray-tracing method, which is discussed. These two models can be linked to form one single algorithm to study the coupled radiation-conduction heat transfer.

### 3.1 Energy conservation equation: Porous material Analysis Toolbox (PATO)

The Porous material Analysis Toolbox (PATO) is used to resolve the transient thermal response of materials studied in this work<sup>(111)</sup>. PATO is a state of the art code that is usually used for the simulation of materials' thermochemical response in space applications. It is based on the volume-averaged mathematical theory and it solves the mass, momentum and energy equations inside the material. These equations, derived and detailed by Lachaud et al.<sup>(16)</sup>, are briefly explained here.

#### 3.1.1 Conservation of mass

The equation for the conservation of the mass of gas inside the material reads:

$$\partial_t (f_{v,g} \rho_g) + \nabla \cdot (f_{v,g} \rho_g \mathbf{v}_g) = \Pi \quad (3.1)$$

where  $f_{v,g}$  is the gas volume fraction,  $\rho_g$  is the gas density, and  $\mathbf{v}_g$  is the vector accounting for gas velocity inside the material.  $\Pi$  is a production term (in  $\text{kg m}^{-3} \text{s}^{-1}$ ) corresponding to pyrolysis gas production, which is generally obtained by fitting one or several Arrhenius laws to thermogravimetry analyses<sup>(16)</sup>.

### 3.1.2 Conservation of momentum

Under the hypothesis of a continuum regime through the porous material, the equation of conservation of momentum is reduced to Darcy's law<sup>(16)</sup>.

$$\mathbf{v}_g = -\frac{1}{f_{v,g}\mu} \underline{\underline{\mathbf{K}}} \cdot \nabla p \quad (3.2)$$

where,  $\mathbf{v}_g$  is the gas velocity inside the material,  $\underline{\underline{\mathbf{K}}}$  is the permeability tensor,  $\mu$  the dynamic viscosity and  $p$  the pressure. Darcy's law is only valid for low velocities (Reynolds numbers below 5, based on pore diameter). For larger Reynolds numbers, Forcheimer extension needs to be used.

### 3.1.3 Conservation of energy

Puiroux et al.<sup>(112)</sup> have shown that solid and gas phases are in thermal equilibrium as long as the Péclet number (diffusion of heat within the pores) is small. The small pore size (100  $\mu\text{m}$ ) and the slow pyrolysis gas flow in carbon/phenolic ablators space materials ensures that this condition is met<sup>(16)</sup>. For ceramic foams, the maximum pore size of the ceramic foams considered is 400  $\mu\text{m}$ . As there is no gas production inside the sample, the assumption of no gas flow can be made. The negligible local flow velocity guarantees a small Péclet number and the assumption of thermal equilibrium within the pore is sound.

Under the assumption of local thermal equilibrium, the equation for the conservation of energy is of the form:

$$\partial_t(\rho_p e_p) + \nabla \cdot (f_{v,g} \rho_g h_g \mathbf{v}_g) + \nabla \cdot \sum_{k=1}^{N_g} (\mathcal{Q}_k) = \nabla \cdot (\mathbf{k}_{\text{eff}} \cdot \nabla T) + \mu f_{v,g}^2 (\underline{\underline{\mathbf{K}}}^{-1} \cdot \mathbf{v}_g) \cdot \mathbf{v}_g \quad (3.3)$$

The first term on the left hand side (LHS) describes the total stored energy of the porous material (subscript p,  $\rho$  is the density,  $e$  is the specific energy), which is defined as the sum of the specific energy of its phases (solid and gas). Convective heat transfer inside the material is defined by the second term on the LHS, with  $h_g$  being the absolute enthalpy of the gas phase. The convection velocity of the gas phase is the solution of Equation (3.2). The last term on the LHS accounts for diffusive heat transfer, where  $N_g$  is the number of gaseous species,  $\mathcal{Q}_k$  is the effective diffusive heat flux. The first term on the right hand side (RHS) defines conduction heat transfer, which is the main mode of heat transfer. The effective thermal conductivity (ETC) tensor,  $\mathbf{k}_{\text{eff}}$ , accounts for conduction through the solid and gas phases of the material and radiative heat transfer. The second term on the RHS corresponds to the energy dissipated by viscous effects in the Darcian regime<sup>(113)</sup>. This term is small enough to be neglected<sup>(16)</sup>.



## 3.2. Pseudo-inverse methodology for determining effective thermal conductivity (ETC)

### 3.1.4 Simplifications for modeling ceramic foams thermal response

In the case of the thermal response modeling of ceramic foams, Equation (3.3) can be simplified. The gas flow through the sample can be assumed negligible, as there is no gas production and the studied materials are partially closed-cell structures. The diffusion heat flux is also negligible compared to conduction flux. As a results, Equation (3.3), becomes:

$$\partial_t(\rho e) = \nabla \cdot (\mathbf{k}_{\text{eff}} \cdot \nabla T) \quad (3.4)$$

where  $\mathbf{k}_{\text{eff}}$  is assumed isotropic and accounts for radiative heat transfer coupled with conduction. The subscript p has been dropped for simplicity.

### 3.1.5 Spatially resolved time dependent boundary condition

In order to apply time dependent, spatially resolved boundary conditions (BC), a new library called `timeVaryingMappedTemperatureRadiationConvection`<sup>1</sup> was implemented in PATO. The library supports Dirichlet (temperature) or Neumann (flux) BCs. The input is a set of points coordinates with their corresponding temperature/flux values. If the set of points does not correspond to mesh points, values are automatically interpolated on the mesh points.

This library was used for the rebuilding of tests in the HFSS (Chapter 4) and VKI's Plasmatron (Chapter 6), where IR camera's temperature data were used as Dirichlet BCs. It was also utilized in Chapter 5 where the BCs corresponded to flux maps measured in the HFSS.

## 3.2 Pseudo-inverse methodology for determining effective thermal conductivity (ETC)

A combined experimental-numerical approach was used to iteratively solve the governing equations assuming a given temperature-dependent ETC (accounting for conduction and radiation in the porous structure). The computational temperature results were compared to the experimental data, and then the ETC was updated (Figure 3.1). The iterative process assumed an isotropic and temperature-dependent ETC. The temperature-dependent ETC measured by laser-flash analysis was used as the starting ETC. The goodness of fit of the computed temperature to the experimental measurement was evaluated using the  $R^2$  value for each thermocouple position defined as:

$$R^2 = 1 - \frac{\sum_{t_j} (T_i(t_j) - T_{i,\text{exp}}(t_j))^2}{\sum_{t_j} (T_i(t_j) - \bar{T}_{i,\text{exp}})^2} \quad (3.5)$$

---

<sup>1</sup>This library applies to cases where the BCs do not show any symmetry pattern. For cases with strong symmetry patterns, like an axisymmetrical flux on a hemispherical surface, existing tools in PATO shall be preferred.

### Chapter 3. Numerical methods and models

---

The ETC was obtained by the iterative coupled experimental-numerical scheme (Figure 3.1), which is explained in details in Algorithm 1.

---

**Algorithm 1:** Algorithm for iterative process to determine temperature-dependent ETC

---

Initialize  $\mathbf{k}_{\text{eff}}$ ;

Initialize endTime: set according to the observed heating rate. The bigger the heating rate, the smaller the initial end time, so that a small range of temperature (up to 100 K) was covered, a range where the ETC could be assumed to vary linearly;

1 Compute temperature solution  $T_{x_i}(t)$  for all  $x_i$  (TC positions);

Compare  $T_{x_i}(t)$  with  $T_{x_i,\text{exp}}(t)$  at the five discrete locations,  $x_i$ ;

Quantify the difference by  $R^2$ ;

**if**  $R_{x_i}^2 < R_{\text{lim}}^2$  **then** // is  $R^2$  smaller than the tolerance fixed for this value?

    Increase endTime;

**if**  $\text{endTime} \leq \text{maxTime}$  **then**

        | exit: end of process

**else**

        | cycle (go back to line 1);

**end**

**else**

**if**  $t < t_{\text{steady-state}}$  **then** // is this transient regime?

**if**  $|\frac{\partial T_{x_i}}{\partial t} - \frac{\partial T_{x_i,\text{exp}}}{\partial t}| < \varepsilon_{\text{slope}}$  **then** // does the temperature change rate present a good match with the experimental value ?

            The temperature difference is acceptable. In general, having a good match for the temperature change rate at each iteration guarantees that a temperature difference outside the fixed tolerance is acceptable;

**else**

            Adjust  $\mathbf{k}_{\text{eff}}$  manually to take advantage of the transient behavior ( $t < t_{\text{steady-state}}$ ) of the measured temperature and guarantee that all information is used. In general, a maximum of five iterations is enough to match the experimental slopes for all thermocouple positions;

**end**

        Increase endTime gradually. The increments for the end time increase as the temperature change rate decreases when reaching the steady-state regime;  
        cycle (go back to line 1);

**else**

        When the ETC is evaluated for the complete range of temperatures (room temperature to maximum surface temperature,  $t < t_{\text{steady-state}}$ ) the end time is set to the maximum time of experiment. If the  $R^2$  value is higher than its limit, refinements of the ETC were performed and they consisted in adjusting of the high temperature conductivities by  $\pm 5\%$ . A maximum of five iterations was usually enough to reach the final conductivity profile;

**end**

**end**

---

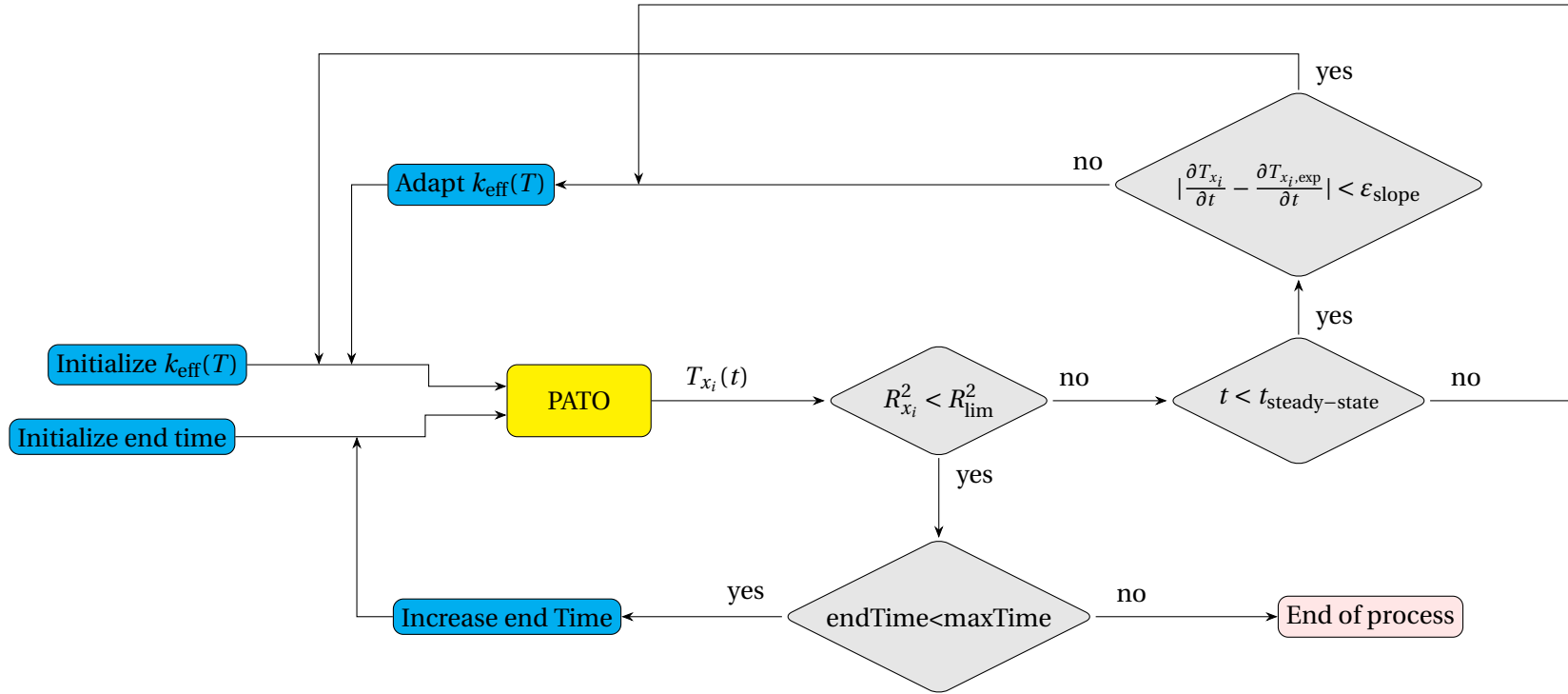


**Figure 3.1** – Iterative process flow chart utilizing experiments and computational model to determine the temperature-dependent ETC.

### 3.3 Radiative heat transfer: Monte-Carlo radiation code

This work considers quasi-steady radiative heat transfer in a medium composed of two semi-transparent phases. For ceramic foams, the two phases are the solid ceramic porous structure and the air filling the pores. The method described in this section is also capable of solving radiative transfer in a medium which phases compositions change, in the case of carbon-phenolic materials. The phase compositions then depend on the extent of decomposition of the resin<sup>(95)</sup>.

The approach is subject to the following assumptions: (i) the media considered are grey and diffuse; (ii) the two phases are considered homogeneous and isotropic; (iii) the media is considered at local thermodynamic equilibrium and at rest compared to the speed of light; and (iv) characteristic lengths of each component are greater than the wavelength of interest such that geometrical optics are valid.

The radiative transfer equation (RTE) describes broadly the conservation of intensity. The averaged intensity conservation for a multi-phase media composed of two semi-transparent phases reads<sup>(81)</sup>:

$$\begin{aligned} \hat{\mathbf{s}} \cdot \nabla I_i(\mathbf{r}, \hat{\mathbf{s}}) = & -\beta_i I_i(\mathbf{r}, \hat{\mathbf{s}}) + \kappa_i n_i^2 I_{b,i}(\mathbf{r}) + \frac{\sigma_{s,ii}}{4\pi} \int_{\Omega_i=0}^{4\pi} I_i(\mathbf{r}, \hat{\mathbf{s}}_i) \Phi_{ii}(\hat{\mathbf{s}}_i, \hat{\mathbf{s}}) d\Omega_i \\ & + \frac{\sigma_{s,ji}}{4\pi} \int_{\Omega_i=0}^{4\pi} I_j(\mathbf{r}, \hat{\mathbf{s}}_i) \Phi_{ji}(\hat{\mathbf{s}}_i, \hat{\mathbf{s}}) d\Omega_i, \quad i, j = 1, 2; i \neq j \end{aligned} \quad (3.6)$$

where  $\hat{\mathbf{s}}$  is a unit directional vector,  $I_i$  is the local volume averaged radiative intensity,  $I_{b,i}$  the volume averaged blackbody radiative intensity in vacuum,  $\kappa_i$ ,  $\sigma_{s,ij}$  and  $\beta_i$  the effective absorption, scattering and extinction coefficients respectively.  $\Phi_{ji}$  is the scattering phase function.  $n_i$  is the refractive index, which correspond to the real part of the complex index of refraction  $m$  defined as:

$$m = n - ik \quad (3.7)$$

where  $k$  is the imaginary part of the complex index of refraction, that is linked to the absorption coefficient in Equation (3.8).

$$\kappa = \frac{4\pi k}{\lambda} \quad (3.8)$$

where  $\lambda$  corresponds to the wavelength of interest considered in the simulation.  $\lambda$  was taken equal to 1  $\mu\text{m}$ , value taken between the visible and infrared wavelength ranges, as incoming radiation in HFSS is in the visible range, and the internal thermal radiation is in the infrared. Moreover, the studied samples were considered as grey media and  $\lambda$  only slightly affected the value of  $\kappa$  (see Equation (3.8)).

The effective radiative properties are given in Equations (3.9) to (3.13). They are a combination

of bulk and morphology dependent properties. The expression for  $\beta_i$  is valid for a medium consisting of two semi-transparent phases.

$$\sigma_{s,ii} = \sigma_{s,\text{refl},i} + \sigma_{s,d,i} \quad (3.9)$$

$$\sigma_{s,ij} = \sigma_{s,\text{refr},i} \quad (3.10)$$

$$\Phi_{ii} = \sigma_{s,ii}^{-1} (\Phi_{\text{refl},i} \sigma_{s,\text{refl},i} + \Phi_{d,i} \sigma_{s,d,i}) \quad (3.11)$$

$$\Phi_{ij} = \sigma_{s,ij}^{-1} \Phi_{\text{refr},i} \sigma_{s,\text{refr},i} \quad (3.12)$$

$$\beta_i = \kappa_i + \sigma_{s,ii} + \sigma_{s,ij} \quad (3.13)$$

The morphology dependent effective properties,  $\sigma_{s,\text{refl},i}$  and  $\sigma_{s,\text{refr},i}$ , can be determined for the two-phase medium by performing 3D direct pore-level simulations on the exact 3D structure obtained by computed tomography (CT) <sup>(75,76,114)</sup>.

The integration of the radiative intensity allows to express the radiative heat flux,  $\mathbf{q}_r$ , as <sup>(115)</sup>:

$$\mathbf{q}_r = \int_{4\pi} I(\hat{\mathbf{s}}) \hat{\mathbf{s}} d\Omega \quad (3.14)$$

Equation (3.6) can be considered as an intensity balance and can therefore be integrated into Equation (3.15) in order to get a volume balance, omitting the position vector notation for brevity.

$$\begin{aligned} \int_{4\pi} \hat{\mathbf{s}} \cdot \nabla I_i d\Omega = & - \int_{4\pi} \beta_i I_i(\hat{\mathbf{s}}) d\Omega + \int_{4\pi} \kappa_i n_i^2 I_{b,i} d\Omega + \int_{4\pi} \frac{\sigma_{s,ii}}{4\pi} \int_{4\pi} I_i(\hat{\mathbf{s}}_i) \Phi_{ii}(\hat{\mathbf{s}}_i, \hat{\mathbf{s}}) d\Omega_i d\Omega \\ & + \int_{4\pi} \frac{\sigma_{s,ji}}{4\pi} \int_{4\pi} I_j(\hat{\mathbf{s}}_i) \Phi_{ji}(\hat{\mathbf{s}}_i, \hat{\mathbf{s}}) d\Omega_i d\Omega, \quad i, j = 1, 2; i \neq j \end{aligned} \quad (3.15)$$

and,

$$\begin{aligned} \nabla \cdot \int_{4\pi} I_i \hat{\mathbf{s}} d\Omega = & 4\pi \kappa_i n_i^2 I_{b,i} - \int_{4\pi} \beta_i I_i(\hat{\mathbf{s}}) d\Omega + \frac{\sigma_{s,ii}}{4\pi} \int_{4\pi} I_i(\hat{\mathbf{s}}_i) \left( \int_{4\pi} \Phi_{ii}(\hat{\mathbf{s}}_i, \hat{\mathbf{s}}) d\Omega \right) d\Omega_i \\ & + \frac{\sigma_{s,ji}}{4\pi} \int_{4\pi} I_j(\hat{\mathbf{s}}_i) \left( \int_{4\pi} \Phi_{ji}(\hat{\mathbf{s}}_i, \hat{\mathbf{s}}) d\Omega \right) d\Omega_i, \quad i, j = 1, 2; i \neq j \end{aligned} \quad (3.16)$$

Moreover, it was shown by Modest <sup>(115)</sup> that

$$\frac{1}{4\pi} \int_{4\pi} \Phi(\hat{\mathbf{s}}_i, \hat{\mathbf{s}}) d\Omega = 1 \quad (3.17)$$

Hence, substituting Equations (3.14) and (3.17) into Equation (3.16) leads to

$$\begin{aligned} \nabla \cdot \mathbf{q}_{r,i}(\mathbf{r}) = & 4\pi\kappa_i n_i^2 I_{b,i} - \beta_i \int_{4\pi} I_i(\hat{\mathbf{s}}) d\Omega + \sigma_{s,ii} \int_{4\pi} I_i(\hat{\mathbf{s}}_i) d\Omega_i \\ & + \sigma_{s,ji} \int_{4\pi} I_j(\hat{\mathbf{s}}_i) d\Omega_i, \quad i, j = 1, 2; i \neq j \end{aligned} \quad (3.18)$$

Finally, Equation (3.13) shows that  $\kappa_i = \beta_i - (\sigma_{s,ii} + \sigma_{s,ji})$ , considering  $\Omega$  and  $\Omega_i$  as dummy arguments for the integration over all solid angles, results in:

$$\nabla \cdot \mathbf{q}_{r,i}(\mathbf{r}) = \kappa_i \cdot \left( 4\pi n_i^2 I_b - \int_{4\pi} I(\hat{\mathbf{s}}_i) d\Omega_i \right), \quad i, j = 1, 2; i \neq j \quad (3.19)$$

The absorption through one phase is described by an exponential decrease in intensity over a geometrical path  $d$  while moving through a participating medium, as shown in Equation (3.20).

$$I(d) = I(0) e^{-\tau} \quad (3.20)$$

where the optical thickness,  $\tau$ , is defined as:

$$\tau = \int_0^d \kappa ds \quad (3.21)$$

In the case where  $\kappa$  is constant through the medium, Equations (3.20) and (3.21) are transformed to

$$\tau = \kappa d \quad (3.22)$$

$$I(d) = I(0) e^{-\kappa d} \quad (3.23)$$

#### 3.3.1 Implementation

Equation (3.19) was integrated using a 3D path length-based Monte-Carlo (MC) code developed in `fortran90` to calculate directly the divergence of the radiative heat flux at all positions of the simulation domain. Practically, the divergence of the radiative heat flux is calculated as in Equation (3.24).

$$(\nabla \cdot \mathbf{q}_{r,\text{tot}}(\mathbf{r}))_{\text{cell}} = \frac{1}{V_{\text{cell}}} (P_{\text{em,cell}} - P_{\text{abs,cell}}) \quad (3.24)$$

where  $P_{\text{em,cell}}$  and  $P_{\text{abs,cell}}$  are the total power emitted and absorbed in one mesh cell respectively, while  $V_{\text{cell}}$  is the volume of that mesh cell.

Figure 3.2 shows the algorithm implemented in the 3D MC code calculating  $P_{\text{em,cell}}$  and  $P_{\text{abs,cell}}$ , considering emission from a boundary face or an internal cell. All calculations are done from a unique wavelength of  $1 \mu\text{m}$ . The code supports emission from the boundaries due to two types of BCs: incoming radiative heat flux and fixed wall temperature. Equations (3.25)

### 3.3. Radiative heat transfer: Monte-Carlo radiation code

and (3.26) define the power transported by one ray,  $P_{0,\text{ray}}$ , emitted from a boundary face in the case of incoming radiative flux and fixed temperature BCs respectively. The power of one ray emitted from an internal cell at a temperature  $T_{\text{cell}}$  is given in Equation (3.27).

$$P_{0,\text{ray}} = \frac{\varepsilon_{\text{vis}} q_{\text{r,inc}} A_{\text{face}}}{N_{\text{rays,face}}} \quad (3.25)$$

$$P_{0,\text{ray}} = \frac{\varepsilon_{\text{IR}} \sigma_B T_{\text{face}}^4 A_{\text{face}}}{N_{\text{rays,face}}} \quad (3.26)$$

$$P_{0,\text{ray}} = \frac{4n_i^2 \kappa_i \sigma_B T_{\text{cell}}^4 V_{\text{cell}}}{N_{\text{rays,cell}}(T_{\text{cell}})} \quad (3.27)$$

$\varepsilon_{\text{vis}}$  corresponds to the emissivity of the material in the visible wavelength range because HFSS radiation is considered for the incoming radiative heat flux BC, and the wavelength range of emission is the visible range as shown by Bader et al.<sup>(101)</sup>. The emissivity of the material in the IR wavelength range,  $\varepsilon_{\text{IR}}$ , is used for emission in the case of a temperature BC because Wien's law of displacement (Equation (3.28)) gives a wavelength of maximum emission of  $1.45 \mu\text{m}$ , which correspond to a maximum surface temperature of 2000 K.  $A_{\text{face}}$  is the area of the cell face from which the ray is emitted.  $N_{\text{rays,face}}$  is the number of rays emitted from one cell face. The total power emitted by one face is divided by  $N_{\text{rays,face}}$  such that all rays emitted from that face transport the same total power, which guarantees the conservation of energy. The division of the total power emitted by one cell by  $N_{\text{rays,cell}}(T_{\text{cell}})$  also ensures energy conservation for internal emission.  $N_{\text{rays,cell}}(T_{\text{cell}})$  is the number of rays emitted by a cell at  $T_{\text{cell}}$ .  $V_{\text{cell}}$  is the cell volume,  $\sigma_B$  the Stefan-Boltzmann constant.

$$\lambda_{\text{max}} = \frac{2898 \cdot 10^{-6}}{T} \quad (3.28)$$

A characteristic of this code is that no phase is pre-determined for each cell or face of the computational domain. Before a ray is emitted, a random number is generated and compared to the porosity,  $\phi$ . If it is smaller than the porosity, the ray is sent from the gas phase and, otherwise, from the solid phase.

The temperature dependence of  $N_{\text{rays,cell}}$  is the result of a trade-off between a high number of rays to avoid fluctuations of  $\nabla \cdot \mathbf{q}_{\text{r,tot}}$  and computational cost. Indeed, the higher the number of rays per cell the lower the energy per emitted ray (Equation (3.27)) but the higher the computational cost. Cells with low temperature emit less power and less rays are necessary to keep the energy emitted per ray within reasonable limits. On the contrary, the number of rays emitted per cell must be increased with temperature. An analysis based on the coupled conduction-radiation algorithm (PATORAC, Section 3.4) led to the temperature dependence

of  $N_{\text{rays,cell}}$  defined in Equation (3.29).

$$N_{\text{rays,cell}}(T_{\text{cell}}) = \begin{cases} N_{\text{rays,cell,base}} & \text{if } T_{\text{cell}} \leq 500 \text{ K}, \\ N_{\text{rays,cell,base}} \left( \frac{T_{\text{cell}}}{550} \right)^4 & \text{if } T_{\text{cell}} \leq 1000 \text{ K}, \\ N_{\text{rays,cell,base}} \left( \frac{T_{\text{cell}}}{550} \right)^4 (T_{\text{cell}} - 999)^{0.12} & \text{else} \end{cases} \quad (3.29)$$

where  $N_{\text{rays,cell,base}}$  is the reference number of rays per cell given as an input to the code. It is typically between 20 and 100 rays depending on the desired accuracy. The starting point  $\mathbf{p}$  on a boundary face and the starting point and direction  $\mathbf{t}$  in a cell are determined stochastically. The direction  $\mathbf{t}$  depends on the assumption made for the BC: diffuse or directional. The *Trace Ray* algorithm presented in Figure 3.3 then propagates the ray through the material until it is absorbed, and the MC algorithm is repeated for  $N_{\text{rays,cell}}$  or  $N_{\text{rays,face}}$ .



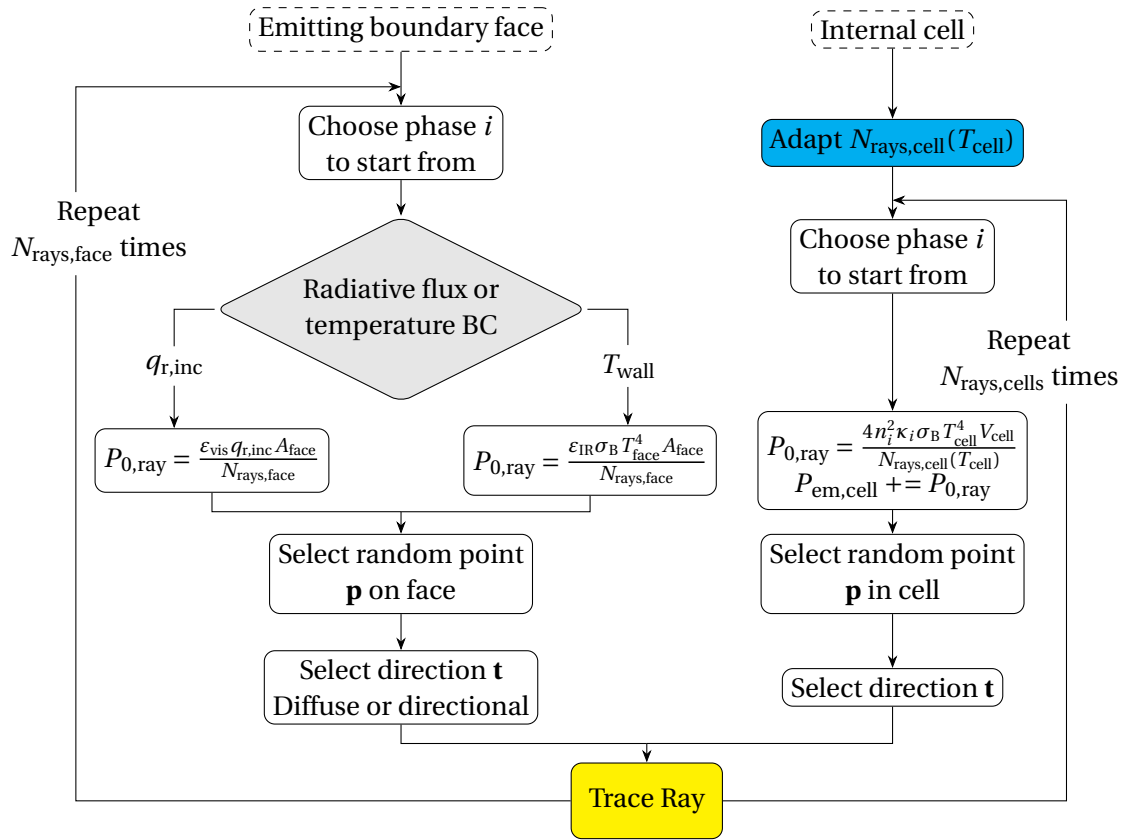


**Figure 3.2** – Path-length Monte-Carlo Algorithm. The "Trace Ray" function is described in Figure 3.3

Figure 3.3 shows the way a ray is traced in the two-phase medium and works as following.

---

**Input:**  $P_0$ , phase  $i$ ,  $\mathbf{p}$ ,  $\mathbf{t}$

Get the effective radiative properties of phase  $i$ ;

```

1 The extinction length  $L_{\text{ext}}$  is calculated using a random number  $R_\beta$ :  $L_{\text{ext}} = \frac{1}{\beta_i} \log\left(\frac{1}{R_\beta}\right)$ ;
while  $P_0 > P_{\text{lim}}$  do
2   Find next face and next point from the starting point  $\mathbf{p}$  in direction  $\mathbf{t}$  and the
     corresponding distance traveled by the ray in the present cell,  $d$ , is extracted;
     if  $d \leq L_{\text{ext}}$  then
       No extinction event in current cell;
       The cell absorbs energy corresponding to distance  $d$ :  $P_{\text{abs,cell}} += P_0(1 - e^{-\kappa d})$ ;
       The ray power is updated:  $P_0 = P_0 e^{-\kappa d}$ ;
       The remaining extinction length is updated:  $L_{\text{ext}} = L_{\text{ext}} - d$ ;
       if New point on boundary face then
         Generate random number  $R_{\text{bnd}}$ ;
         if  $R_{\text{bnd}} \leq \rho_{\text{face}}$  then // is  $R_{\text{bnd}}$  smaller than face reflectivity  $\rho_{\text{face}}$ ?
           Reflected ray: cycle (go back to line 2);
         else
           Absorbed ray;
           exit TraceRay algorithm and goes on with next ray;
         end
       else
         New point on inner face: cycle (go back to line 2);
       end
     else
       Extinction event in current cell;
        $d$  is updated and cannot be higher than  $L_{\text{ext}}$ :  $d = L_{\text{ext}}$ ;
       The cell absorbs energy corresponding to distance  $d = L_{\text{ext}}$ :  $P_{\text{abs,cell}} += P_0(1 - e^{-\kappa d})$ ;
       The ray power is updated:  $P_0 = P_0 e^{-\kappa d}$ ;
       if  $R_\sigma \leq \Omega_{i(i\pm 1)}$ ? then // is  $R_\sigma$  is smaller than scattering albedo  $\Omega_{i(i\pm 1)}$ 
         Scattered;
         if  $R_\sigma \leq \Omega_{ii}$ ? then // is  $R_\sigma$  smaller than scattering albedo  $\Omega_{ii}$ 
           Scattered to phase 1 (go back to line 1);
         else
           Scattered to phase 2 (go back to line 1);
         end
       else
         Absorbed ray:  $P_{\text{abs,cell}} += P_0$ ;
         exit TraceRay algorithm and goes on with next ray;
       end
     end
  end
end

```

---

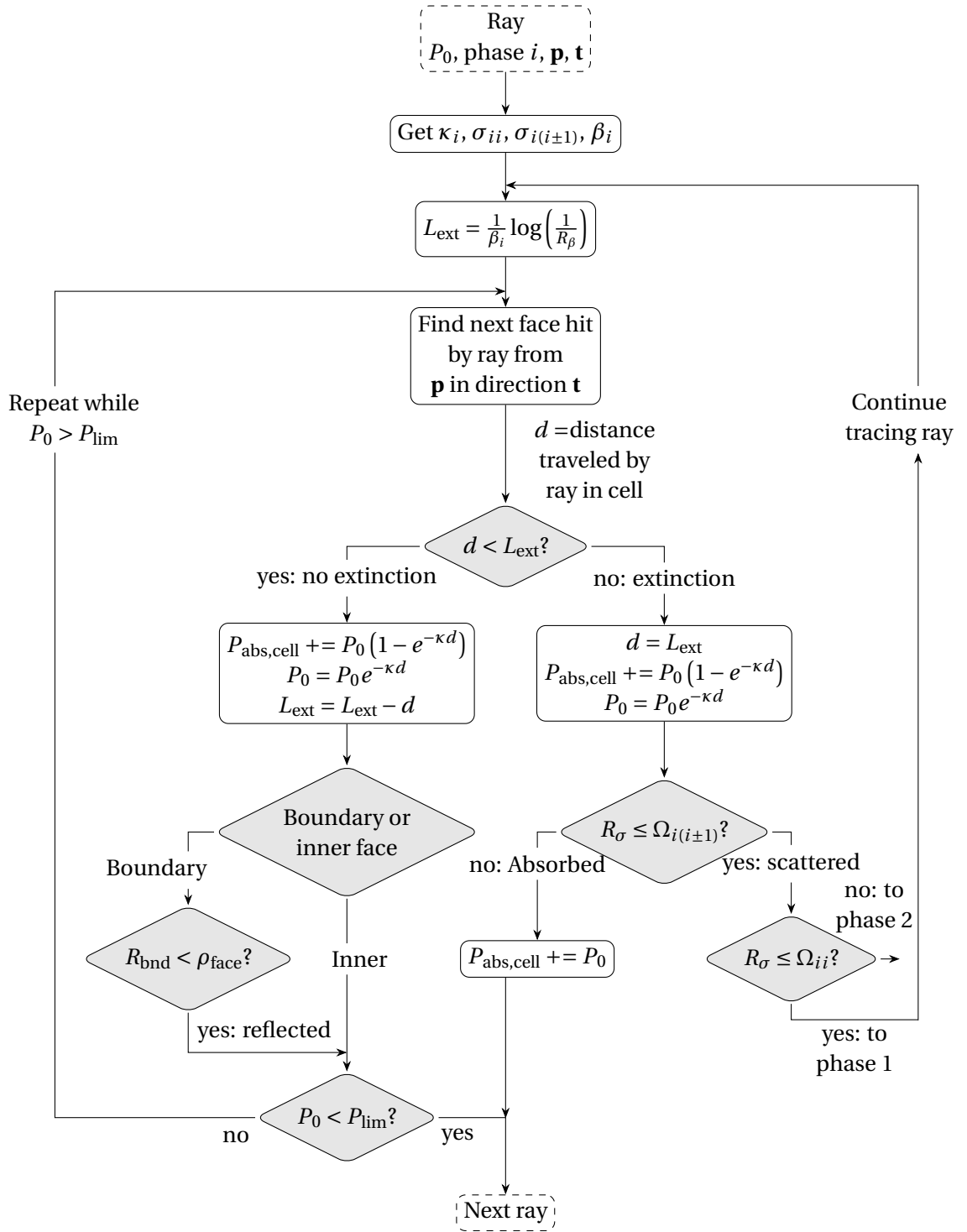


**Figure 3.3** – TraceRay function algorithm.

### 3.3.2 High performance computing considerations

The MC code was parallelised to decrease its computational time. Since all rays are independent from each other, the parallelisation was simple to implement. However, since each process stores the values of  $P_{em}$  and  $P_{abs}$  for the whole mesh,  $P_{em}$  and  $P_{abs}$  are matrices that need to be summed element by element at the end of the MC simulation, facing a so-called race condition in high-performance computing (HPC). No operator to perform such an operation is available in `fortran90`. Therefore, a custom reduce operator was coded to overcome this issue.

First, a subroutine describing the way the two matrices (vectors) should be added element by element was defined as following:

```
SUBROUTINE E2eSumMPI(IN, INOUT, LEN, DATATYPE)
```

```
!-----  
! Arguments  
!-----
```

```
  INTEGER :: LEN, DATATYPE  
  REAL(DP) IN(LEN), INOUT(LEN)  
  INTEGER :: i  
  
  DO i = 1, LEN  
    INOUT(i) = IN(i) + INOUT(i)  
  END DO
```

```
END SUBROUTINE E2eSumMPI
```

The custom MPI (Message passing interface) operator was created using the `fortran90` operator creator. `E2eSumMPI` corresponds to the routine previously defined, and `MPI_E2eSUM` to the operator that can be used in an MPI reduce operation.

```
CALL MPI_OP_CREATE(E2eSumMPI, 1, glob%mpiInfo%MPI_E2eSUM, glob%mpiInfo%ef)
```

Finally, a blocking MPI reduce operation is performed using the `MPI_E2eSUM` operator, adding up all `EmittedLoc` vectors calculated by each processor into the `EmittedGlob` vector containing the final result.

```
CALL MPI_REDUCE(EmittedLoc(:), EmittedGlob(:), &  
  size(EmittedGlob(:)), MPI_REAL8, glob%mpiInfo%MPI_E2eSUM, IOPROC, MPI_COMM_WORLD,  
  glob%mpiInfo%ef)
```

The last piece of computational time optimization was done by implementing load balancing into the code. Indeed, arbitrarily distributing cells to processors could lead to a situation where some processors would have much more rays to trace than others, leading to a important loss of computational efficiency. Instead, cells were smartly distributed such that an equal number of rays was treated by each processor.

### 3.4 Radiation-conduction coupling algorithm: PATORAC

The PATORAC algorithm allows to simulate the thermal response of materials by processing conduction and radiation contributions separately, in opposition to the ETC model where radiation is accounted for in the effective conductivity  $\mathbf{k}_{\text{eff}}$ . The divergence of the radiative heat flux, which calculation was detailed in the previous section, is used to add an extra term to the energy conservation equation (Equation (3.3)) as following:

$$\partial_t(\rho_p e_p) + \nabla \cdot (\epsilon_g \rho_g h_g \mathbf{v}_g) + \nabla \cdot \sum_{k=1}^{N_g} (\mathcal{Q}_k) = \nabla \cdot (\mathbf{k}_{\text{cond}} \cdot \nabla T) + \mu \epsilon_g^2 (\mathbf{K}^{-1} \cdot \mathbf{v}_g) \cdot \mathbf{v}_g - \nabla \cdot \mathbf{q}_{\text{r,tot}} \quad (3.30)$$

The thermal conductivity  $\mathbf{k}_{\text{cond}}$  now only accounts for the conduction through the material. In the case of a material in which no thermochemical processes occur, Equation (3.30) is simplified into Equation (3.31).

$$\partial_t(\rho e) = \nabla \cdot (\mathbf{k}_{\text{cond}} \cdot \nabla T) - \nabla \cdot \mathbf{q}_{\text{r,tot}} \quad (3.31)$$

Figure 3.4 shows the algorithm that couples PATO and the MC solver called MCRAD. The BCs, heat flux or fixed temperature, can be applied on either the PATO or the MCRAD side. First, the mesh and corresponding temperature field have to be initialized. The mesh used in PATO (OpenFOAM) and MCRAD are identical such that the results of one can easily be used by the other part of the coupling algorithm. The first MCRAD calculation can then be performed to provide PATO with the divergence of radiative flux source term. The temperature field is updated by a PATO simulation for a given time. Generally, the MC simulation is not performed at every time step of the PATO simulation in order to save computational resources. The coupling steps can be adapted and they define the coupling frequency of the transient algorithm. A typical coupling step is defined by a PATO simulation, producing a temperature field that is used to perform an MCRAD iteration, which provides the divergence of the radiative flux for the temperature to be updated by a new PATO simulation.

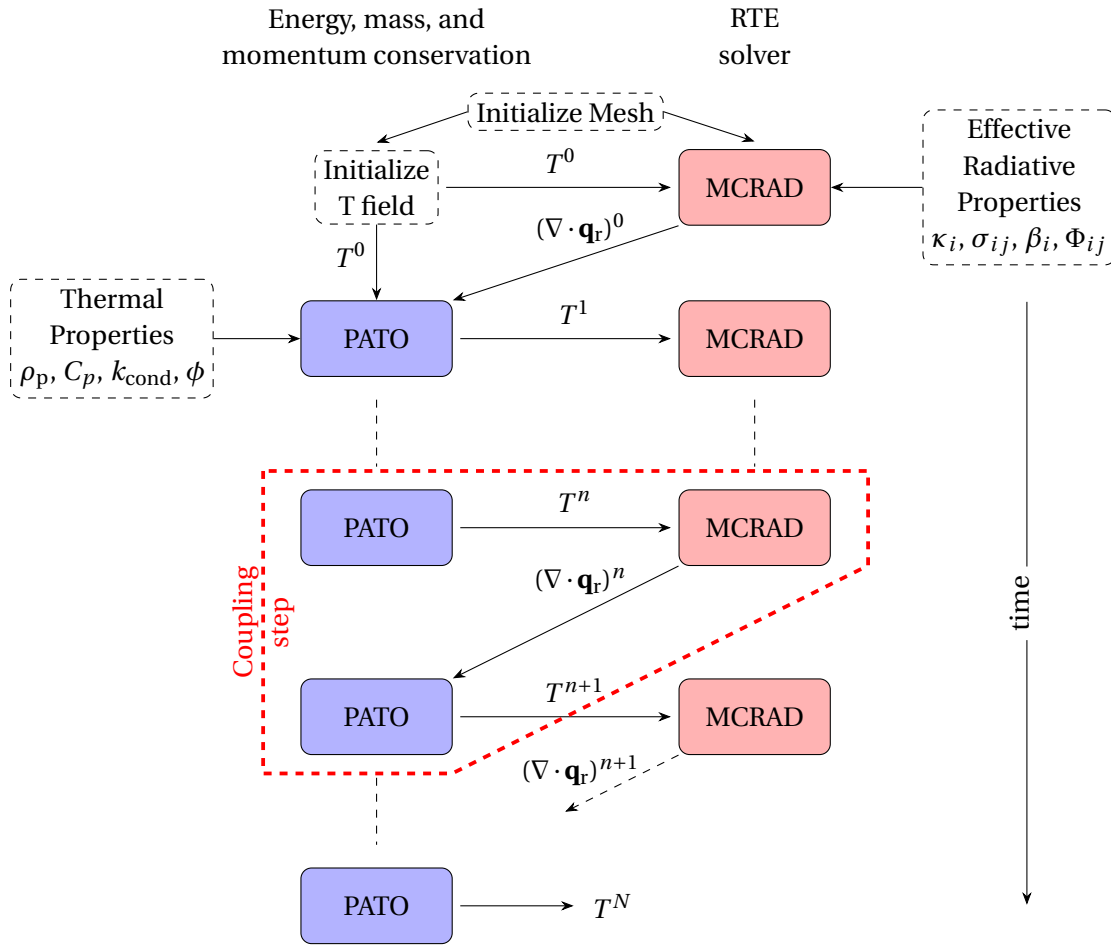


Figure 3.4 – PATORAC coupled transient algorithm.

## 4 Effective conductivity of highly porous ceramics in a radiative environment<sup>1</sup>

In this chapter, the pseudo-inverse methodology to determine the effective thermal conductivity (ETC) from experimental measurements in the High-Flux Solar Simulator (HFSS) is applied to evaluate the ETC of highly porous ceramic samples for a temperature range of more than 1000 K.

The first part of the chapter describes and evaluates the properties of the samples considered. The second part gives methodology complements to the approach defined in Section 3.2 for the coupled numerical-experimental simulations. In the third part of the chapter, the corresponding ETCs for all samples are presented.

### 4.1 Sample properties

Pure alumina and AS foam samples were manufactured by the company de Cavis for the purpose of this work using a method that processes particle-stabilized wet foams into ceramics<sup>(116)</sup>.

U92 samples were made of a high purity (99.5 %) alumina foam that presents a porosity of approximately 92 % and a density of  $316 \text{ kg m}^{-3}$ . U75, U81 and U88 AS samples were produced with porosities of 75, 81, and 88 % and densities of 690, 532, and  $343 \text{ kg m}^{-3}$  respectively. The typical pore size of samples U92, U75, U81 and U88 were evaluated (using SEM images presented on Figure 4.1) to 80, 190, 230, and  $400 \mu\text{m}$  respectively. This yields typical extinction coefficients of 12500, 5260, 4350, and  $2500 \text{ m}^{-1}$  respectively, considering the approximation of the extinction coefficient being inversely proportional to the pore size ( $\beta = 1/D_p$ ). C88 samples were a composite composed of an 88 % porosity AS foam with a thin, dense AS foam layer on one side (with thickness 200 to  $400 \mu\text{m}$ ). Figure 4.1(e) represents the surface of the dense AS foam layer and shows no significant apparent porosity. Table 4.1 gives the sample types that were tested in EPFL's HFSS<sup>(101,102)</sup> with the corresponding peak heat flux, and the

---

<sup>1</sup>Material from this chapter has been accepted for publication: J. Mora-Monteros, C. Suter, S. Haussener. Effective conductivity of porous ceramics in a radiative environment. *Ceramics International*, 2019<sup>(107)</sup>

## Chapter 4. Effective conductivity of highly porous ceramics in a radiative environment

abbreviations that will be used to identify them.

**Table 4.1** – The list of experimentally investigated sample types, flux levels, densities, porosities, typical extinction coefficient  $\beta$ , and the abbreviations used for the various sample types. \* denotes typical values averaged over the composite.

Material	Flux level ( $\text{MW m}^{-2}$ )	Density ( $\text{kg m}^{-3}$ )	$\phi$ (vol%)	$\beta$ ( $\text{m}^{-1}$ )	coated	Abbreviation
$\text{Al}_2\text{O}_3$	1.5	316	92	12500	no	U92
AS	1.0	690	75	5260	no	U75
AS	1.0	532	81	4350	no	U81
AS	1.0	343	88	2500	no	U88
AS	0.14	343	88	2500	no	U88LF
AS	1.0	376*	86*	2500	yes	C88

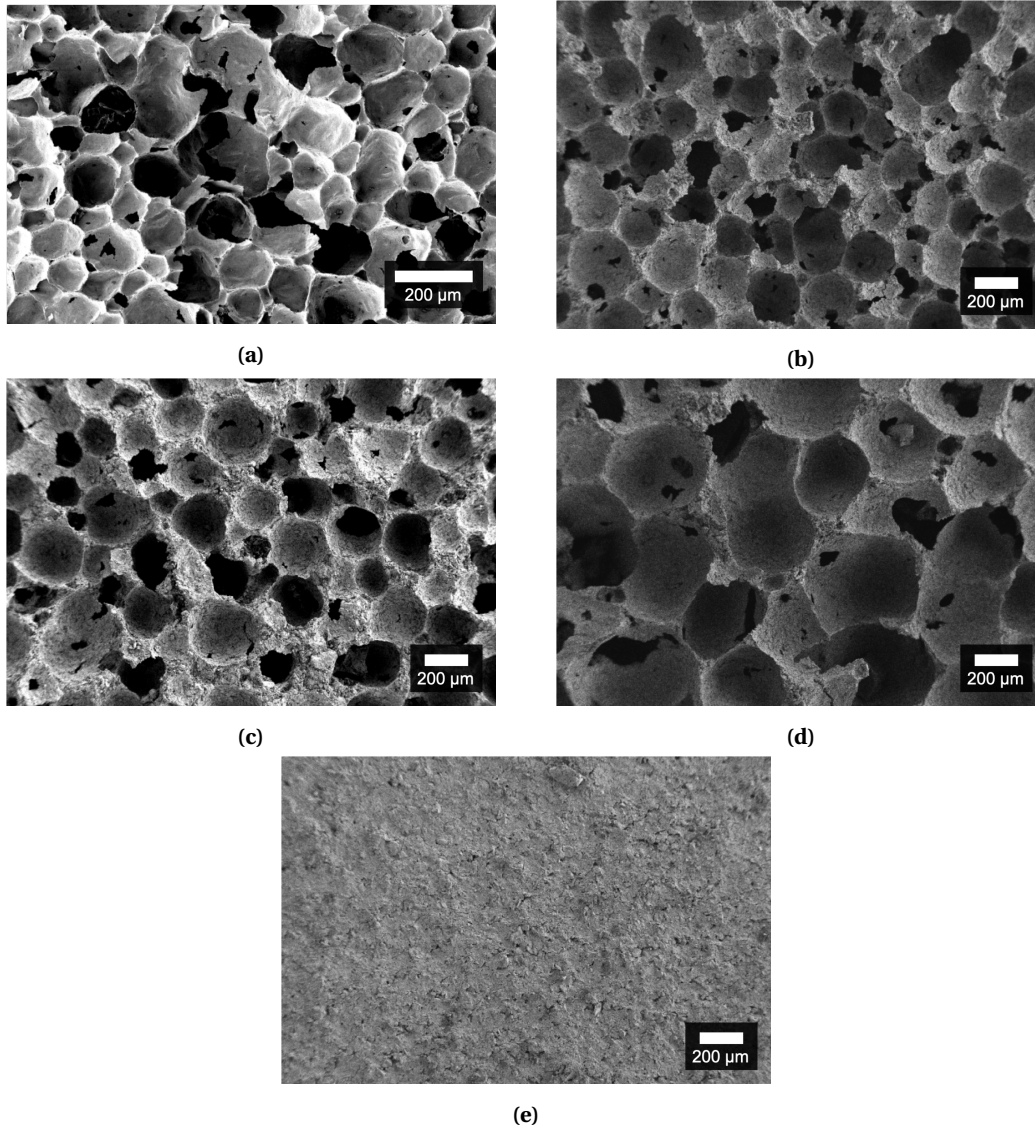


**Figure 4.1** – SEM images of the studied samples surfaces: (a) U92, (b) U75, (c) U81, (d) U88, (e) C88.



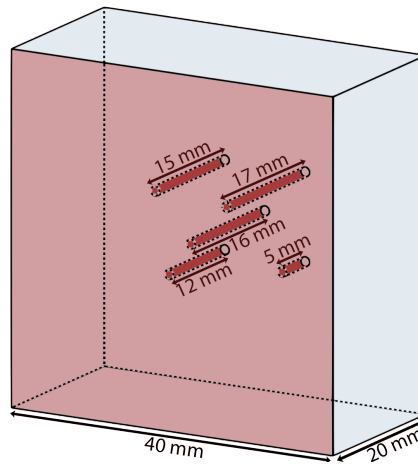


**Figure 4.2** – Shape and size of the investigated samples. The red surface corresponds to the surface exposed to the radiative flux. The thermocouples arrangement is shown in darker red, with hole depths indicated from the back face.

The diverse samples allow for comparing materials, studying the influence of the morphology (specifically the porosity), or investigating the effect of the thin, dense layer on the ETC. Table 4.2 explains which sample type comparisons can be used to evaluate the influence of different parameters on the ETC.

**Table 4.2** – The experimental matrix investigated, indicating what sample comparison was done and what effect on ETC could therefore be investigated (indicated by the colors).

Sample type	C88	U88LF	U88	U81	U75	U92
U92	not used		Material comparison	not used		
U75	Influence of porosity on ETC					
U81						
U88	Influence of pure radiative heat flux on ETC					
U88LF						
C88						

The samples were manufactured with dimensions of 40x40x20 mm<sup>3</sup>. Each sample had machined holes with precision of  $\pm 0.1$  mm and depths of 3, 4, 5, 8, 15 mm from the irradiated surface for the positioning of thermocouples. The hole at 4 mm depth was centered, while the other four holes (at depths 3, 5, 8, 15 mm) were arranged in a rectangle with edge length of 1 mm around the center as shown in Figure 4.2.

## 4.2 Methodology complements

The ETC algorithm described in Section 3.2 using PATO was utilized to model the thermal response of the studied samples and to determine their ETCs. Specific boundary conditions are detailed for the accurate modeling of the physical heat transfer processes taking place on the samples surfaces.

### 4.2.1 Boundary conditions

The measured surface temperatures of the exposed surface were used as boundary conditions. Thus, a mapped time-dependent Dirichlet boundary condition was set on the irradiated face of the sample. In these conditions a radiative flux boundary condition would have been more physical as the samples are exposed to a flux from the HFSS. Even though a temperature measured with the IR camera assumes a fixed emissivity it allows to overcome many uncertainties resulting from unknown heat losses on the exposed surface in the case of a flux boundary condition. The areas in contact with the water-cooled sample holder were set to a fixed temperature of 288 K. For the lateral and rear faces of the sample, a flux boundary condition based on mixed reradiation-convection was set. We assumed forced convection on the sides faces due to global ventilation in the experimental room, and a natural convection on the back face. Considering a laminar flow on flat plates with a velocity of  $1 \text{ ms}^{-1}$ , the Nusselt number on the sides faces was 31, yielding a heat transfer coefficient of  $20 \text{ W m}^{-2} \text{ K}^{-1}$ . Re-radiation is then added to complete the boundary condition. A Nusselt correlation on the back face gave a heat transfer coefficient of  $5 \text{ W m}^{-2} \text{ K}^{-1}$ . The convective heat transfer coefficient was multiplied by a factor to account for surface roughness that depends on porosity and pore size. The factor was 1.2, 2, and 5 for samples U75, U81, and U88 respectively. These empirical factors allowed for a better fitting of the numerical results to the experimental measurements.

### 4.2.2 Numerical considerations

#### Mesh study

The mesh refinement study in both  $x$ - and  $y$ -directions (see Figure 2.1(a)) revealed that relative errors were below 1 % for all positions where temperatures were recorded for a mesh with  $20 \times 20$  cells compared to a mesh with  $60 \times 60$  cells (considered as the reference solution, both 100 cells in the  $z$ -direction). This error corresponds to an absolute error of 12 degrees for the highest temperature, occurring at 4 mm from the surface. No clear improvement could be noticed when refining the mesh. Considering that experimental errors (see paragraph *Measurement errors*, Section 2.1.5) can be up to 40-50 K, a mesh of  $20 \times 20$  cells is sufficient.

The mesh refinement study in the longitudinal direction showed that a mesh of 100 cells in the  $z$ -direction was needed to reach a relative error below 1 %. Indeed, a mesh with 50 cells in the  $z$ -direction induced a relative difference of up to 2 % with the reference solution (200 cells). The improvement was not significant when increasing the number of cells from 100 to 200. Therefore, 100 cells were used in the  $z$ -direction for this work.

#### Solver and convergence criteria

As an OpenFOAM toolbox, PATO is using a stabilized preconditioned (bi-)conjugate gradient solver, coupled with a diagonal incomplete-LU preconditioner, to solve all sets of equations<sup>(117)</sup>. The solution was considered converged when the residuals of the energy equation

solver (inner loop) was smaller than  $10^{-6}$ . The 2-norm error  $\epsilon$  relative to the results with a tolerance of  $10^{-7}$  (subscript "ref") was used as a measure of accuracy for all positions (subscript "i"):

$$\epsilon = \frac{\|T_i - T_{i,\text{ref}}\|_2}{\|T_{i,\text{ref}}\|_2} \quad (4.1)$$

A value of  $10^{-6}$  for the solver tolerance was necessary to guarantee a value of  $\epsilon$  below  $10^{-6}$  for all temperatures.

## 4.3 Results and discussion

### 4.3.1 Validation of computational model

Figure 4.3 shows the comparison between numerical and experimental temperature profiles for sample U88.

Figure 4.3(a) presents the center ( $x = 20$  mm,  $y = 20$  mm) temperature of the irradiated surface and the solid temperatures at the five positions in the sample foam as a function of time.  $R^2$  values for the whole duration of tests were 0.998, 0.942, 0.993, 0.997 and 0.904 at 4 mm, 3 mm, 5 mm, 8 mm, and 15 mm depth, respectively. The relative differences between experimental and numerical values at steady state ( $t > 300$ s) regime were 0.5 %, 0.52 %, 0.24 %, 0.05 % and 5.29 % at the same depths. A fundamental difference was observed in the transient phase ( $t = 0 - 300$ s) of the temperature profiles at 3 and 5 mm depths, where numerical values are up to 37.3 % and 12.6 %, respectively, higher than experimental ones, while the temperature at 4 mm depth matches well for the whole duration of the experiment ( $R^2 = 0.998$ , maximum relative difference of 4.6 %). We hypothesize that these differences come from the assumption of the ETC being isotropic. As shown by Mendes et al. <sup>(28)</sup>, the ETC is expected to be 25 % larger in the main direction of heat transfer. In this case, decreasing the ETC in cross directions ( $x$  and  $y$ ) will reduce the off-center temperatures at depths of 3 and 5 mm. Another possibility could be coming from the effect of incoming radiation described in Section 4.3.2 and 4.3.3. The discrepancies observed for TCs at 3 and 5 mm could be the consequence of the non-uniformity of the irradiation on the surface.

Figure 4.3(b) displays the evolution of the temperatures at the five positions in the sample foam with time of the temperature profiles through the sample. The vertical error bars represent the temperature differences induced by a numerical shift of the positions of  $\pm 0.2$  mm. It can hence be noticed that experimental values lie in these margins in the steady state regime ( $t = 300 - 600$ s). The temperature differences described previously for depths of 3 and 5 mm during the transient phase appear more clearly, even though not depicting the disparities in slopes. The horizontal error bar correspond to the experimental uncertainty in the depths of thermocouples. It can therefore be seen that differences between numerical and experimental values could come from differences in thermocouple positions.

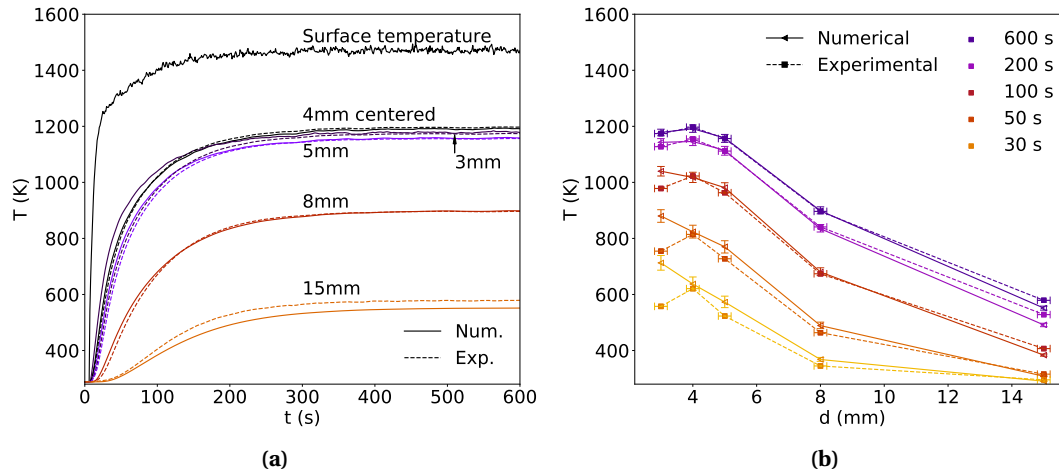


**Figure 4.3** – Comparison between numerical data and thermocouple measurements at five different depths, for the sample U88 that was exposed to a  $1 \text{ MWm}^{-2}$  peak radiative flux. The numerical data is compared to (a) measurements in function of time, and (b) measurements as a function of sample depth (for different locations in the  $xy$ -plane) at different times (dots: experiments, connected lines: numerical results). The measured temperatures lie within an error margin of the numerical results, obtained by numerically shifting the probe positions by  $\pm 0.2 \text{ mm}$  (b).

Overall, experimental and numerical temperature profiles match within reasonable margins ( $R^2 > 0.9$  for the whole duration of the test, relative error  $< 1 \%$  in steady-state regime for all thermocouples but the deepest -15 mm- one probably due to uncertainties in the back face boundary condition). The temperature analyses of the five others sample types (Table 4.1) shows similar behaviour and is summarized in Table 4.3.

**Table 4.3** – Summary of values representative of the goodness of fit for temperature analyses for the five other types of sample presented in this work.

	4 mm	3 mm	5 mm	8 mm	15 mm
Sample	Goodness of fit, $R^2$ value				
U92	0.941	0.954	0.962	0.974	0.984
U75	0.989	0.985	0.996	0.982	0.902
U81	0.991	0.975	0.992	0.990	0.943
U88	0.998	0.943	0.993	0.997	0.904
U88LF	0.992	0.981	0.994	0.999	0.927
C88	0.988	0.976	0.996	0.991	0.900
Steady state relative error in %					
U92	1.75	0.76	1.59	1.46	1.74
U75	0.93	1.14	0.77	0.67	0.08
U81	0.02	0.54	0.6	0.75	0.37
U88	0.5	0.5	0.2	0.05	5.29
U88LF	0.11	0.79	0.23	0.09	1.8
C88	0.84	0.78	0.25	1.15	2.29

### 4.3.2 Influence of porosity

Figure 4.4 shows a comparison of the ETC for three investigated samples types (Table 4.1) as a function of the temperature. The temperature ranges are limited by the maximum temperature difference between the surface and initial temperatures. Figure 4.4(a) depicts the ETC as a function of the temperature for samples U75, U81, and U88. The ETC increases monotonically with temperature from  $0.25 \text{ W m}^{-1} \text{ K}^{-1}$  at 286 K to  $0.47 \text{ W m}^{-1} \text{ K}^{-1}$  at 1324 K, from  $0.19 \text{ W m}^{-1} \text{ K}^{-1}$  at 286 K to  $0.3 \text{ W m}^{-1} \text{ K}^{-1}$  at 1374 K, and from  $0.16 \text{ W m}^{-1} \text{ K}^{-1}$  at 286 K to  $0.28 \text{ W m}^{-1} \text{ K}^{-1}$  at 1474 K for samples U75, U81, and U88 respectively.

The ETC is generally expected to increase with increasing temperature and solid fraction. This is verified for all three samples. Sample U88 exhibits a strong dependence on  $T^3$  ( $R^2$  value of 0.998 for a curve fit with a cubic function), which is expected in the presence of high temperature radiation in such porous materials. The dependence on  $T^3$  decreases for U81 and U75 ( $R^2$  values of 0.989 and 0.981 for a curve fit with a cubic function for samples U81 and U75 respectively), indicating that radiation effects are less dominant in those samples.

Figure 4.4 (b) shows the variation of the ETC in function of the samples solid fraction at six different temperatures. For conduction-only dominated problems, the value of ETC is expected to decrease with the solid fraction, reaching a value corresponding to that of thermal conductivity of air at low temperatures (i.e.  $0.025 \text{ W m}^{-1} \text{ K}^{-1}$ ).

While the trend between a solid fraction of 0.25 (sample U75) to 0.19 (sample U81) would lead to such a value for a solid fraction of 0.0, the ETC profile bends for a solid fraction of 0.12 (sample U88) to values indicating that radiation affects the heat transfer through sample U88 also at low temperatures. This effects comes from the incoming radiation of the surface of sample in the HFSS facility.

A value of  $2500 \text{ m}^{-1}$  for the extinction coefficient means that radiation can penetrate the sample (typical penetration length of  $400 \mu\text{m}$ ) and therefore affects the ETC of sample number U88. Indeed, at a depth of 1 mm, with the assumption of a gray and diffuse medium following Beer-Lambert law, 8.2 % of the initial radiation intensity is left, which is not negligible, showing that incoming radiation influences the thermal response of an 88 % porosity alumina-silicate sample and therefore its ETC, especially at low temperatures.

Samples U81 and U75 exhibit smaller typical pore sizes than sample U88, implying larger extinction coefficients of 4350 and  $5260 \text{ m}^{-1}$  (i.e. typical penetration lengths of 230 and  $190 \mu\text{m}$ ), respectively. This explains why for U81 and U75 the ETCs are not affected by incoming radiation.

### 4.3.3 Influence of coating layer and magnitude of incoming radiative heat flux

The incoming radiative heat flux can affect the ETC. As we consider ETC to be a combination of the thermal conductivity of the porous media and of the radiation conductivity, we do not consider any radiation source term. Therefore, if the radiation can penetrate into the sample, temperatures inside the sample close to the surface will depend not only on conduction but also on incoming radiation, i.e. the boundary condition. Consequently, the ETC has to be

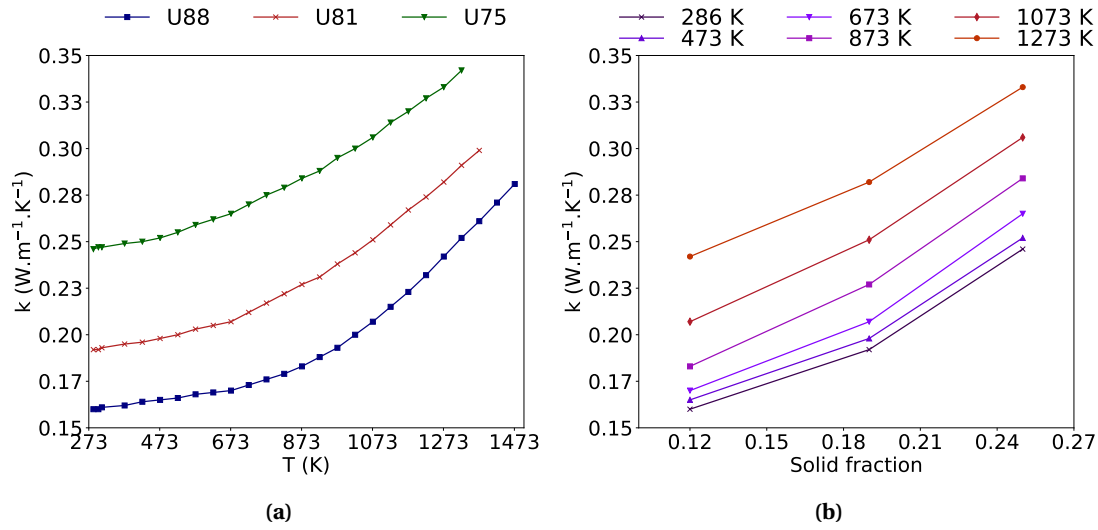


**Figure 4.4** – Comparison of the ETCs of Alumino-silicate samples U75, U81, and U88 in function of (a) the temperature, and (b) the solid fraction at six different temperatures.

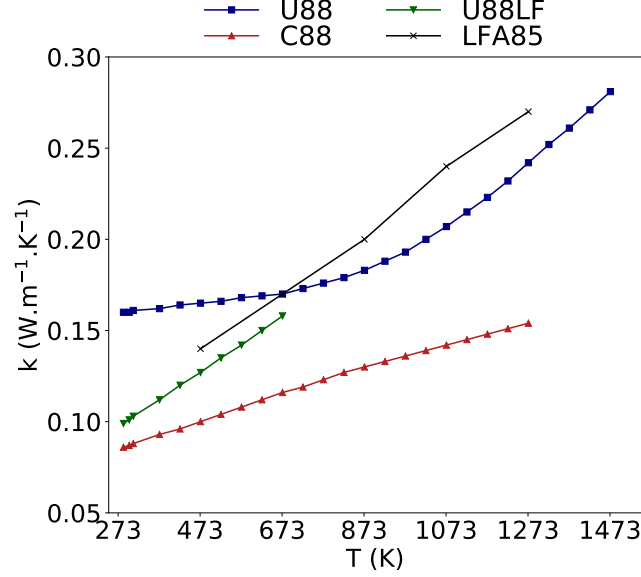
larger in order to fit the measured temperatures. The ETC depends on the boundary condition. The difference between U88 and C88 (Figure 4.5) indicates that the coating has a strong influence on the thermal response and hence the determined ETC. For sample C88, the ETC increases almost linearly from  $0.09 \text{ W}\cdot\text{m}^{-1}\cdot\text{K}^{-1}$  at 286 K to  $0.15 \text{ W}\cdot\text{m}^{-1}\cdot\text{K}^{-1}$  at 1274 K. The difference between C88 and U88 is between 28 and 46 % in the temperature range of 273 to 1473 K. Considering the thickness of the coating (200 to 400  $\mu\text{m}$ ), we assumed that the conduction heat transfer is not affected by the presence of such a layer. Therefore, the coating only affected the radiative heat transfer by preventing the incident radiative flux from penetrating into the sample.

Figure 4.5 compares U88 and U88LF, the material and porosity are identical but they were exposed to different peak radiative fluxes, i.e. U88 and U88LF were exposed to  $1 \text{ MW}\cdot\text{m}^{-2}$  and  $136 \text{ kW}\cdot\text{m}^{-2}$ , respectively. The comparison can only be done up to 723 K, given by the maximum surface temperature of sample U88LF.

The values and shape of U88LF's ETC confirm the hypothesis made in the previous section. An incident radiative heat flux with a peak value of  $136 \text{ kW}\cdot\text{m}^{-2}$  leads to an ETC that is between 7 and 38 % lower than with a high flux of  $1 \text{ MW}\cdot\text{m}^{-2}$ . This indicates that at lower levels of radiative heat flux and, hence, intensity, ETCs are less affected by the boundary condition. The ETC of sample U88LF remains 15 to 36 % higher than that of sample C88, showing that the thermal response is still affected by the incoming radiation that can penetrate the sample in the absence of coating.

Thermal conductivity obtained with a laser flash analysis (LFA) on an 85 % porosity sample is plotted in black. The comparison of the ETC with sample U88 at low temperature confirms the influence of incoming radiation. On the other hand, LFA values (between those of sample U88 and U81, see Figure 4.4(a), above 673 K) show that values obtained with the present

methodology are consistent with LFA measurements.



**Figure 4.5** – Influence of the boundary condition on the effective conductivity. The effective thermal conductivities of three 88 % porosity AS samples are compared to a laser flash analysis of an 85 % porosity sample (temperature-dependent thermal conductivity provided by the foam manufacturer). Samples U88 and C88 have been exposed to  $1 \text{ MW m}^{-2}$ , sample U88LF to  $136 \text{ kW m}^{-2}$ . The maximum temperature of the predicted ETC is limited to the maximum temperature reached at the surface of the sample, which was 723 K for the U88LF sample and 1473 K for the U88 sample.

#### 4.3.4 Material Comparison

Figure 4.7(a) displays a comparison between the ETC of a 92 % porosity pure alumina uncoated sample (U92) and the values obtained using the Kunii model, modified using the Ashby–Glicksman model, described by Shimizu et al.<sup>(118)</sup>, which expresses the ETC as :

$$k_{\text{eff}} = C(1 - \phi)k_b + k_a\phi^{1/3} + \overbrace{\left(\frac{2}{3}\right)10^{-6}(\alpha_r D_p)\phi^{1/3}}^{k_{\text{rad}}} \quad (4.2)$$

where  $C$  is a parameter taking into consideration the cell structure,  $k_b$  is the bulk thermal conductivity,  $k_a$  the thermal conductivity of air.  $C$  is expressed as:

$$C = \frac{2 - f_s}{3} \quad (4.3)$$

where  $f_s$  is the volume ratio of a strut to the total solid volume of a cell. Typically, for closed-cell structures exhibited by the studied materials  $f_s = 0$ , then  $C = \frac{2}{3}$ <sup>(118)</sup>. The radiative part of the ETC by Kunii-Ashby,  $k_{\text{rad}}$ , requires  $D_p$  (in  $\mu\text{m}$ ) the typical pore diameter of the sample and  $\alpha_r$

## Chapter 4. Effective conductivity of highly porous ceramics in a radiative environment

(in  $\text{W m}^{-2} \text{K}^{-1}$ ) the radiant heat transfer coefficient.  $\alpha_r$  is defined by Shimizu et al.<sup>(118)</sup> as:

$$\alpha_r = 0.1942\varepsilon \left( \frac{T}{100} \right)^3 \quad (4.4)$$

where  $\varepsilon$  is the emissivity of the material, and  $T$  the absolute temperature. For comparison, we replaced the  $k_{\text{rad}}$  of the Kunii-Ashby model (Equation (4.2)) by the Rosseland approximation of the radiative conductivity:

$$k_{\text{rad}} = \frac{16}{3} \frac{\sigma T^3}{\beta} \quad (4.5)$$

using the approximated, wavelength-independent extinction coefficient ( $\beta \approx 1/d$ ). The values obtained with the Kunii model and the Rosseland-modified Kunii-Ashby model are based on the range of bulk alumina and alumino-silicate conductivity values given by Shackelford and Alexander<sup>(119)</sup> for alumina and alumino-silicate, and from Zake-Tiluga et al.<sup>(36)</sup>, Barea et al.<sup>(120)</sup> and Coquard et al.<sup>(18)</sup> for alumino-silicate. The bulk values are shown in Figure 4.6.

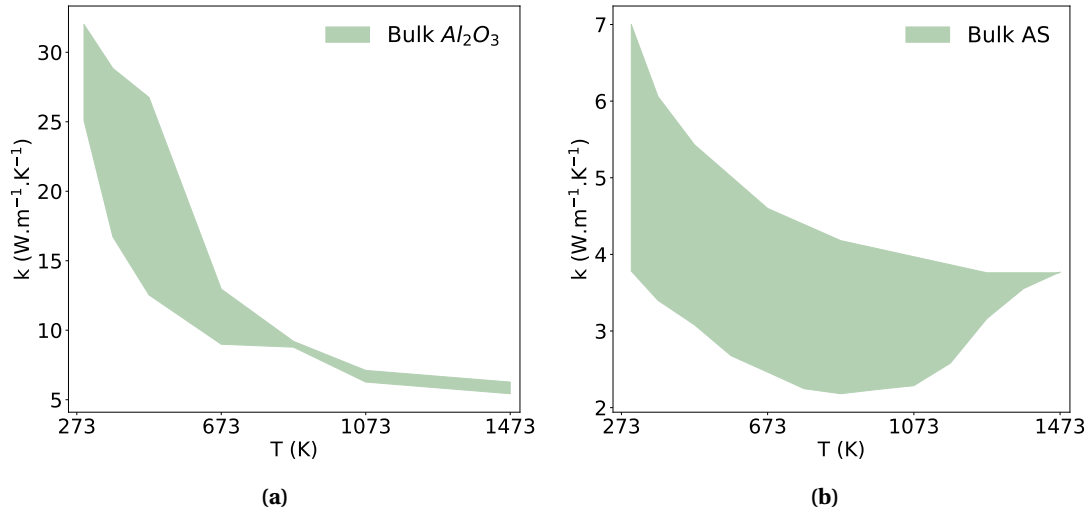


**Figure 4.6** – Temperature-dependent bulk conductivity ranges for (a) pure alumina and (b) alumino-silicate. The values were extracted from Shackelford and Alexander<sup>(119)</sup> for alumina and alumino-silicate, and from Zake-Tiluga et al.<sup>(36)</sup>, Barea et al.<sup>(120)</sup> and Coquard et al.<sup>(18)</sup> for alumino-silicate.

Figure 4.7(b) shows the comparison between U88 ETC values to values obtained using the modified Kunii model (using  $C = 0.25$ ), and the Litovsky model<sup>(121)</sup> to which the radiative conductivity of Kunii or Rosseland models part was added, giving:

$$k_{\text{eff}} = M(1 - \phi)^{3/2} k_b + k_a \phi^{1/4} + k_{\text{rad}} \quad (4.6)$$

where Litovsky suggested a thermal resistance parameter  $M$  of 0.55 for porous ceramics to account for grain boundaries and microcracks<sup>(122)</sup>.



We observe that the ETC of U92 decreases monotonically from  $2.0 \text{ W m}^{-1} \text{ K}^{-1}$  at room temperature to reach its minimum of  $0.56 \text{ W m}^{-1} \text{ K}^{-1}$  at  $1473 \text{ K}$ . Those numbers are consistent with what was reported by Mendes et al. <sup>(28)</sup>, or Zake-Tiluga et al. <sup>(36)</sup>. At room temperature, the ETC is about  $1.5 \text{ W m}^{-1} \text{ K}^{-1}$  for a sample with a porosity of  $89 \%$  <sup>(28)</sup>, and about  $3.0 \text{ W m}^{-1} \text{ K}^{-1}$  for a sample with a porosity  $70 \%$  <sup>(36)</sup>. The respective minimum values reported are  $0.45 \text{ W m}^{-1} \text{ K}^{-1}$  at  $1073 \text{ K}$  in the case of pure conduction <sup>(28)</sup> and  $1.07 \text{ W m}^{-1} \text{ K}^{-1}$  at  $1173 \text{ K}$  <sup>(36)</sup>. The ETC of U92 follows the trend presented by Mendes et al. <sup>(28)</sup> with the model considering heat transfer through pure conduction, which indicates that there is no influence of radiation on the ETC of sample U92. Our prediction of the extinction coefficient (of  $12500 \text{ m}^{-1}$ ) based on the analysis of SEM images indicated that incoming or internal radiation should not affect the ETC, in contrast to what was presented for the AS samples.

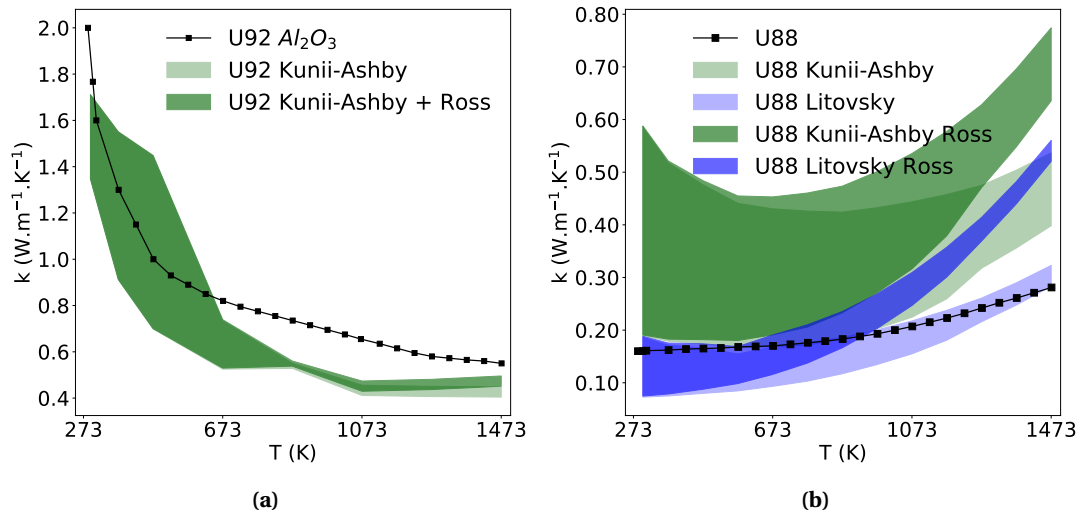


**Figure 4.7** – Comparison of the ETC of (a) U92 sample and (b) U88 sample, exposed to the same levels of peak radiative heat flux ( $1 \text{ MW m}^{-2}$ ). The black lines represent the conductivity of (a) U92 and (b) U88 obtained with the modified Kunii model <sup>(118)</sup>, considering closed-cell structures. The ETC of sample U88 is also compared to the modified Litovsky model. Comparisons to the Rosseland model with the corresponding conductivity extension (dark green and blue areas) are also made. Bulk conductivity values come or were extracted from Shackelford and Alexander <sup>(119)</sup> for U92 and U88, and Zake-Tiluga et al. <sup>(36)</sup>, Barea et al. <sup>(120)</sup> and Coquard et al. <sup>(18)</sup> for U88. The green, respectively blue, area in (b) corresponds to the range of ETC values obtained the modified Kunii model, respectively Litovsky model.

The comparison of the ETC of U92 with the Kunii and Rosseland-modified Kunii-Ashby (Equation (4.2) updated by Equation (4.5)) models confirms that the heat transfer mode is conduction dominated. Indeed, the contribution of the radiative part of the modified Kunii model to the ETC is negligible for such small pore sizes ( $80\text{-}100 \mu\text{m}$ ). The ETC of U92 is 3 % higher than the maximum ETC found with the modified Kunii model at  $300 \text{ K}$ . The ETC of U92 lies in the range of ETC given by the Kunii model up to  $623 \text{ K}$ , and is slightly higher between  $673$  and  $1473 \text{ K}$ , with a maximum relative difference of 30.4 % at  $1073 \text{ K}$ . There is a difference between the Kunii-Ashby model and the Rosseland-modified Kunii-Ashby model at the higher temperatures only ( $T > 873 \text{ K}$ ), where the Rosseland-modified model shows 15 % higher ETCs. The ETC of U92 is 12.5 times higher than that of U88 sample at room temperature, and 1.95

times higher at 1473 K.

The contribution of the radiative part of the ETC in both Kunii and Litovsky models is much more important in the case of U88. This can be explained by the pore diameter (400  $\mu\text{m}$ ), and by a much smaller bulk conductivity of alumino-silicate, which values were also taken from Shackelford and Alexander<sup>(119)</sup>, Zake-Tiluga et al.<sup>(36)</sup>, Barea et al.<sup>(120)</sup> and Coquard et al.<sup>(18)</sup>. The green and blue areas shown in Figure 4.7(b) correspond to ETC values obtained using the modified Kunii and Litovsky models, respectively. The ETC of U88 lies in the lower end of the range of values obtained by the modified Kunii model and in the higher end of those obtained using the Litovsky model. The Litovsky models appears to fit better the values of ETC determined for sample U88. The relative errors between the higher limit of the Litovsky model and the ETC of sample U88 are 16.4 % at 300 K, and 14.9 % at 1473 K.

If the Rosseland-modified models are used, a much stronger increase in ETC at higher temperatures is predicted than what we calculated. We associate this overestimation of the ETC by Rosseland for U88 by the intermediate optical thickness of our sample, i.e. in this case Rosseland is not applicable without doubt.

The discrepancy in ETC values obtained with the modified Kunii and Litovsky models shows that bulk conductivity values have a strong influence on ETC values given by such models. The range of bulk conductivities that can be found in the literature is wide, and depends on the detailed elemental composition of alumino-silicate materials.

The comparison between the values of ETC determined in this work and these models shows that our methodology provides reasonable predictions for the temperature-dependent ETC for highly porous materials.

### 4.4 Conclusions

A coupled experimental-numerical method was developed to determine effective thermal conductivities (ETCs) of ceramic foams made of alumino-silicate and pure alumina with different porosities. A 3D transient heat transfer model was developed and implemented in OpenFOAM assuming an isotropic effective thermal conductivity. The model results were compared to experimentally measured temperatures for ceramic foams exposed to a radiative flux environment. Our method numerically minimized the difference between numerically calculated and experimentally measured temperatures at five different locations inside of the samples. The influences of the material properties, morphology, and the operating conditions on the ETC were investigated.

A strong dependence of the ETC on  $T^3$  was noticed for the highest porosity alumino-silicate sample (U88), indicating that the contribution of radiative heat transfer was dominating. This dependence weakened as the porosity decreased for samples U81 and U75. Overall the ETC increased with increasing solid fraction of a sample. We observed that the ETC of U88 was influenced by radiation even at low temperatures, a behaviour attributed to the effect of the incoming radiation on the sample.

We additionally observed that the ETC is also affected by the external radiation, i.e. the

boundary condition. Particularly, we compared the ETC of an uncoated 88 % porosity sample and that of a coated 88 % porosity sample (coated with a 200 to 400  $\mu\text{m}$  thick, dense layer that prevents radiation from penetrating the sample). The ETC of these samples showed differences between 28 to 46 %. We conclude that in the case of highly porous materials, the ETC is affected by the incoming radiation to which the sample is exposed if the source of heat flux is purely radiative. The ETC of a sample exposed to a heat flux approximately 8 times smaller than the reference case ( $1 \text{ MW m}^{-2}$ ) was evaluated to confirm this hypothesis. We indeed observed that there is a correlation between the incoming heat flux level and the ETC values, as the ETC of a sample decreases by 7 to 38 % with a lower peak heat flux ( $136 \text{ kW m}^{-2}$ ). This effect was less noticeable for samples with lower porosities (81 % and 75 %) as the pore diameters of these types of sample are small enough (230 and 190  $\mu\text{m}$ ), therefore limiting the effect of internal or incoming radiation.

The ETC of a uncoated pure alumina sample with 92 % porosity was not affected by the incoming radiation. The extinction coefficient of this specimen is about an order of magnitude higher than that of an 88 % porosity alumino-silicate sample. This highlights that the extinction coefficient and, hence, the morphology is an important characteristic to consider when quantifying the influence of incoming radiation on the ETC.

We conclude that the ETC depends not only on the material and its morphology but also on operating conditions, especially if the material is expected to have a rather low extinction coefficient and to be exposed to a pure radiative heat flux. Consequently, the evaluation of the ETC has to be done under realistic conditions or for a large range of conditions in order to provide general engineering relations and guidance.

The goal of this study was to present a new, simple method to determine the ETC, which requires one experiment only and can provide - in one go - the ETC in temperature range larger than 1000 K. Further investigations considering separate radiation and conduction are recommended to evaluate the ranges of conditions and material conductive and radiative properties for which an ETC approach is sufficient and those for which a more detailed, but therefore computationally more expensive method such as Monte-Carlo ray-tracing, are needed.

2222.6



# 5 Coupled conduction-radiation modeling of the thermal response of highly porous materials in radiative environment

This chapter presents results of coupled conduction-radiation simulations performed with the PATORAC algorithm presented in Section 3.4 that makes use of the MCRAD code detailed in Section 3.3.

The methodology is partially reminded and assumptions specific to this study are explained in the first part of this chapter. The second part shows a comparison between the results obtained with the ETC model and those with a coupled approach, highlighting the influence of incoming radiation and hence the need for coupled simulations in the case of a radiative flux boundary conditions on semi-transparent samples. The third part of this chapter shows the results of a sensitivity study on the porosity, bulk thermal conductivity and extinction coefficient of ceramic foams. This study leads to guidelines in the choice of the approach to model the thermal response of highly porous materials placed in a radiative environment.

## 5.1 Methodology complements

As a reminder, in the PATORAC algorithm, the equation of conservation of energy reads:

$$\partial_t(\rho e) = \nabla \cdot (\mathbf{k}_{\text{cond}} \cdot \nabla T) - \nabla \cdot \mathbf{q}_{\text{r,tot}} \quad (5.1)$$

where,  $\mathbf{k}_{\text{cond}}$  is the thermal conductivity accounting for conduction only, and  $\nabla \cdot \mathbf{q}_{\text{r,tot}}$  is the sum of divergence of radiative heat flux of the two phases, solid and air, modeled in the MCRAD code. This chapter uses the simplified version of Equation (3.30) because thermochemical processes do not occur in the studied ceramic foams. The simulations were all performed on a 40x40x20 mm computational domain, reproducing the size and shape of the samples studied in Chapter 4.

This chapter is based on the thermal properties of pure alumina. The density of alumina is

$3980 \text{ kg m}^{-3}$ . The heat capacity and thermal bulk conductivity extracted from Shackelford and Alexander<sup>(119)</sup> are shown in Figure 5.1.

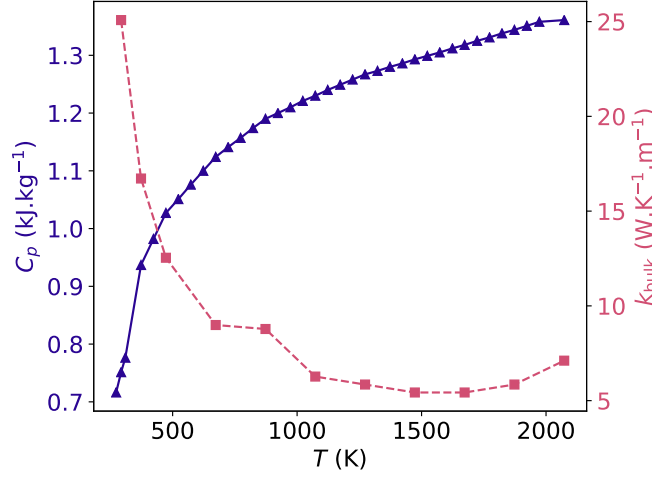


**Figure 5.1** – Bulk thermal conductivity and heat capacity of alumina

This chapter deals with pure alumina samples. Consequently, as discussed in Section 2.1.5, the emissivity in the IR wavelength range was assumed to be 0.95. The emissivity in the visible range, to be considered for incoming HFSS radiation (see Section 3.3), was equal to 0.25, as suggested by Touloukian<sup>(108)</sup> for 99 % pure alumina.

The effective thermal conductivities for the ETC model were obtained using the Kunii model, which was introduced in Section 4.3.4 and is reminded in Equation (5.2).

$$k_{\text{eff}} = \underbrace{C(1-\phi)k_b + k_a\phi^{1/3}}_{k_{\text{cond}}} + \underbrace{\left(\frac{2}{3}\right)10^{-6}(\alpha_r D_p)\phi^{1/3}}_{k_{\text{rad}}} \quad (5.2)$$

Equation (5.2) can be rewritten as:

$$k_{\text{eff}} = k_{\text{cond}} + k_{\text{rad}} \quad (5.3)$$

where  $k_{\text{rad}}$  is the radiative conductivity, taking into account radiative transfer in the ETC model.

Porous alumina samples were considered to be composed of two semi-transparent phases. Phase 1 corresponded to the solid phase of the ceramic foam, phase 2 to the gas phase. The effective radiative properties are given in Equations (5.4) to (5.7).

$$\beta_1 = \beta_2 = \frac{1}{D_p} \quad (5.4)$$

$$\kappa_1 = \beta_1 - 1.0 \text{ m}^{-1}, \sigma_{11} = 0.0 \text{ m}^{-1}, \sigma_{12} = 1.0 \text{ m}^{-1} \quad (5.5)$$

$$\kappa_2 = 1.0 \text{ m}^{-1}, \sigma_{21} = \beta_2 - 1.0 \text{ m}^{-1}, \sigma_{22} = 0.0 \text{ m}^{-1} \quad (5.6)$$

$$n_1 = n_2 = 1.0 \quad (5.7)$$

As a reminder, as opposed to pore-level MC radiation simulations, no phase was pre-determined in each mesh cell: the phase was selected in function of a random number compared to the porosity of the studied material. Therefore, the extinction coefficients of the two phases were assumed to be equal. The solid phase was assumed to be non-scattering ( $\sigma_{11} = \sigma_{12} = 0.0 \text{ m}^{-1}$ ). On the contrary, the gas phase was assumed to be purely scattering to phase 1 (refraction,  $\kappa_2 = 0.0 \text{ m}^{-1}$ ).  $\sigma_{12}$  and  $\kappa_2$  were taken equal to  $1.0 \text{ m}^{-1}$  in order to avoid code errors. The value of  $1.0 \text{ m}^{-1}$  is very small compared to the order of magnitude of extinction coefficient, which lowest value was  $256.0 \text{ m}^{-1}$ , making  $\sigma_{12}$  and  $\kappa_2$  about 0.25 % of  $\beta$ .

### 5.1.1 Initial and boundary conditions

At  $t = 0$ , the entire simulation domain was at ambient temperature. The considered solar radiation input flux on the exposed surface was assumed to be typical of solar concentrating facilities, such as solar dishes or solar simulator. The flux distribution, which corresponds to the steady-state regime of lamps 3 and 6 of the HFSS at 70 A (see Section 2.1), is shown in Figure 5.2. The peak flux was set to  $14495$  or  $2222.6 \text{ kW m}^{-2}$ .

Boundary conditions (BCs) on the external walls were different, whether the ETC approach or the PATORAC model were used. For the ETC and PATORAC models, the BC at the front face were defined as the absorbed radiative flux at the front face as:

$$q_{\text{abs}} = \varepsilon_{\text{vis}} q_{\text{inc}} \quad (5.8)$$

where the emissivity in the visible light range was set  $\varepsilon_{\text{vis}} = 0.25^{(108)}$ . For one alternative version of the PATORAC model front boundary, the front wall temperature distribution,  $T_{\text{wall},f}$ , was given, derived from the solution of the ETC model. The re-radiation at the front surface and lateral surfaces were given as:

$$q_{\text{rerad}} = \varepsilon_{\text{IR}} \sigma T_{\text{wall},f}^4 \quad (5.9)$$

where the emissivity in the IR range was set to  $\varepsilon_{\text{IR}} = 0.8^1$ ,  $\sigma$  is the Stefan-Boltzmann constant, and the subscript  $i$  identifies front, lateral or rear wall (subscripts f, l and r). Convective heat

<sup>1</sup>For an assumed considered temperature profile in the alumina samples of 300 - 2000 K, the corresponding wavelength according to Wien's displacement law is  $\lambda = 1.5 - 10 \mu\text{m}$ . Thus, the considered emissivity  $\varepsilon_{\text{IR}} = 0.8^{(108)}$ .

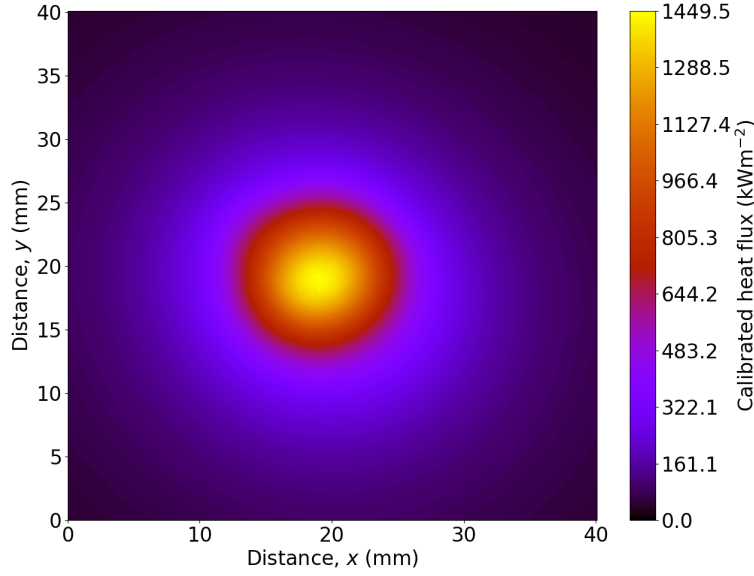


**Figure 5.2** – Radiative flux distribution on the 40x40 mm exposed surface for the study of radiation-conduction coupling.

losses from the front, lateral and rear walls were given as:

$$q_{\text{conv},i} = h_i(T_{\text{wall},i} - T_{\text{amb}}) \quad (5.10)$$

where  $T_{\text{amb}}$  is the ambient temperature,  $T_{\text{wall},i}$  and  $h_i$  are the temperature and the convective heat transfer coefficient, respectively, at face  $i$ .  $h_i$  is equal to 135.0, 20.0, 5.0  $\text{W m}^{-2} \text{K}^{-1}$  for front, lateral and rear faces respectively. BCs on internal walls were defined as fully diffusely reflecting with wall reflectivity of  $\rho_{\text{wall},i} = 1.0$ .

The BCs are schematically shown in Figure 5.3. For the ETC model, BCs type (a) were used, which are absorbed radiative flux on the front face as well as heat convection and re-radiation from all faces. For the PATORAC model, two types of BCs were tested. BCs type (b) considered the sample with non-transparent walls, thus BCs type (a) were applied for the external BCs whereas full and diffuse reflection for inner walls within the media was assumed. Alternatively, BCs type (c) were considering the lateral and rear walls as semi-transparent walls. Thus for these walls, no radiative BCs ( $q_{\text{terad}}$ ,  $q_{\text{refl}}$ ) were necessary, only the heat convection was considered.

These BCs were set in this way to make the simulation cases close to the real application in the HFSS, but they do not correspond to any rebuilding case. The goal of this chapter is to show the differences between the ETC and PATORAC methods, and hence to highlight the advantages and limitations of both approaches.



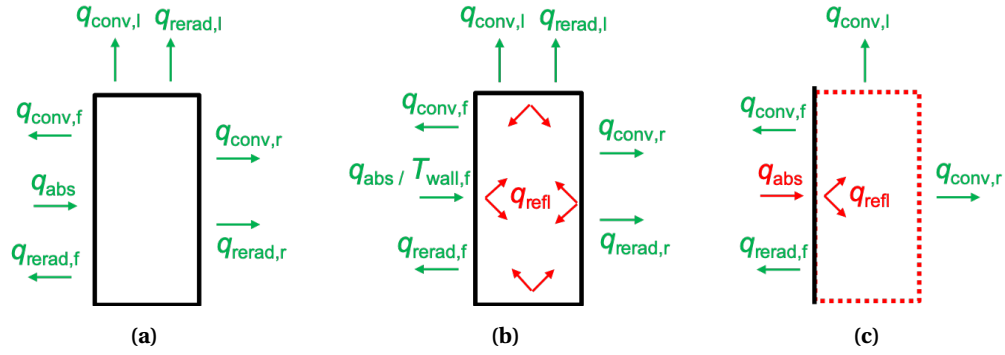


**Figure 5.3** – For the ETC model, BCs type (a) were used, which are absorbed radiative flux on the front face and heat convection and re-radiation from all faces. For the PATORAC model, BCs type (b) or (c) were considered. BCs type (b) considered the sample with non-transparent walls, thus BCs type (a) were applied for the external BCs plus full and diffuse reflection boundaries in the medium were assumed. BCs type (c) considered the lateral and rear walls as semi-transparent walls. Thus, no radiative BCs ( $q_{rerad}$ ,  $q_{refl}$ ) were necessary, only the heat convection was considered. For all types, BCs indicated in green were used in order to solve Equation (5.1) whereas BCs in red were applied to Equation (3.19).

## 5.2 Results and discussion

### 5.2.1 Comparison of ETC model to coupled model results

The goal of this section is to quantitatively show how the ETC and PATORAC model compare, considered that PATORAC is assumed to be physically more advanced. First, the difference between the ETC model and the PATORAC model, where only internal radiation is taken into account on the MC side (the incoming flux or surface temperature BC was applied on the PATO side), is highlighted. Then, the effect of incoming radiation taken into account on the MC side is described.

The influence of the bulk conductivity values was studied by varying its values, using a bulk conductivity factor, called bulk conductivity factor  $F_{k,bulk}$ . The  $R^2$  values is evaluated with the PATORAC as reference.

#### Internal radiation

Figures 5.4(a) and (b) show in purple the temperature results on the center line of the sample through its thickness obtained with the ETC model for a 95 % porosity sample, with a bulk conductivity factor of 0.125 and two extinction coefficients of 1024 and 16384  $m^{-1}$  respectively. The third case is shown in black plain lines in Figure 5.4 and corresponds to a case where the same flux BC as for the ETC model was applied on the PATO side. Pure conduction is considered in the energy equation and radiation is treated in the MC code.

The time-dependent surface temperature was extracted from the two ETC cases in order to apply it and evaluate the effect of internal radiation in the case of a transient Dirichlet boundary condition. The corresponding results are presented in dashed line in Figure 5.4. The goal is to suppress the differences due to the flux BC and study exclusively the differences due

to the way radiation is treated.

Figure 5.4 shows that the deviation between the ETC and PATORAC models for a flux BC applied on the PATO side is important even though the  $R^2$  value is 0.99. The reason is that the two temperature profiles through the thickness cross at a corresponding depth of 1 mm. The surface temperature is 7.1 % higher with the PATORAC model whereas the ETC model provides higher temperatures (maximum difference of 17.1 % at 9.3 mm) through the sample from 1 mm below the exposed surface. The difference between the ETC model and the PATORAC with a temperature BC is even more significant, with an  $R^2$  value of 0.88. In both cases, the relative temperature difference on the backface is also important (8.9 %).

The ETC takes into account radiative heat transfer through a radiative conductivity  $k_{\text{rad}}$ , which increases with  $T^3$ . The difference between the ETC ( $k_{\text{eff}}$ ) and  $k_{\text{cond}}$  explains the deviation between the two gradients, especially at high temperature. This shows that  $k_{\text{rad}}$  is overestimating the internal radiative heat transfer for the considered sample (95 % porosity,  $\beta = 1024 \text{ m}^{-1}$ ,  $F_{k,\text{bulk}} = 0.125$ ).

When  $\beta = 16384 \text{ m}^{-1}$ , the differences are significantly smaller, with  $R^2$  values over 0.99 for the two types of BCs with PATORAC. However, the maximum temperature differences are still 6.1 % and 5 % for the flux and temperature BC cases, respectively. This demonstrates that the ETC model still overestimates the internal radiative heat transfer in the case of a low bulk conductivity.

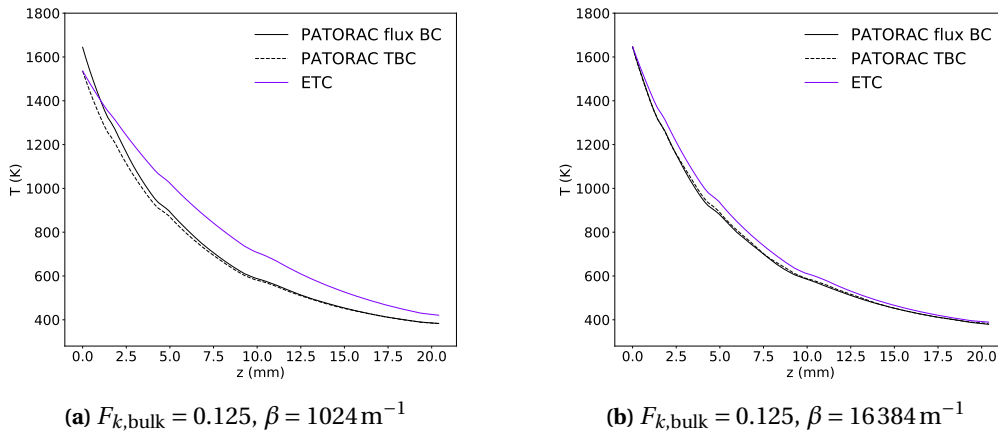


**Figure 5.4** – Comparison of results obtained with the ETC and the PATORAC model using flux and temperature BCs for a sample with a porosity of 95 % and a bulk conductivity factor  $F_{k,\text{bulk}}$  of 0.125. Two extinction coefficients, (a)  $\beta = 1024 \text{ m}^{-1}$  and (b)  $\beta = 16384 \text{ m}^{-1}$ , were used to evaluate the capability of the ETC to account for internal radiation in function of  $\beta$ .

Figure 5.5 shows a similar comparison as of the cases in Figure 5.4, where the bulk conductivity factor is 1.0, i.e. the sample considered is made of pure alumina. The temperature profiles in Figure 5.5(a) show globally the same behaviour as those in Figure 5.4(a), with much smaller deviations between the ETC and PATORAC models ( $R^2$  values of 0.995 and 0.988 for the flux and temperature BCs respectively). The surface temperature relative difference between the ETC and the flux BC PATORAC models is reduced to 5.0 %. The maximum relative differences

with the ETC model of 3.8 and 5.1 % occur at 6.3 and 2.8 mm for the flux and temperature BCs respectively. Figure 5.5(b) shows that the three plotted temperature profiles are almost identical when  $\beta = 16384 \text{ m}^{-1}$ , with  $R^2$  values higher than 0.999 and maximum relative temperature differences of 1.4 % and 0.9 % for the flux and temperature BC cases, respectively. Therefore in the case of higher bulk conductivity, the radiative part of the ETC is adapted to model the internal radiative heat transfer.

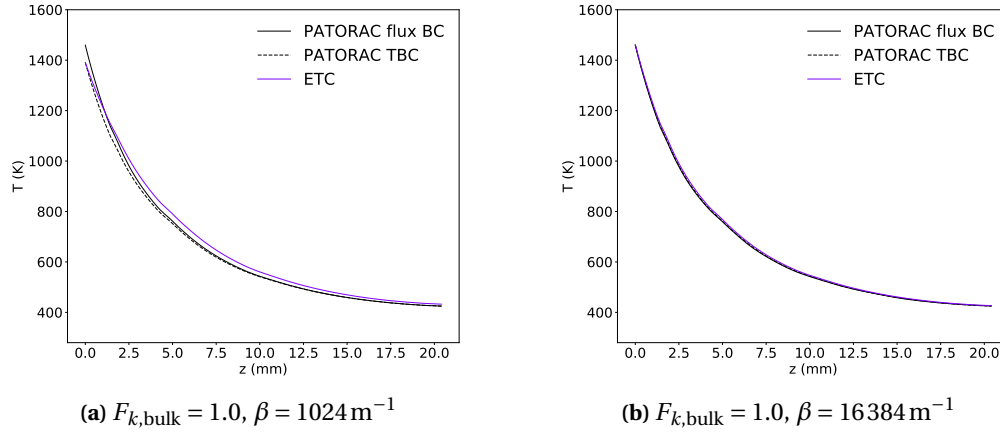


**Figure 5.5** – Comparison of results obtained with the ETC and the PATORAC model using flux and temperature BCs for a sample with a porosity of 95 % and a bulk conductivity factor  $F_{k,bulk}$  of 1.0. Two extinction coefficients, (a)  $\beta = 1024 \text{ m}^{-1}$  and (b)  $\beta = 16384 \text{ m}^{-1}$ , were used to evaluate the capability of the ETC to account for internal radiation in function of  $\beta$ .

First, these analyses show that internal radiation heat transfer is over-estimated by the radiative part of the ETC, as seen in Figure 5.4(a). This issue is less problematic when the heat transfer becomes conduction-driven in the case of a high bulk conductivity. At high extinction coefficients, the internal radiative heat transfer is less important, and negligible when conduction is dominating, which corresponds to a low radiative conductivity relatively to the bulk conductivity. This highlights that the capability of the ETC model to account for internal radiative heat transfer depends on the couple  $(k_b, \beta)$ .

### Incoming radiation

Figure 5.6 presents a comparison of results obtained with the ETC and PATORAC models, for a bulk conductivity factor of 0.125. The radiative flux BC was applied on the MC code side, meaning that the incoming radiation penetrated into the sample and contributed to the radiative heat transfer, which physically corresponds to a more realistic model of the studied phenomenon.

Figure 5.6(a) shows the results for  $\beta = 1024 \text{ m}^{-1}$ . The penetration of radiation produced a PATORAC temperature profile through the sample which is drastically different from what was obtained with the ETC model. The maximum temperature of 2119 K did not occur at the surface but at a depth of 1.2 mm, and corresponded to a maximum temperature relative difference of 27.5 % between the two models (the maximum temperature for the ETC model is at

the surface). The  $R^2$  value is 0.50, which indicates that the ETC models failed at modeling heat transfer through a sample with these characteristics ( $\phi = 95\%$ ,  $F_{k,bulk} = 0.125$ ,  $\beta = 1024 \text{ m}^{-1}$ ). The reasonable surface and back temperature relative differences of 8.2 % and 9.5 % induced a global temperature difference through the sample of 953 K compared to 1115 K for the ETC model (16.9 % difference). This means that this specific ETC model underestimates the overall effective conductive heat transfer through the sample, even though the gradients indicate that the effective conductive heat transfer is locally much smaller with the PATORAC model. Figure 5.6(b) presents the comparison for an extinction coefficient of  $16384 \text{ m}^{-1}$ . The maximum temperature occurred at 0.2 mm from the surface with the PATORAC model. The overall fitting of the ETC model is very good ( $R^2$  value of 0.994, 1.8 % difference of global temperature difference), which shows that the ETC model was a good alternative to the fully coupled model in the case of a high extinction coefficient, even though it slightly underestimated the maximum temperature difference (4.4 % relative difference with maximum temperature of ETC model).

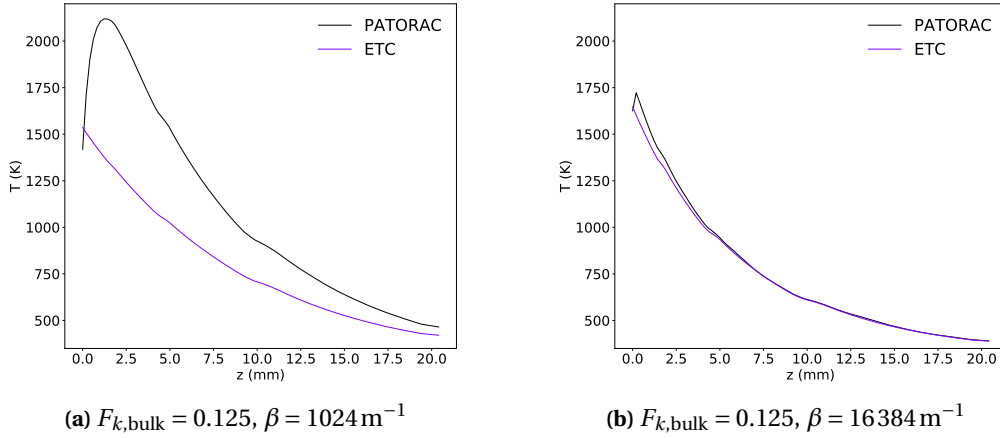


**Figure 5.6** – Comparison of results obtained with the ETC and the PATORAC model considering the radiative flux BC on the MC side for a sample with a porosity of 95 % and a bulk conductivity factor  $F_{k,bulk}$  of 0.125. Two extinction coefficients, (a)  $\beta = 1024 \text{ m}^{-1}$  and (b)  $\beta = 16384 \text{ m}^{-1}$ , were used to evaluate the influence of radiative transfer on the temperature profile in function  $\beta$ .

Similarly to what was observed in Figure 5.6(a), Figure 5.7(a) shows that the ETC model failed at predicting the thermal response of a material with an extinction coefficient  $\beta$  of  $1024 \text{ m}^{-1}$  and a bulk conductivity factor  $F_{k,bulk}$  of 1.0, although the deviation is less important ( $R^2 = 0.844$ ) when the bulk conductivity is higher. The maximum temperature relative difference was 15.1 % (1464 K at 0.8 mm for the PATORAC model, 1390 K at the surface for the ETC model). The relative error on the global temperature difference was almost identical with a higher conductivity (16.8 % for  $F_{k,bulk} = 1.0$  vs 16.9 % for  $F_{k,bulk} = 0.125$ ).

Figure 5.7(b) shows that the differences between the PATORAC and ETC models were minimal with high bulk conductivity factor and extinction coefficient ( $F_{k,bulk} = 1.0$  and  $\beta = 16384 \text{ m}^{-1}$ ), which was expected since this corresponds to a case very similar to that presented in Chapter 4 for sample U92. The maximum temperature appeared 0.2 mm below the surface with the

PATORAC model, leading to a maximum temperature relative difference of 1.0 % which was overestimated by the ETC model in this case. The  $R^2$  value of 0.998 confirmed that the ETC model is adapted to simulate the heat transfer in this type of sample.

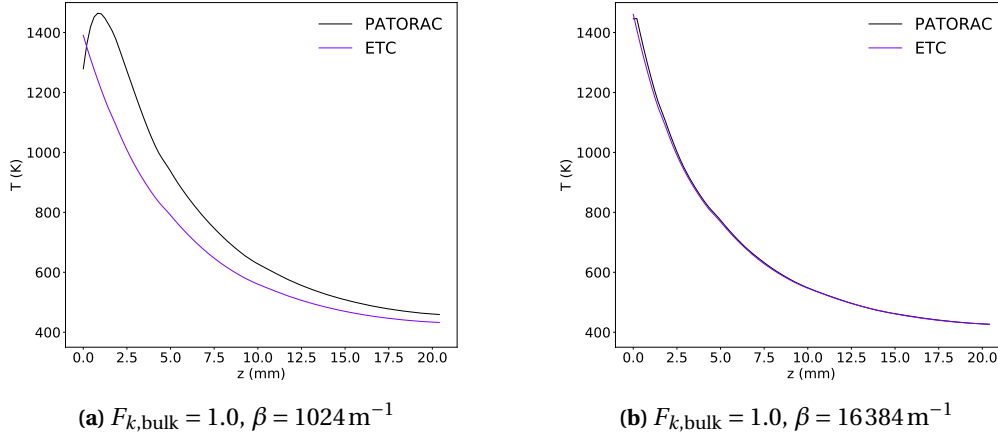


**Figure 5.7** – Comparison of results obtained with the ETC and the PATORAC model considering the radiative flux BC on the MC side for a sample with a porosity of 95 % and a bulk conductivity factor  $F_{k,bulk}$  of 1.0. Two extinction coefficients, (a)  $\beta = 1024 \text{ m}^{-1}$  and (b)  $\beta = 16384 \text{ m}^{-1}$ , were used to evaluate the influence of radiative transfer on the temperature profile in function  $\beta$ .

### Qualitative experimental comparison

Figure 5.8 shows a front and a cut view of an 85 % porosity sample, with pore sizes around 1 mm yielding an extinction coefficient of about  $1000 \text{ m}^{-1}$ . This sample was exposed to a heat flux high enough to cause degradation. The pictures highlight that the degraded region had a cavity shape, indicating that the degradation is more important below the surface. This is consistent with the PATORAC temperature profiles that are shown in Figures 5.6(a) and 5.7(a) where the maximum temperature occurred below the surface.

### Summary

This analysis has shown the way that the temperature profiles through the studied sample change in function of the bulk conductivity and extinction coefficient, in the presence of a radiative incoming heat flux. As the extinction coefficient decreases, the PATORAC temperature profile through the sample center line exhibits a behaviour that could never be reproduced by an ETC model. Due to the incoming radiative flux that penetrates the sample, the temperature increases from the exposed surface, reaches a maximum value before decreasing towards the back surface. It showed the importance of considering the radiative flux BC on the radiation side of the coupling algorithm. Nevertheless, the ETC model did not completely fail at simulating the overall temperature difference between the front and the back of the sample. For lower values of  $\beta$ , this overall temperature difference was overpredicted by the ETC model, indicating that the ETC is globally underestimated. However, it was clearly proved that in

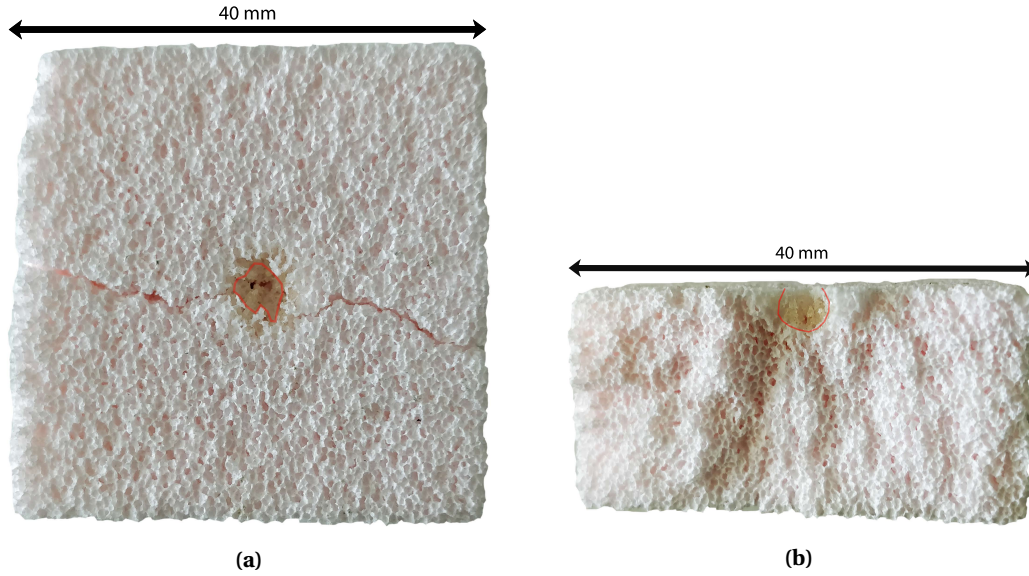


**Figure 5.8** – Pictures on a sample exposed in the HFSS to a high heat flux than induced the degradation of the sample. The flux relative distribution was identical to the one showed in Figure 5.2. (a) and (b) show respectively a front and a cut view of the degraded sample.

the case of a radiative incoming flux on a relatively low absorbing semi-transparent material the ETC model will not predict accurately the maximum temperature through the sample. Assuming that the iterative method described in Chapter 3 and used in Chapter 4 was to be applied to the PATORAC temperature profile obtained with  $F_{k,bulk} = 1.0$  and  $\beta = 16384 \text{ m}^{-1}$ , with thermocouple measurements at 3, 4, 5, 8 and 15 mm like it was done in Chapter 4, the ETC prediction would lead to acceptable values but would have missed completely the maximum temperature occurring inside the sample.

Figure 5.8 qualitatively confirmed the shape of temperature profiles obtained with the PATORAC model when the radiative flux BC was applied on the MC side.

### 5.2.2 Sensitivity study

It was shown in the previous section that the capability of the ETC model to accurately account for radiative heat transfer depends on the couple  $(k_b, \beta)$ . Therefore, in order to quantify the ranges for these two parameters within which the ETC model is adapted, a sensitivity study was performed. The bulk conductivity factor range was: 2.0, 1.0, 0.5, 0.25, 0.125, 0.0125. The porosity range that was considered goes from 75 % to 95 % with increments of 5 %.

Chapter 4 showed that the heat transfer through a 92 % porosity sample with an extinction coefficient of  $12500 \text{ m}^{-1}$  was driven mainly by conduction. The extinction coefficient values were therefore taken as: 16384, 8192, 4096, 2048, 1024, 512, 256  $\text{m}^{-1}$ . This range allowed to evaluate differences between regimes that are pure conduction driven and others where radiation has a strong influence.

The same geometry as in the previous section was used. The BCs were taken identical to

those described in the previous section for all the unexposed faces. For the exposed face BC, two magnitudes of radiative flux were studied to quantify potential differences induced by a change of flux. The first considered flux is the same as presented in Figure 5.2. The second flux was taken with the same relative distribution as the first one with a peak value of  $2222.6 \text{ kW m}^{-2}$ .

The bulk thermal conductivity and heat capacity of alumina (see Figure 5.1) were considered as a first step. A constant (temperature independent) conductivity of  $1.0 \text{ W m}^{-1} \text{ K}^{-1}$  was taken as a second step to assess the possible influence of the temperature dependence of the bulk thermal conductivity. In the latter case, a constant heat capacity of  $1.0 \text{ kJ kg}^{-1}$  was selected and the bulk conductivity factors were 100, 10, 1.0, 0.1, and 0.01.

The ETC and radiation-conduction coupled models were used to simulate the center line temperature profiles for all chosen cases. The deviations between the two models were evaluated with  $R^2$  values representing the goodness of fit of the PATORAC results by the ETC model. These values were reported to form one map for each porosity. The maps allowed to graphically quantify the ranges of suitability of the ETC model. White areas represent regions where no result could be obtained because of temperature reaching values outside the temperature range considered (273 to 2273 K). The red areas correspond to negative  $R^2$  values, which means that the fitting of the PATORAC results by the ETC model was worse than a horizontal line which constant value is the mean value of PATORAC temperature through the sample thickness.

### Temperature-dependent bulk conductivity and heat capacity

Figure 5.9 shows  $R^2$  values maps for all porosities and a peak value of incoming radiative heat flux of  $1449.5 \text{ kW m}^{-2}$ .

First, it can be seen in Figures 5.9(a) and (b) that there are  $(F_{k,\text{bulk}}, \beta)$  couples for which no data was available (crossed areas in the maps, due to too high temperatures). These region correspond to low  $F_{k,\text{bulk}}$  and  $\beta$  values. In fact, the lower the  $\beta$  the larger the radiation penetration. Moreover, the lower the thermal conductivity the higher the maximum temperature because the material transfers less heat and hence concentrates energy. This phenomenon was observed in the previous section (Section 5.2.1), where a higher conductivity material produced lower temperatures. The maximum temperature relative difference of 33 % occurred for  $\phi = 0.9$ ,  $\beta = 256$  and  $F_{k,\text{bulk}} = 0.0125$ , because no results were calculated for  $\phi = 0.9$ ,  $\beta = 256$  and  $F_{k,\text{bulk}} = 0.0125$  (white area).

It can be noticed that the red area decreased with the porosity. The conduction through the material increased with the solid proportion of the material. Therefore, similarly to the difference seen between Figures 5.6(a) and 5.7(a), the  $R^2$  value increased with the porosity for the same bulk conductivity and extinction coefficient.

The isolines tended to an vertical asymptotic behaviour for the lowest value of  $F_{k,\text{bulk}}$ , which means that they became independent of  $F_{k,\text{bulk}}$ . As detailed in Equation (5.3),  $k_{\text{cond}}$  was a combination of the bulk and air conductivity. At  $F_{k,\text{bulk}} = 0.0125$  the conductivity corresponding to the solid becomes negligible compared to the conductivity due to the air. For example,



## Chapter 5. Coupled conduction-radiation modeling

for a 95 % porosity sample,  $k_{\text{cond}}(1073 \text{ K}) = 0.0728 \text{ W m}^{-1} \text{ K}^{-1}$  of which  $0.07 \text{ W m}^{-1} \text{ K}^{-1}$  is due to conduction through air and  $0.0028 \text{ W m}^{-1} \text{ K}^{-1}$  through the solid.

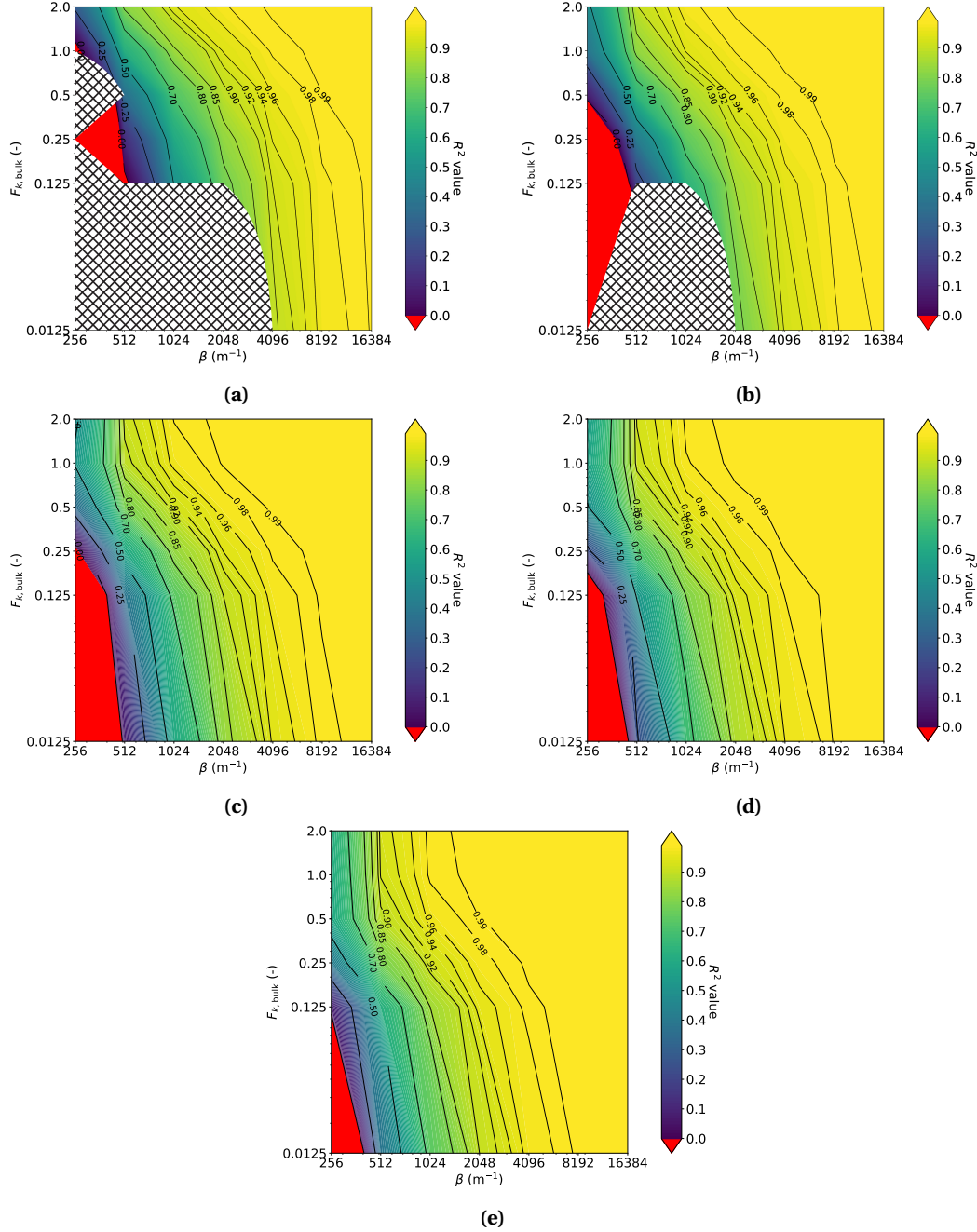


**Figure 5.9** – Maps of  $R^2$  values in function of the studied ranges of  $F_{k,\text{bulk}}$  and  $\beta$ , for porosities of (a) 95 %, (b) 90 %, (c) 85 %, (d) 80 %, and (e) 75 %. The peak value of incoming heat flux was  $1449.5 \text{ kW m}^{-2}$ .  $R^2$  values represent the deviations between the temperature profiles on the sample center line obtained with the ETC and PATORAC models. The red areas correspond to negative  $R^2$  values and crossed regions to cases where no results were obtained due to temperature values outside the material range.



### Temperature-independent conductivity and heat capacity

Figure 5.10 shows a comparison of results for an 85 % porosity sample obtained using temperature-dependent and independent thermal properties. The  $R^2$  maps were presented in function of extinction coefficient values and values of the porous material values average over the whole range of temperatures. The reported  $k_{\text{cond}}$  is averaged over the whole temperature range (only relevant for the temperature-dependent  $k_{\text{cond}}$ ). The two maps show very similar trends, especially the vertical asymptotical behavior for higher values of conductivities. Indeed, small differences between the ETC and PATORAC models created by incoming radiation is conserved because of the very high conductivity. This showed that the choice of the method to model heat transfer through porous media in the presence of a radiative heat flux environment does not depend on a potential temperature dependence of the bulk thermal properties of the material.

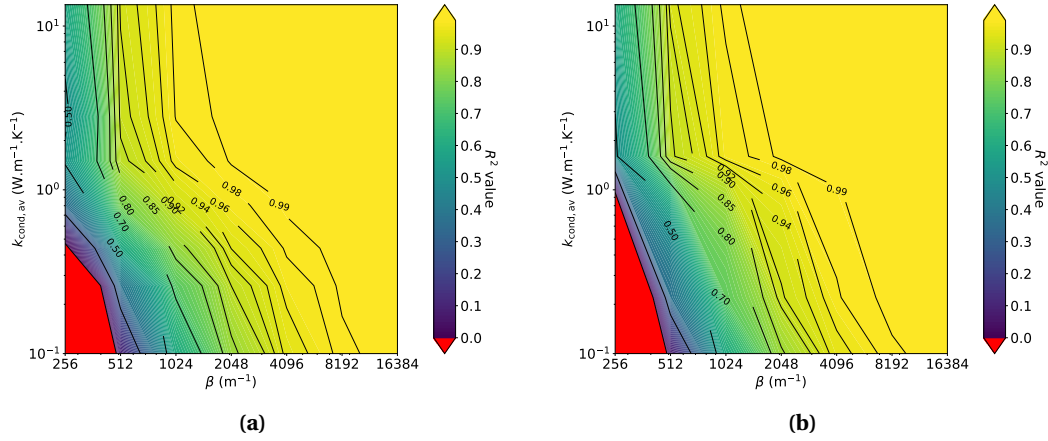


**Figure 5.10** – Comparison of  $R^2$  values maps between the (a) temperature dependent and (b) constant bulk conductivity cases for a porosity of 85 %. The peak value of incoming heat flux was  $1449.5 \text{ kW m}^{-2}$ . The red areas correspond to negative  $R^2$  values.

### Influence of incoming flux magnitude

Figure 5.11 shows a comparison of maps obtained for an 75 % porosity sample with the two levels of radiative flux considered in this section ( $1449.5$  and  $2222.6 \text{ kW m}^{-2}$ ). It can be seen that the isolines are very similar for bulk conductivity factors between  $0.125$  and  $2.0$ , indicating that the flux magnitude does not have much influence on the  $R^2$  values maps. However, the coefficient of determination  $R^2$  does not allow to evaluate the maximum temperature absolute difference between the ETC and PATORAC models, which might be the critical criterion for design purposes. Therefore the heat flux magnitude should still be taken into account for the choice of the approach to model heat transfer in such cases.

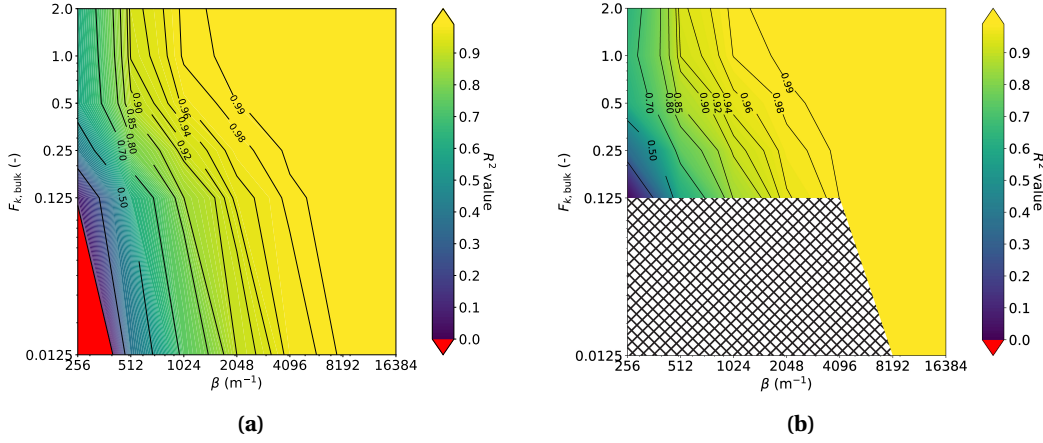


**Figure 5.11** – Comparison of  $R^2$  values maps between the (a) lower flux ( $1449.5 \text{ kWm}^{-2}$ ) and (b) higher flux ( $2222.6 \text{ kWm}^{-2}$ ) cases for a porosity of 75 %. The red areas correspond to negative  $R^2$  values and crossed regions to cases where no results were obtained due to temperature values outside the material range.

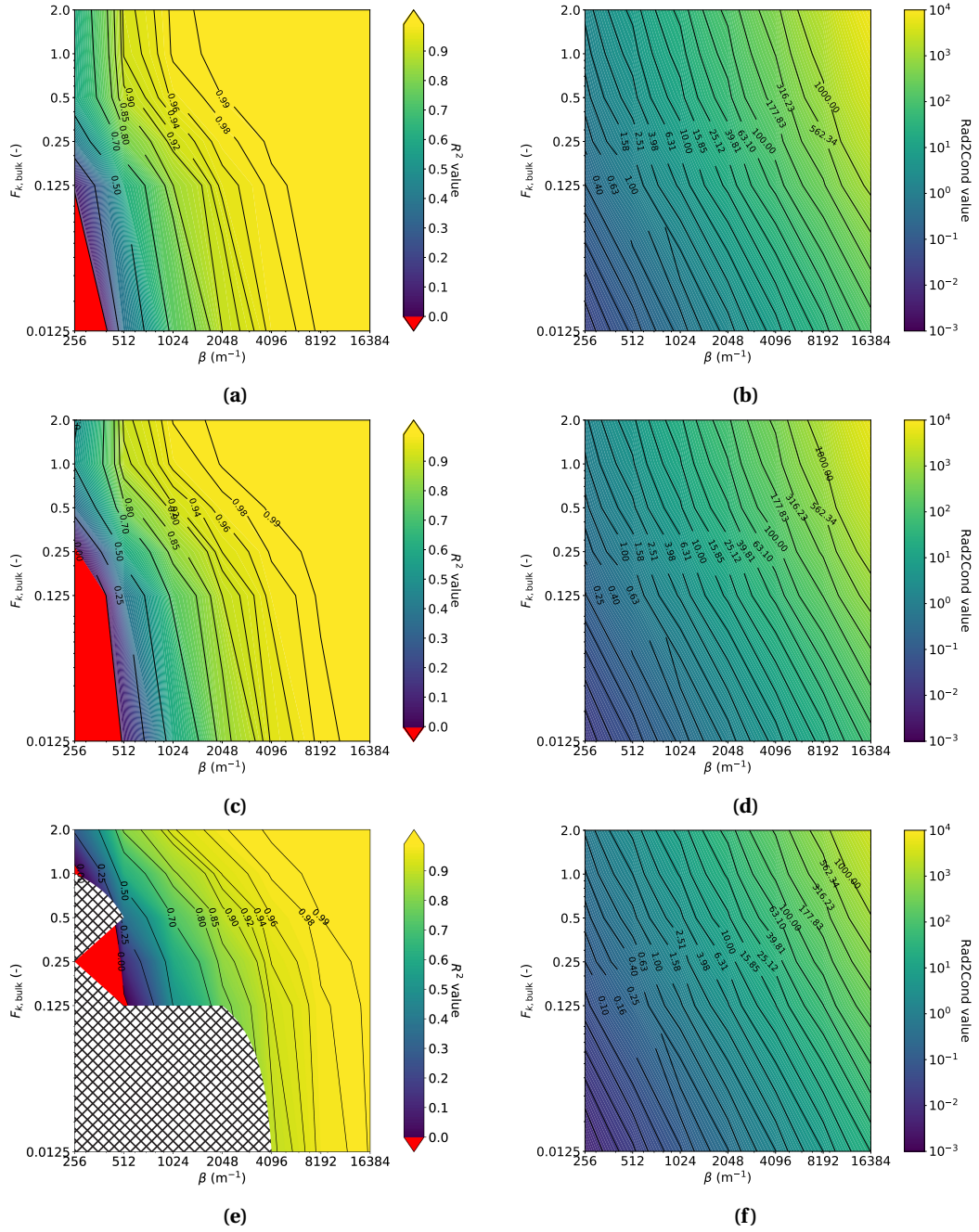
### Radiation-to-conduction number comparison

Figure 5.12 presents a comparison of the  $R^2$  value map for samples with 75, 85, and 95 % porosity obtained in the case of a flux peak value of  $1449.5 \text{ kWm}^{-2}$  to a map of a radiation-to-conduction dimensionless number. This number is noted  $Rad2Cond$  and is expressed in Equation (5.11).

$$Rad2Cond = \frac{k\beta^2 LT_w}{\dot{q}_{rad,inc}} \quad (5.11)$$

where  $T_w$  is the surface temperature given by the ETC model,  $L$  is the length of the sample, and  $\dot{q}_{rad,inc}$  is the incoming radiative flux peak value.  $\beta L$  represents the optical thickness of the considered sample.

The minimum  $R^2$  value to suggest choosing the ETC to model the heat transfer through these materials in the presence of a radiative flux environment is 0.98. The super-imposition of Figures 5.12(c) and (d) gives a value of 100 for the  $Rad2Cond$  dimensionless number, which is consistent with Figures 5.12(a) and (b) and Figures 5.12(e) and (f). For  $Rad2Cond > 100$  the ETC is adapted for the prediction of the temperature maximum value and profiles through the sample. However, this value decreases when the bulk conductivity becomes negligible compared to the air conductivity. For  $Rad2Cond < 100$ , the choice depends on what has to be predicted accurately. It has been shown in Section 5.2.1 that the ETC does not fail at predicting the surface temperature. The same applies for the global temperature variation or back face temperature. However, the ETC model produces significant relative errors on the predicted maximum temperature. Therefore, in the case of system design purposes where a material has to be chosen for its capacity to withstand a given range of flux, a fully coupled simulation would be preferred.



**Figure 5.12** – Comparison of (a), (c) and (e)  $R^2$  values map obtained for a sample porosity of 75, 85, and 95 % respectively and an incoming peak heat flux value of  $1449.5 \text{ W m}^{-2}$  to (b), (d) and (f) respective radiation-to-conduction factor values maps.

### 5.3 Conclusions

A coupled conduction-radiation model was developed to accurately study the heat transfer through porous materials which can be assumed to be composed of two semi-transparent phases (one pure absorbing and the other purely scattering), in the presence of incoming

radiative heat flux. The PATO toolbox was used to solve the conduction part of the model. A MC ray-tracing algorithm supporting the use of two volume-averaged phases was developed and implemented to simulate radiative heat transfer. The two codes were coupled via a python script which formed the PATORAC method.

This method was used to simulate the heat transfer through alumina sample with dimensions of 40x40x20 mm and to evaluate the performance of the ETC model used in the previous chapter to accurately predict heat transfer compared to the coupled model, taken as reference. The comparison between results was made using the coefficient  $R^2$  evaluated at the center line through the thickness of the sample. Maximum temperature and global temperature difference relative errors were also quantified.

The ETC was calculated using the modified Kunii model, as the results in Section 4.3.4 showed good agreement between retrieved values of ETC and the Kunii model. It was observed that the ETC model overestimated substantially the radiative conductivity when considering internal radiative transfer only. This difference decreased as the extinction coefficient increased, which is expected since the radiative conductivity was inversely proportional to the extinction coefficient. Moreover, the higher the bulk conductivity, the smaller the discrepancies between the ETC and fully coupled models, which was due to the radiative conductivity proportion of the ETC decreasing. On the contrary, for very low values of bulk conductivities, the conduction through the solid phase became negligible in front of the conduction through the air at atmospheric pressure. This made the deviations between the two models only extinction coefficient dependent.

The main differences between the temperature profiles obtained with the two approaches came from the penetration of the radiation through the sample when using the PATORAC model, leading to maximum temperatures occurring inside the sample instead of at the surface with the ETC method. The maximum temperature relative difference noticed was 33 %, which is critical for the design of such a material and for the numerical prediction of its thermal behaviour for a given application.

It was shown that for lower values of extinction coefficients the global temperature difference was overpredicted by the ETC model, which indicates that in the presence of radiation penetration, the ETC is globally underestimated by the Kunii model. This observation is only valid on a global point of view when looking at the front and back temperatures.

The temperature dependence of bulk thermal properties of the material did not prove to be very important for the evaluation of the capability of the ETC model to predict the thermal behaviour. The incoming flux magnitude did not change the  $R^2$  maps, suggesting that it had no influence on the results. Nevertheless,  $R^2$  values do not take into account absolute temperatures. Special care should be taken in the case of lower extinction coefficients.

Finally, a *Rad2Cond* factor was proposed to help in the choice of the approach to model heat transfer through this type of material. It was concluded that for  $Rad2Cond > 100$ , the ETC can be used in order to save substantial computational time. If  $Rad2Cond < 100$  and  $\beta < 1000 \text{ m}^{-1}$ , the ETC should not be utilized. If  $Rad2Cond < 100$  and  $1000 \text{ m}^{-1} < \beta < 8000 \text{ m}^{-1}$  the choice depends on what needs to be predicted. Errors produced by the ETC model on the surface temperatures are not too important (up to 15 %) and the ETC model can be acceptable.

However, the deviations on maximum absolute temperatures can reach 600 K and the ETC model is not recommended anymore. For  $\beta > 8000 \text{ m}^{-1}$ , the ETC model errors were generally acceptable.



## 6 Numerical rebuilding of ZURAM high-temperature tests in convective and radiative flux environment

This chapter first presents results and numerical rebuilding of tests on the ZURAM material performed in a convective flux environment, VKI's Plasmatron, which includes material analyses of tested sample providing data for charring degree numerical comparisons. Experimental and numerical results are also presented in the case of a HFSS tested ZURAM sample, in order to evaluate the testing viability of the HFSS for this type of material.

### 6.1 VKI Plasmatron tested ZURAM samples

This section focuses on two specific tests performed with ZURAM samples at two different flux levels in VKI plasmatron. Post-test material analyses are presented. Thermocouple measurements and charring degrees are compared to numerically rebuilt values using PATO, considering the effective thermal conductivity Section 3.1.

#### 6.1.1 ZURAM material

The ZURAM material is a composite made of carbon felts and phenolic resin. The phenolic resin is impregnated into a rigid carbon felt (CALCARB) and hot pressed. The final material is a lightweight ablative material designed for high-enthalpy space applications, with a density of 0.36 to 0.4 g cm<sup>-3</sup> (123).

#### 6.1.2 Experimental results

The testing conditions are given in Table 6.1.  $P_{el}$  is the electric power delivered to the inductive torch.  $\dot{q}_{cw}$  is the cold wall heat flux.  $p_s$  and  $p_d$  are the static and dynamic pressures respectively.  $T_w$  is the maximum wall temperature. The test corresponding to sample ZU1 is a relatively low flux condition (i.e. 0.3 MWm<sup>-2</sup>) that ran for a long time (i.e. 82 seconds) in order to trigger pyrolysis reactions through most of the sample, producing charred, partially pyrolysed and virgin layers through the sample thickness. The sample ZU3 was exposed to a high flux

## Chapter 6. Numerical rebuilding of ZURAM high temperature tests

condition (i.e.  $4.6 \text{ MWm}^{-2}$ ) for a short period of time (i.e. 10 seconds), inducing a very high surface temperature (2850 K) without letting heat propagate too deep inside the sample (only about xy mm).

**Table 6.1** – VKI Plasmatron test conditions for the two studied samples: ZU1 (low flux, long exposure time) and ZU3 (high flux, short exposure time)

Sample ID	$P_{el}$ kW	$\dot{q}_{cw}$ $\text{MWm}^{-2}$	$p_s$ hPa	$p_d$ Pa	$t$ s	$T_w$ K
ZU1	110	0.3	50	17	82	1510
ZU3	560	4.6	15	642	10	2850

Figure 6.1(a) shows a drawing of the test samples. They present a hemispherical nose with 25 mm radius and a cylindrical afterbody with 25 mm radius and 15 mm length. The sample holder hole of 14 mm in diameter was drilled from the back of the sample. The thermocouples positions for samples ZU1 and ZU3 are shown in Figure 6.1(b) and (c) respectively, and are summarised in Table 6.2. K-type thermocouples were used, with an uncertainty of  $\pm 0.75\%$  resulting in  $\pm 10^\circ \text{C}$  for the maximum measurable temperature. The axial distances are evaluated from the bottom of the sample, whereas the radial ones are given from the axis of symmetry. During the tests, the thermocouples were not arranged in the same plane from mounting reasons. However, the flux and temperature distribution exhibit an axisymmetrical pattern and the TCs will be assumed to be all part of the same plane for the numerical rebuilding of these tests.

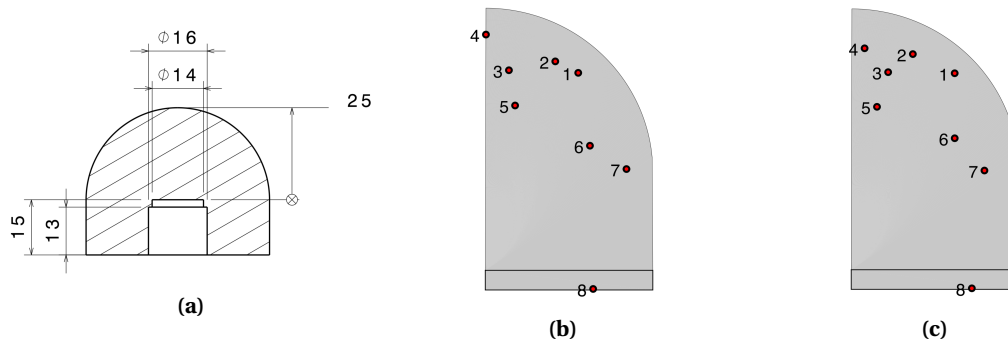


**Figure 6.1** – Drawing and schematics showing (a) the sample shape and dimensions, (b) and (c) the TCs positions reported to the same plane.

Figure 6.2(a) shows the stagnation point temperature for ZU1 and ZU3 samples recorded during VKI plasmatron tests using an IR camera coupled to a two-color pyrometer for in-band emissivity correction. The surface temperature of the ZU1 sample was recorded only during the heating phase because it was removed from its testing position, whereas that of the ZU3 sample was recorded for the whole duration of the test. The temperature distributions on the exposed surface at the end of the heating phase are presented in Figure 6.3 for the two



## 6.1. VKI Plasmatron tested ZURAM samples

**Table 6.2** – Probes/thermocouple positions for ZU1 and ZU3 cases: first row distance from sample bottom, second row distance from centre axis. All values are in mm

		TC1	TC2	TC3	TC4	TC5	TC6	TC7
ZU1	Axis	30.0	31.7	30.4	35.8	25.0	18.9	15.3
	Radial	14.0	10.6	3.7	0.3	4.6	15.8	21.2
ZU3	Axis	30.0	32.9	30.1	33.8	24.8	20.0	15.1
	Radial	15.6	9.3	5.7	2.1	4.0	15.6	20.0

samples. They exhibit axisymmetrical patterns for the two cases. The temperature on the hemispherical shape of the two samples (see Figure 6.2(b)) are almost constant relatively to the radial position, especially for ZU1 sample. The surface temperature of sample ZU1 slightly decreases towards the stagnation point (1521 K at the stagnation point vs 1564 K at 12.5 mm from the axis). The overall temperature difference is 543 K for ZU1 and 672 K for ZU3, which can be explained by the difference in flux level and the fact that ZU3 had not reached steady-state conditions after 10 s of test time, in opposition to ZU1 sample which reached steady state at around 40 s and surely after 82 s.

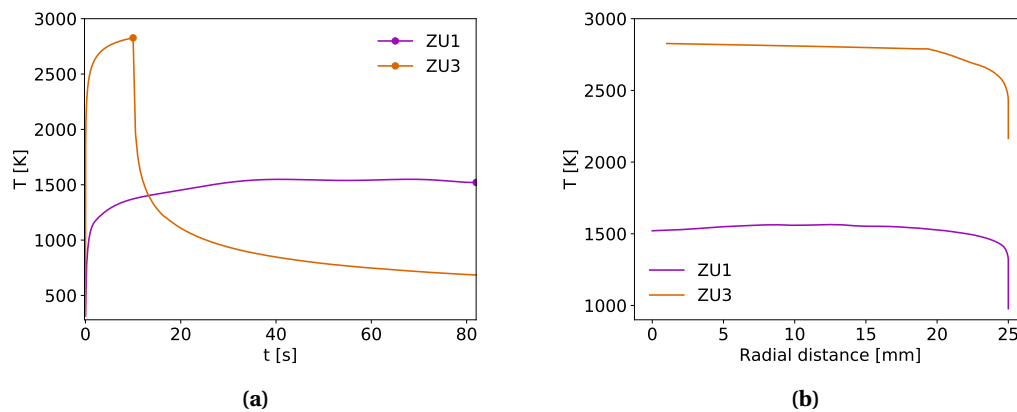


**Figure 6.2** – Temperature profiles (a) at stagnation points in function of time and (b) along the surfaces in function of the distance to central axis at the end of the heating phases for ZU1 and ZU3 cases. The dots in (a) identify the times when the temperature profiles represented in (b) were taken.

### 6.1.3 Material analyses

#### Measurement of charring degree of VKI tested samples using TGA

The purpose of TGA measurements was to quantify the charring degree of VKI tested samples. The first output would be the char thickness considering a threshold at which the material is completely decomposed. The second output is a charring degree profile through the tested sample on a specific line.

#### *Sample preparation*

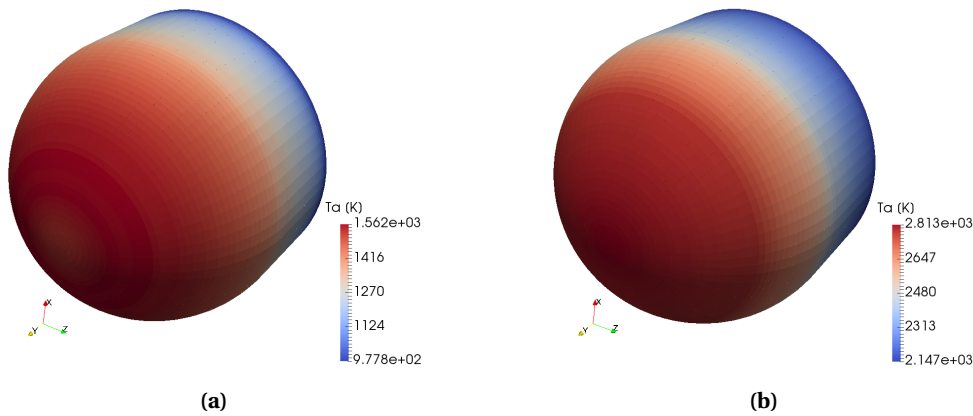


**Figure 6.3** – Surface temperature distributions for (a) ZU1 and (b) ZU3 cases recorded at the end of the heating phase (82 s for ZU1, 10 s for ZU1).

The two main requirements for doing TGA in the machine described in Section 2.3 were in terms of size and weight. The samples needed to fit in small cylindrical crucibles of approximately 6 mm in diameter and height. The minimum mass of a sample at the beginning of a test needs to be 3 mg, and the maximum is 15 mg.

The goal of the sample preparation for TGA testing was to prepare small samples representative of the region of interest. For virgin materials, a fragment taken off from the virgin is sufficient to represent the virgin material. For tested samples, a group of several samples representative of a radial line was cut off the cylindrical part of the models. A slice corresponding to such a line in which the group of samples was cut is shown in Figure 6.4(a). A total of 5 samples fulfilling the weight requirements (all 5 slightly more than 3 mg) were cut in this slice. This slice corresponds to the red line that is displayed in Figure 6.4(c). Locations A to E (see Figure 6.5) are positions taken from the surface towards inside the sample, which are spaced by 3 mm starting 1.5 mm below the surface. Material analyses were not done on sample ZU1 because it did not show a very changing char state profile through the thickness.

A razor blade for industrial use was utilized to cut these samples. As the samples did not have to have a specific shape, it was assumed that this technique was appropriate enough for this preparation. The use of gloves as shown in Figure 6.4(a) was mandatory too to avoid contamination of the samples.

### *Methodology*

The first phase of the test campaign was focused on the virgin materials in order to evaluate how fast the resin would decompose and therefore estimate the time needed to decompose all the resin contained in a sample. The resin content of a sample from the virgin material can be assumed to be the highest compared to samples coming from tested models. All tests were conducted with nitrogen as the test gas, to prevent the carbon fibres from oxydising. However, the oxidation of the fibers could not be prevented. A reason could be that there was a small opening on the lid of the TGA machine that allowed for oxygen diffusion and hence oxidation.

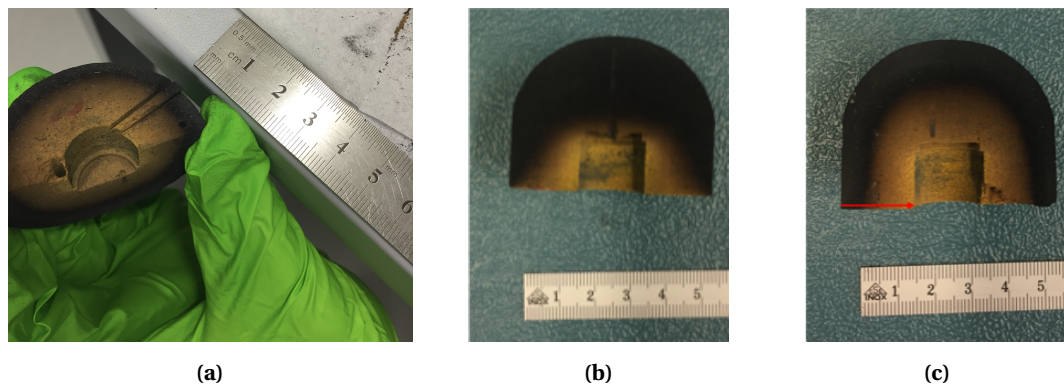


**Figure 6.4** – (a) Slice of sample to be cut into 6 pieces for TGA measurements. (b) Cut of sample ZU1 (c) Cut of sample ZU3 and cutting location for TGA measurements.

From now on, the normalised weight refers to the weight divided by the weight of the sample at a temperature of 100 °C in order not to account for the potential water content of samples due to humidity.

The temperature profile for these tests was as following:

1. Hold the temperature at 30°C for 1 minute.
2. Ramp the temperature from 30 to 900°C at a rate of 40°C/min.
3. Hold the temperature at 900°C for 180 minutes.

The heating rate was chosen high (40°C/min) in order to save some time, as the focus is not on defining precisely at which temperatures the reaction mechanisms are happening, but rather on defining how much resin is left in each sample. Figure 6.5 shows the TGA results for sample ZU3 in which the specimen A to E have been cut on the red line (see Figure 6.4). The curve corresponding to the virgin material in Figure 6.5(a) shows that there are two main reaction mechanisms happening, the first starting around 200°C and the second around 500°C. Figure 6.5(b) shows an initial transient phase for the virgin sample related to pyrolysis, followed after approximately 3000s by a linear decrease (with a slope of  $xy \text{ g/s}$ ) most likely due to the slow oxidation of fibres due to the impurity level of the technical nitrogen as well as the fact that the lid of the ceramic oven is pierced. Therefore, according to Figure 6.5(a), virgin Zuram contains approximately 28% of resin.

If there was no oxidation of the fibers, the resin content would have been evaluated according to the residual weight at the end of each TGA measurement. The presence of the slow oxidation of fibres that follow the pyrolysis make the detection of the end of pyrolysis difficult, even though Figure 6.5(a) shows that pyrolysis appears to be almost complete when the temperature reaches 900 °C.

For this reason the interpretation was made as following. Figure 6.5 shows the presence of

a dip (red box in normalised weight time derivative in subfig. (c)) just after the peak corresponding to pyrolysis. The bottom of the dip -that would correspond to a transition between pyrolysis and fibres oxidation- is considered as the end of the pyrolysis phenomenon. The time corresponding to this is then reported in Figure 6.5(b) to get the residual normalised weight at the end of pyrolysis. As a verification, this gives a resin content of 28.5% for the virgin material. Another dip can be seen for sample A (blue box) in Figure 6.5(c). This phenomenon happens only for the most charred sample, where the end of pyrolysis is then considered to be finished at the bottom of this trough.

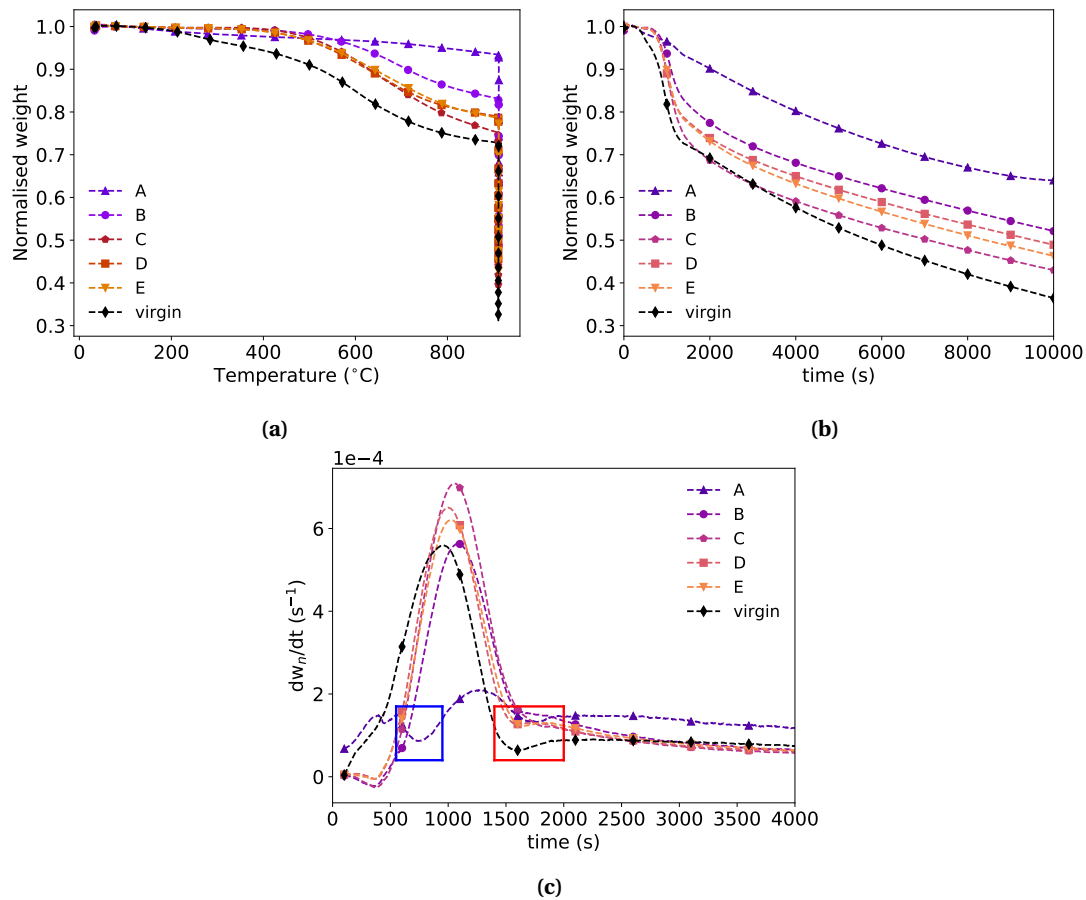


**Figure 6.5** – TGA results for ZU3 test sample showing the evolution of the normalised weight in function of (a) the temperature (the temperature rises from 30 to 900°C in 1500 seconds) and (b) the time. (c) gives the normalised weight time derivative in function of time. The letters A to E denote the five samples cut on the red line (see Figure 6.4), A being the closest to the exposed surface of the model and expected to be the most charred, E the deepest sample and hence the least charred. The samples are spaced by 3 mm. The red box correspond to a dip that identify the end of pyrolysis. The blue box identifies the end of pyrolysis for sample A.

Figure 6.6 displays the resin content (subfig. (a)), and the residual fibre content (subfig. (b)) for the 6 samples cut along the red line (see Figure 6.4) of sample ZU3. It can be observed that the profiles shown in Figure 6.6 do not behave as expected. Indeed, contents (resin or fibre) variations should be monotonical through the thickness of a sample. These small irregularities

are probably due to sample preparation differing from one sample to another. To evaluate the char layer thickness, a threshold of 10% of resin content is chosen. This is an arbitrary number and another value would lead to slightly different results in terms of char thickness, since char thickness is a discrete value. Values are interpolated between two data points given by the TGA. Therefore, the char layer thickness is approximately 2.7 mm for ZU3 test sample. However, the full residual weight profile are compared to numerical values of the charring degree profile in the next section.

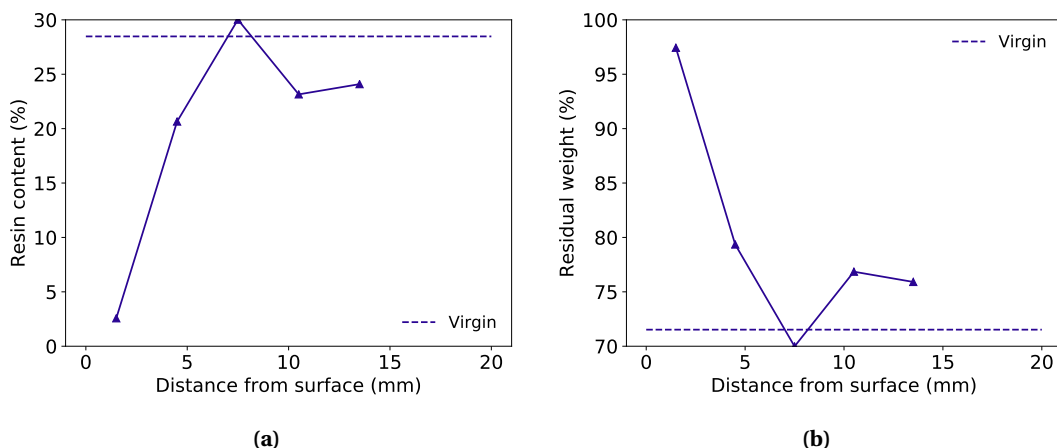


**Figure 6.6** – (a) Resin content and (b) residual weight through the thickness of sample corresponding to slice on the red line of sample ZU3.

### XPS measurement of charring degree of VKI tested samples

As explained in Chapter 2, X-Ray Photoelectron Spectroscopy (XPS) measurements were carried out using a PHI VersaProbe II scanning XPS microprobe (Physical Instruments AG, Germany). Analysis was performed using a monochromatic Al K $\alpha$  X-ray source of 24.8 W power with a beam size of 100  $\mu$ m. More details about the sample preparation can be found in the corresponding technical report<sup>(124)</sup>. Detailed spectra of the identified peaks (C1s, O1s, N1s, Si2p) were recorded on different locations of sample ZU3 corresponding to the red line in Figure 6.4(c). Atomic concentrations were determined by integrating the peak area of each element after a Shirley type background subtraction. A full compilation of the measured spectra is given in the corresponding technical report<sup>(124)</sup>. Only the main results relevant to the char layer are presented below.

#### *Virgin Zuram*

Carbon, Oxygen, Nitrogen and Silicon were identified in the spectra measured on the virgin Zuram sample. The C1s, O1s, N1s and Si2p peak areas were converted into atomic concentrations using the atomic sensitivity factors given by the proprietary PHI software. The atomic concentrations are listed in Table 6.3. The material was analysed in two spots to get an average value for the virgin material.

*Tested ZU3 sample*

The atomic concentrations at each position are listed in Table 6.3 and graphically represented as a function of distance from the surface in Figure 6.7.

Figure 6.7 shows that the exposition of the material in the plasmatron modifies its composition with respect to that of the virgin material. In particular, sample ZU3 is richer in carbon than the virgin one. When moving from the exposed surface to the center, the carbon content decreases from approximately 95% to values approaching 85%. The oxygen content increases correspondingly in the same direction. This effect is consistent with the expected preferential pyrolysis of the oxygen containing phenolic matrix. It can be observed that the composition measured on the exposed sample never reaches the values of the virgin material and always shows carbon enrichment. This indicates that the matrix undergoes degradation over the entire depth. This is consistent with the change in colour observed in the cross sections (Figure 6.4). Note, however, that XPS characterizes only the uppermost surface layer of the analysed material. It is thus possible that the observed deviation from the virgin material composition not only results from the loss of matrix mass but also from surface transformations (coking for example) of the matrix.

**Table 6.3** – XPS Atomic concentrations at different distances from the surface.

Material	Distance from surface (mm)	C1s (%)	N1s(%)	O1s(%)	Si2p(%)
Virgin #1	-	79.17	0.99	15.46	4.39
Virgin #2	-	79.52	1.07	14.82	4.59
ZU3 A	0.9	98.4	0.0	1.4	0.2
ZU3 B	3.5	97.2	0.0	2.4	0.4
ZU3 C	6.0	93.8	0.3	5.8	0.1
ZU3 D	8.8	91.9	0.0	8.1	0.0
ZU3 E	12.6	88.6	0.3	10.8	0.3
ZU3 F	14.4	87.4	1.1	11.1	0.3

**SEM measurement of charring degree of VKI tested samples**

The resin contained in the tested sample charges under the electron beam created by the SEM, whereas the carbon fibers, which are electrically conducting, do not charge. Charged regions can be identified as the brighter parts of an SEM image.

A Zeiss GEMINI 300 SEM has been used to detect the char thickness. The analysis was performed on sample ZU3 at low magnification (x50), at an accelerating voltage of 10 kV, and without coating to be able to observe charging of the resin rich parts. Figure 6.8 presents a

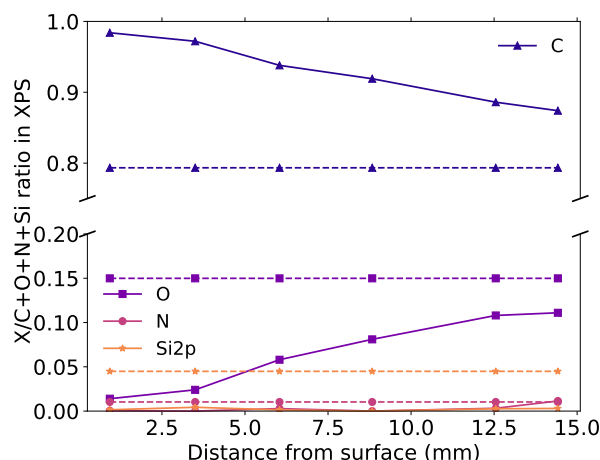


**Figure 6.7** – Atomic concentration ratio in function of the distance from the surface of the model on the red line (see Figure 6.4). The dashed lines correspond to virgin values.

mosaic of images recorded through the thickness of sample ZU3 on the red line (see Figure 6.4) that allowed to measure a char thickness of 5.055 mm. This distance was identified as the region where no charging occurs, highlighted by a yellow scale in Figure 6.8.

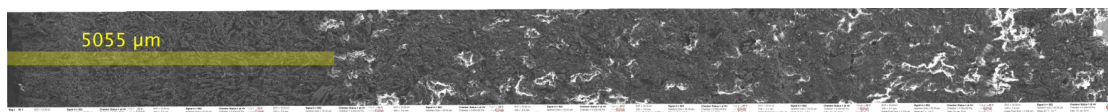


**Figure 6.8** – SEM images at low magnification (x50) of ZU3 sample along the sample depth on the red line defined in Figure 6.4. The sample surface is at on the left of the picture. The region highlighted by the yellow scale corresponds to the char layer.

### Char thickness comparisons

In order to compare the three measurement techniques, the char layer thickness is taken into account. It corresponds to the thickness through which the sample is considered to be fully charred. SEM measurements give exactly this value. For TGA analyses, it was assumed that the char layer thickness is determined by a threshold of 10% of resin content. The values were linearly interpolated between two measurement points to evaluate the position of this threshold. For the XPS technique, a discontinuity in the data would correspond to the char layer thickness, given the spatial resolution of the measurements presented previously.

Figure 6.9 shows a comparison of TGA, XPS, and SEM analyses. The plot shows that the position of the discontinuity for XPS is comparable to the position where the threshold of 10% of resin content is reached, given the fact that the best resolution for the distance from the surface that should be considered for TGA measurements is  $\pm 1$  mm. Indeed, the discontinuity for ZU3 sample can be noticed at 3.5 mm with XPS and for a char layer thickness of 2.7 mm with TGA. Nevertheless, with a threshold of 15 % of resin, the char layer thickness value can be

estimated to 3.5 mm. Therefore, the char layer thickness obtained with XPS falls into the error margin induced by TGA measurements. SEM images gave a char thickness of 5.1 mm, which is almost twice higher than the value found with TGA. One reason could be that potentially no charring could be seen on SEM pictures for a resin content. In that case, the threshold chosen for TGA measurement could be increased to 20 % and the values would match. Another reason is that SEM is a superficial technique, and the images might not be representative of the whole sample volume at a given depth. The summary of char layer thicknesses obtained with the three techniques is given in Table 6.4.

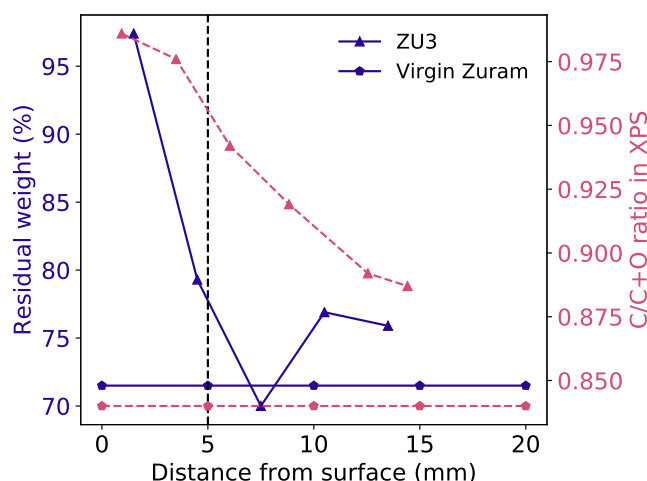


**Figure 6.9** – Comparison of the TGA residual weight (in blue) and the XPS C/C+O (in light red) profiles through the thickness of sample ZU3 on the red line. The vertical black dashed line corresponds to the char thickness determined with SEM.

**Table 6.4** – Char layer thicknesses (in mm) in the red line of sample ZU3 according to each method.

	SEM	TGA	XPS
Zuram 3	5.0	2.7	3.5

### Comments on material analyses techniques for the measurement of charring degree

The main advantage of TGA is that it evaluates directly the mass/volume resin content instead of a superficial quantification. The results obtained with this methodology are consistent with what is expected from the visual aspect of the tested sample (see Figure 6.4). They are also correlated to results given by SEM and XPS. XPS is a very efficient technique for material surface elemental composition evaluation. However, this method has one main disadvantage for the current application: the measurement is made only at the surface (first atomic layers) and does not necessarily reflect the volume and the mass of each of the components. In fact, in this application, it measures a projection of the surface of carbon fibres covered and uncovered by resin. Also, it can measure the elemental composition, so if the chemical



composition of the resin changes when decomposing during the pyrolysis phenomenon, the comparison of results between two regions that have a different advancement of reaction might be biased. Consequently, so is the comparison with TGA results. Nevertheless, XPS allows to perform a scan of a full surface instead of lines in a short time, which would give an even better set of data to be compared with numerical simulations. Finally, SEM is an efficient technique to assess the char thickness of tested Zuram samples. Indeed, Zuram is rather dense and the limit of the charred area is well defined (see Figure 6.8) when using standard SEM conditions. Like XPS analysis, this technique remains superficial.

As TGA provides a volumetric measurement of the charring degree, the TGA dataset is compared to numerical results.

### 6.1.4 Numerical rebuilding of experiments

#### ZURAM input data

ZURAM material data was extracted from a technical report by Turchi et al. <sup>(125)</sup> and is summarised in Tables 6.5 and 6.6 and Figures 6.10 (a) and (b). The material is considered orthotropic. Given the main axis of heat transfer through the specimen, "through-plane" corresponds to the direction of that main axis, and "in-plane" refers the other two directions, that are orthogonal to the main direction.

The resin contained in ZURAM decomposes as the temperature rises, following an Arrhenius' law given in Equation (6.1). The decomposition of the resin is described by three reactions occurring simultaneously but triggering at different energy levels. The parameters for these three reactions are given in Table 6.6.

$$\frac{\partial \xi_i}{\partial t} = (1 - \xi_i)^{n_i} A_i \left( \exp \frac{-E_i}{\mathcal{R}T} \right) \quad (6.1)$$

$\xi_i$  is the advancement of pyrolysis reaction  $i$ ,  $A_i$  is the Arrhenius law pre-exponential factor,  $E_i$  is the activation energy of reaction  $i$ ,  $\mathcal{R}$  is the universal gas constant and  $n_i$  is an extra Arrhenius' law parameter. The material properties (e.g. density) are calculated using a weighted average of virgin and char material properties. Equation (6.1) allows to calculate the gas production term,  $\Pi$ , due to resin decomposition and is therefore linked to Equation (3.1) (mass conservation) by Equation (6.2).

$$\Pi = f_{v,mv} \rho_{mv} \sum_{i=1}^{N_p} F_i \partial_t (\xi_i) \quad (6.2)$$

where  $f_{v,mv}$  and  $\rho_{mv}$  are the virgin polymer matrix volume fraction and density,  $N_p$  the number of pyrolysis reactions describing resin decomposition ( $N_p = 3$ ) and  $F_i$  the mass loss fraction due to pyrolysis reaction  $i$ . The equation for conservation of momentum (Equation (3.2)) is also directly affected by the gas production term as it uses the solution of the conservation of

mass.

The gas production term can also be seen as the density change of the matrix due to pyrolysis, which can be written as:

$$\partial_t (f_{v,m} \rho_m) = -\Pi \quad (6.3)$$

where  $f_{v,m}$  and  $\rho_m$  are the pyrolyzing matrix volume fraction and density. Moreover, the term  $\partial_t(\rho_p e_p)$  can be decomposed into:

$$\partial_t (\rho_p e_p) = \partial_t (f_{v,g} \rho_g e_g) + \partial_t (f_{v,m} \rho_m h_m) + \partial_t (f_{v,f} \rho_f h_f) \quad (6.4)$$

where  $f_{v,g}$ ,  $f_{v,m}$  and  $f_{v,f}$  are the volume fractions of gas, matrix and fibers phases,  $\rho_g$ ,  $\rho_m$  and  $\rho_f$  are the gas, matrix and fibers phases densities,  $e_g$  is the specific energy of the gas phase,  $h_m$  and  $h_f$  are the specific enthalpy of matrix and fibers phases. The production term  $\Pi$  therefore allows to calculate the contribution to Equation (3.3) (energy conservation) of internal energy change rate due to matrix pyrolysis.

Nevertheless, it is intrinsically impossible to determine experimentally virgin properties for all temperatures. The "virgin" properties shown in Figures 6.10 (a) and (b) correspond to a decomposing material with changing temperature. Consequently, for the heating up periods of the two test cases, the decomposing (virgin) material properties are used for both phases, to simulate the equivalent of one decomposing material. For the cool-down period, the material properties are switched to char properties for both phases again. As for the pyrolysis gas mixture physico-chemical data, the database `tacotair` available in the `MUTATION++` database was used. `MULTICOMPONENT THERMODYNAMIC AND TRANSPORT PROPERTIES FOR PARTIALLY IONIZED GASES IN C++ (MUTATION++)` is an open-source library developed at the von Karman Institute for Fluid Dynamics, designed to couple with conventional CFD or material response codes to provide thermodynamic, transport, chemistry, and energy transfer properties<sup>(126)</sup>.

**Table 6.5** – Summary of the ZURAM material input data to run PATO cases.

Variable	virgin state	charred state
Porosity [-]	5.56E-01	7.08E-01
Intrinsic density [g cm <sup>-3</sup> ]	7.48E+02	8.99E+02
Tortuosity [-]	1.2	1.1
Permeability [m <sup>-2</sup> ]	2.31E-013	5.95E-013
Emissivity [-]	0.8	0.9

**Table 6.6** – Pyrolysis reaction data for ZURAM

Reaction $i$	$F_i$	$A_i$ [SI]	$E_i / \mathcal{R}$ [K]	$n_i$ [-]
1	6.020E-02	6.667E+04	8.58E+03	5
2	4.988E-02	8.256E+05	1.33E+04	2.9
3	2.528E-01	9.499E+03	1.20E+04	2.2

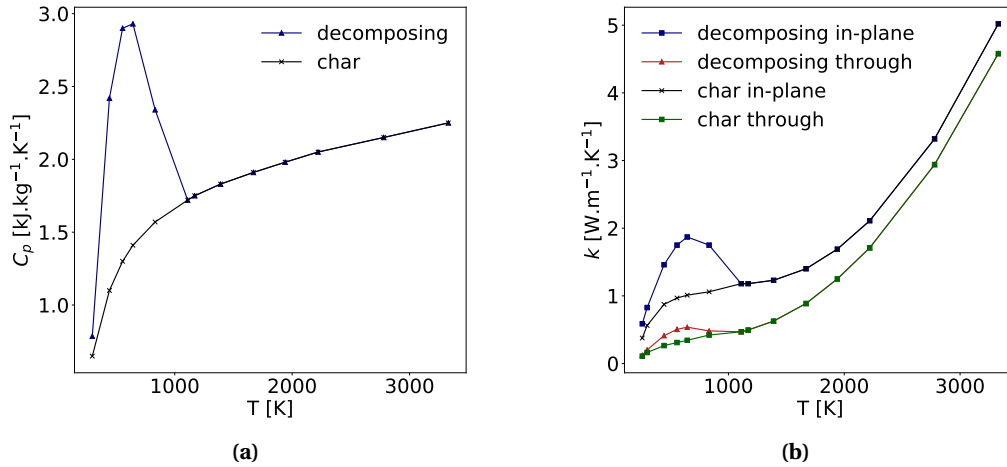


**Figure 6.10** – ZURAM material thermal properties. (a) Specific heat capacity for virgin and char states. (b) Effective thermal conductivity for virgin and char states. The conductivity being considered orthotropic, values are given "in-plane" and "through-plane"

### Domain geometry

The computational domain and mesh were built according to the geometry described in Figure 6.1.

As explained in Section 6.1.2 the test conditions are assumed to be fully axisymmetrical and the probes where temperature will be extracted are all positioned in the same plane, according to the distances from the centre axis and bottom of the sample, given in Table 6.2. Figure 6.11 shows the wedge geometry and the mesh created for rebuilding simulations.

### Boundary conditions

An adiabatic boundary condition was set on the bottom of the sample -in blue in Figure 6.11(a)- and inside the hole where the graphite holder is inserted -in orange in Figure 6.11(a)-. A simple symmetry condition is set on the axis of symmetry -in green in Figure 6.11(a)-. On the front and back patches, wedge boundary conditions are applied, corresponding to a cyclic condition between these two patches, except that it is applied to a 2D geometry. The BC that is applied on the exposed surface -in red in Figure 6.11(a)- is a set temperature (Dirichlet BC). This temperature is time-dependent and corresponds to the temperature extracted from IR images recorded during tests in the plasmatron as described in Section 6.1.2.

The `timeVaryingMappedTemperatureRadiationConvection` described in Section 3.1 was used to apply this temperature BC.

The pressure was set on the exposed surface equal to the total pressure, which is the sum of the static and dynamic pressures given in Table 6.1.

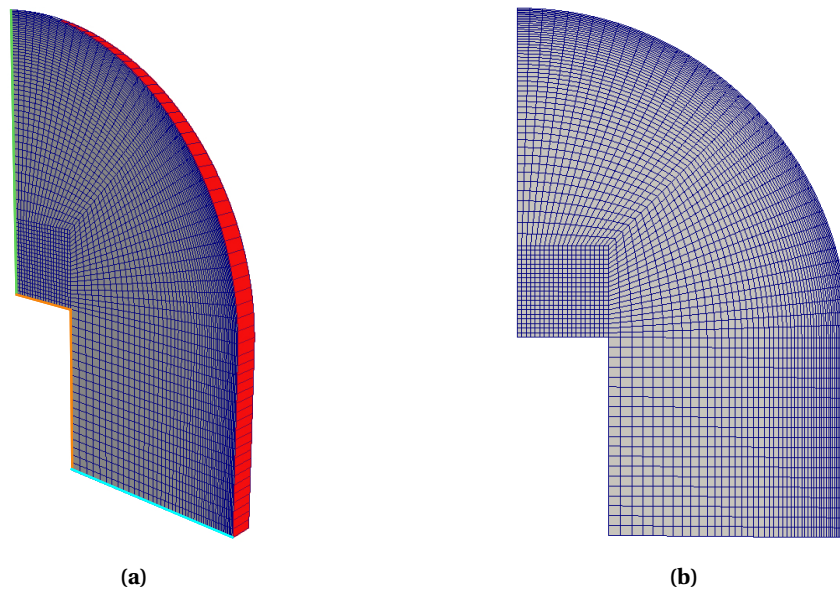


**Figure 6.11** – Geometry and mesh of the test sample. (a) View of the wedge used for 2D-axisymmetrical simulations. The blue, orange and green lines correspond to the bottom of the sample, the hole where for the sample holder and the symmetry axis respectively. The red surface represents the exposed surface. (b) View of the mesh with a refinement close to the surface of the test sample.

### Choice of model for numerical rebuilding

Given the pressure at which these tests were performed, there was no radiative flux coming into play. The thermal conductivity is relatively high, and effective extinction coefficients for this type of material are above  $30\,000\text{ m}^{-1}$  as shown by Banerji<sup>(127)</sup>. This is confirmed by White<sup>(97)</sup>, whose preliminary evaluation showed that such a material acts as a surface absorber. The ETC model is therefore used to rebuild those experiments.

### TC results

#### *ZU1 sample: database conductivity*

Figure 6.12 shows the results obtained for the simulation of ZU1 case using the material properties presented previously. It can be noticed that temperatures were overestimated by the simulation for all thermocouples (TC), especially for the lower temperature ones 5 to 7. Indeed, the temperature levels at 82 seconds, which corresponds to the end of heating phase, were over-predicted by 10.7, 12.1, 14.7, and 8.1 % for probes 1 to 4 respectively, whereas the simulation over-evaluated these by 29.4, 23.8, and 21.1 % for TCs 5, 6, and 7 respectively. The differences between numerical and experimental slopes indicate that the thermal diffusivity is too high when using the present model. The cooling down phase tends to confirm that the thermal diffusivity is too high. The values for TCs 1 to 4 look fairly close to experimental data, meaning that numerical values catch up to numerical ones very quickly. The temperature also tends to become uniform over the sample, which points out that heat transfer is fast and

confirms that the thermal diffusivity is too high compared to the experimental behaviour of the sample.

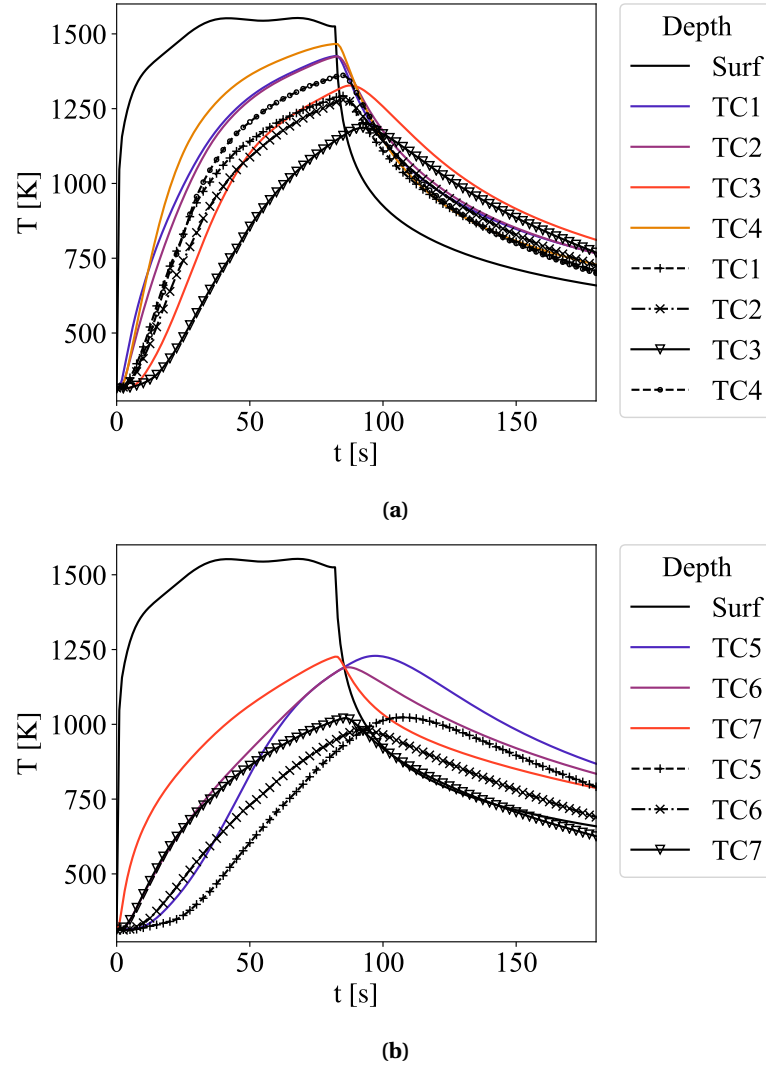


**Figure 6.12** – Comparison of thermocouple measurements in ZU1 sample (lines with symbols) to numerical temperature profiles (solid lines) at the corresponding depths, using the database thermal conductivity. (a) shows thermocouples at locations 1 to 4 (as per Figure 6.1(b)) and (b) shows thermocouples at locations 5 to 7 (as per Figure 6.1(b)).

#### *ZU1 sample: reduced conductivity*

The thermal diffusivity was therefore reduced by decreasing the effective thermal conductivity. Figure 6.13 shows results obtained by multiplying the conductivity by a factor of 0.55. This value was the one allowing to get the best fitting numerical results.

It can be seen in Figure 6.13(a) that the fitting of numerical values to experimental data for TCs 1 to 4 is much better, especially for the 3 TCs closer to the exposed surface (TC 1, 2, and 4), and almost perfect for TC4. Indeed, the relative differences at 82 s of test time are brought down to 0.9, 0.6, 5.6, and 0.1 % for TCs 1, 2, 3, and 4 respectively.

The results shown in Figure 6.13(b) show that the improvement of results is not as good for TCs 5 and 7. TC 7 indicates that the thermal conductivity is still too high, whereas TC 5 would tell the opposite. Numerical data for TC 6 fits well the experiment during the heating up phase, with a relative difference of 2.4 % at 82 s, but the cooling down phase is not significantly improved. One suggestion would be to further investigate separately thermal conductivity values in the two orthogonal directions. The slight change of slope for TC 5 and 6 when the cool-down starts is coming from the change of properties for both phases from decomposing to charred material properties at this time. It reveals that the material is not completely decomposed at the position of these TCs.

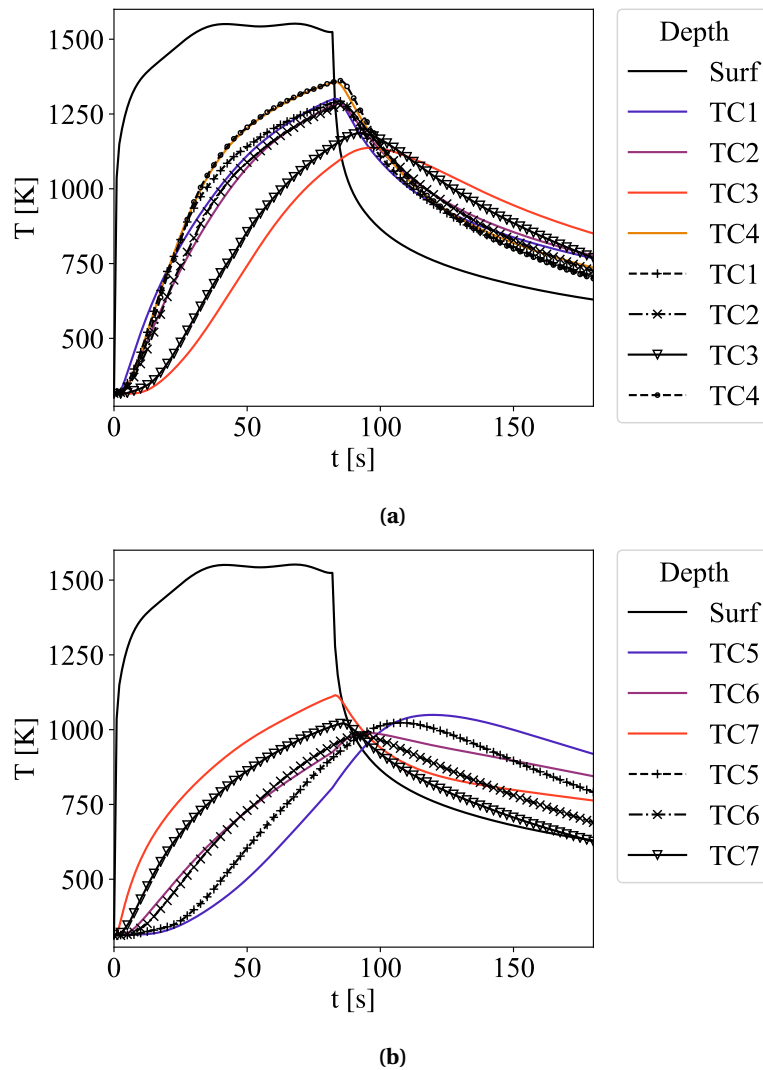


**Figure 6.13** – Comparison of thermocouple measurements in ZU1 sample (lines with symbols) to numerical temperature profiles (solid lines) at the corresponding depths, using the database thermal conductivity multiplied by a factor of 0.55. (a) shows thermocouples at locations 1 to 4 (as per Figure 6.1(b)) and (b) shows thermocouples at locations 5 to 7 (as per Figure 6.1(b)).

*ZU3 sample: database conductivity*

Figure 6.14 shows the results obtained using the conductivity from the database. It can be noticed that no comparison for TC 4 can be made since the experimental measurement has failed because the thermocouple was not well placed at the bottom of its hole.

Very similarly to ZU1 case, Figure 6.14(a) shows that the temperature for probes 1 to 3 is highly overestimated by the simulation, denoting a high value of the thermal diffusivity. The relative difference at 10 s is 62.1, 80.8, and 33.7 % for TCs 1, 2, and 3 respectively. However, the relative difference between numerical and experimental values for TC3 has not reached its maximum at 10 seconds, because of the short duration of the test compared to the inertia of the system. A maximum value of 81.6 % is reached at a time of 14 s. The temperatures are also over-predicted by the simulation for TCs 5 and 6 (see Figure 6.14(b), maximum relative differences of 27.7 and 63.7 % at 13 and 24 s respectively), whereas the fitting for TC 7 looks decent. However, it can be seen at the very beginning of the test that the temperature recorded by the thermocouple was 56 K higher than the value specified in the simulation. Despite this, the simulated temperature fits the experimental value very quickly, indicating a high thermal diffusivity.

### *ZU3 sample: reduced conductivity*

Given the results for ZU1 case with a factor of 0.55 applied to the effective thermal conductivity, it was decided to apply the same factor for ZU3 case. Indeed, as the same material was used, it was consistent to use the same values to evaluate if they did not depend on the flux or temperature level. Therefore, Figure 6.15 shows the results obtained for ZU3 case with the same reduced conductivity as for ZU1 case. An improvement of results can be seen in Figure 6.15(a), especially for the heating phase of TC2 where the relative difference of temperature is 6.6 % at 10 s. However the temperature for TC1 is still overestimated by 25.8 % at 10 s. The cooling phase TC2 and TC3 shows a bigger inertia than the experimental measurements would suggest, possibly indicating that the capacity to store energy and hence the heat capacity is too high. Figure 6.15(b) shows that temperatures for TCs 5 to 7 are all under-predicted for the heating phase, with relative differences of temperature of 6.5, 19.4, and 31.1 % respectively. The cooling phase shows the same inertia as for TCs 2 and 3.

It should be noted that given the maximum temperatures reached by TC 3, 5, and 6 (920, 792, and 894 K respectively) during the experiment, the resin of the material is certainly far from being totally decomposed. However, the values for heat capacity and effective conductivity were deduced from the experimental measurement of thermal diffusivity for a maximum decomposition at each temperature. This is certainly not the case for this experiment. This contributes to the difficulty to explain the thermal behaviour at low temperatures (TCs 3, 5 and 6), where temperature are under-estimated by the simulation with the reduced conductivity.

### **Charring degree results for ZU3 sample**

Figure 6.16 shows a comparison between the residual weight measured with Thermogravimetry analysis (TGA) presented in Section 6.1.2 and the char degree at the end of the present simulation of ZU3. The char degree corresponds to the sum of the reaction advancements over all pyrolysis reactions. A value of 0 for the char degree corresponds to a virgin material,

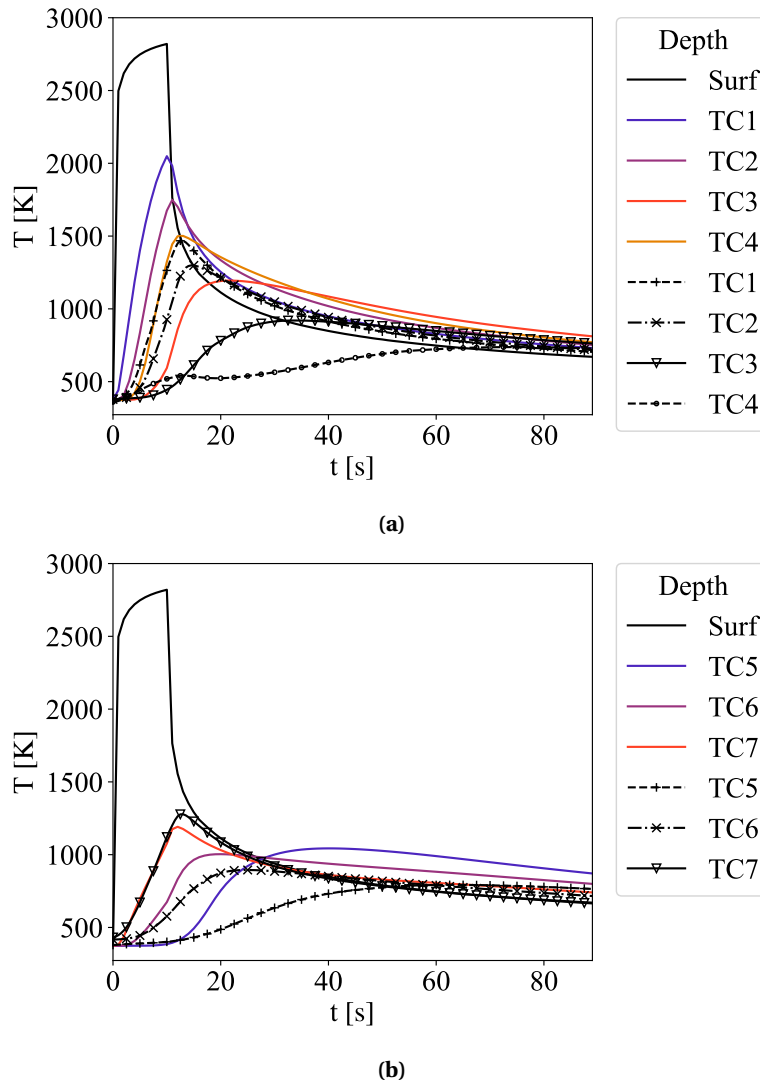


**Figure 6.14** – Comparison of thermocouple measurements in ZU1 sample (lines with symbols) to numerical temperature profiles (solid lines) at the corresponding depths, using the database thermal conductivity. (a) shows thermocouples at locations 1 to 4 (as per Figure 6.1(c)) and (b) shows thermocouples at locations 5 to 7 (as per Figure 6.1(c)).

while a value of 1 corresponds to a charred material. The residual weight is the most consistent parameter with char degree since it evaluates the proportion of carbon that is left in one sample. The constant residual weight for the virgin material is logically aligned with a char degree of 0.

The comparison is performed on the red line shown in Figure 6.4 as the TGA were made along this line.

The numerical values were almost in perfect agreement with the two measurements at 1.5 (1.1 % relative difference) and 4.5 mm (0.4 % relative difference) from the surface. The measurement at 7.5 mm is wrong and considered an outlier as the residual weight was smaller than the virgin material. Numerical char degree values differed from TGA measurements only by



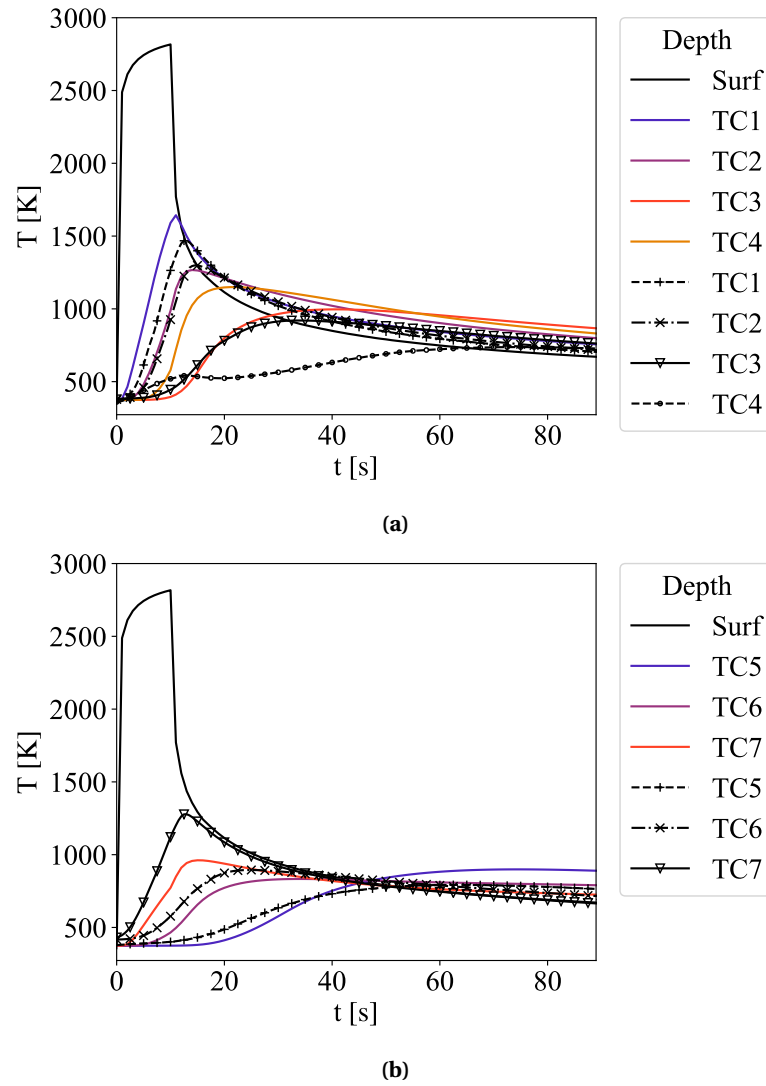


**Figure 6.15** – Comparison of thermocouple measurements in ZU1 sample (lines with symbols) to numerical temperature profiles (solid lines) at the corresponding depths, using the database thermal conductivity multiplied by a factor of 0.55. (a) shows thermocouples at locations 1 to 4 (as per Figure 6.1(c)) and (b) shows thermocouples at locations 5 to 7 (as per Figure 6.1(c)).

5.7 and 3.1 % at depth of 10.5 and 13.5 mm respectively.

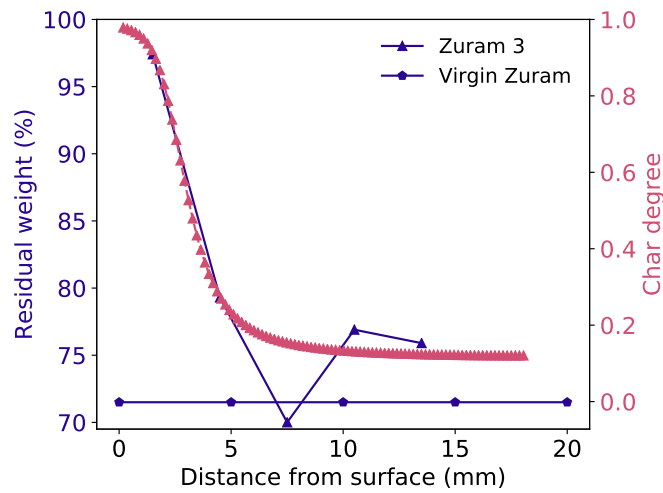


**Figure 6.16** – Comparison of numerical char degree values (pink curve with symbols) with normalised residual weight in TGA measurements (violet lines with symbols) for ZU3 case. Numerical values were obtained using the reduced effective conductivity.

## 6.2 HFSS tested ZURAM

In order to compare ZURAM testing in convective and radiative environment, ZURAM samples were tested in the HFSS. The rebuilding of this experiment will allow to assess whether a radiative flux facility such as the HFSS can be used to accurately test and model the thermo-chemical behaviour of a carbon-phenolic material like ZURAM.

### 6.2.1 Sample description and conditions

A sample similar to the one shown in Figure 4.2 was used, except with dimensions 25x25x20 mm. The thermocouples depths were 2, 8, 12 and 16 mm from the surface, arranged on a square centered on the sample. A centered thermocouple at 4 mm was also added. The pressure was set on all the surfaces equal to the ambient pressure.

The sample was exposed in the HFSS to a heat flux which distribution is shown in Figure 6.17. A peak heat flux of around  $1.0 \text{ MW m}^{-2}$  was chosen as this value corresponds to testing conditions of the PICA (Phenolic Impregnated Carbon Ablator) material at Sandia Solar Tower as described by White<sup>(97)</sup>.

ZURAM is also considered to act as a surface absorber in this section, and the ETC model is used to rebuild the HFSS experiments. Given the results presented in Section 6.1.4, the effective thermal conductivity to which a factor of 0.55 was applied is utilized as it appeared to represent more accurately the thermal properties of ZURAM. The ETC is still considered orthotropic and the through thickness values are applied to the main direction of heat transfer, i.e. from exposed to back surface.

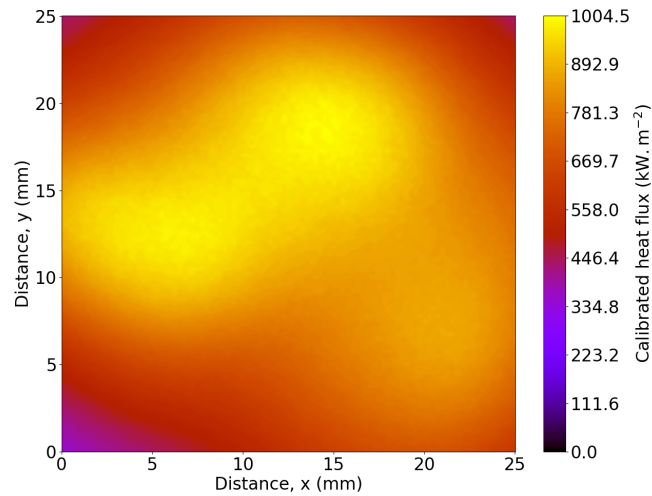


**Figure 6.17** – Flux distribution and magnitude to which the ZURAM was exposed in the HFSS

### Surface temperature BC

Based on the successful rebuilding of ZU1 and ZU3 that used a time-dependent Dirichlet BC, it was attempted to rebuild the ZURAM HFSS test by using surface temperatures recorded by the IR camera. The surface temperature profile on the center point shown in Figure 6.18(a) indicates that some issues were encountered for the IR camera measurements. Indeed the temperature drop from 30 s is not consistent with the TC measurements. The emissivity that was given as an input in the IR camera software could only be a constant. It was shown in a technical report<sup>(128)</sup> that the emissivity of ZURAM varies in the IR wavelength range changes as its surface changes in appearance. This variation was a first source of error for the IR measurements. On the other hand, Figure 6.18(b) shows the IR measured temperature distribution 33 s after the lamps were turned on. The temperature distribution was expected to look similar to the heat flux distribution shown in Figure 6.17. In this case, the surface temperature map at 33 s was very different from the flux one. This suggested that the emissivity change was not the only factor influencing the IR measurement. In fact, pyrolysis gases are ejected from the front surface. These gases contained carbon-based species which can significantly absorb radiation emitted from and arriving to the sample. Therefore, the HFSS ZURAM was rebuilt using a flux boundary condition.

### Front face exposed to flux BC

As briefly explained in the previous paragraph, the pyrolysis gases absorbed radiation emitted from the sample, but also radiation arriving to the exposed surface. For this reason, a factor was applied to the incoming heat flux given in Figure 6.17 to fit numerical data of the shallowest TC (2 mm) on experimental data and to see how the numerical data of other TCs behaved compared to measurements. Figure 6.19 shows the comparison between experimental and numerical data. It can be seen that the numerical data at 2 mm fitted well the experimental

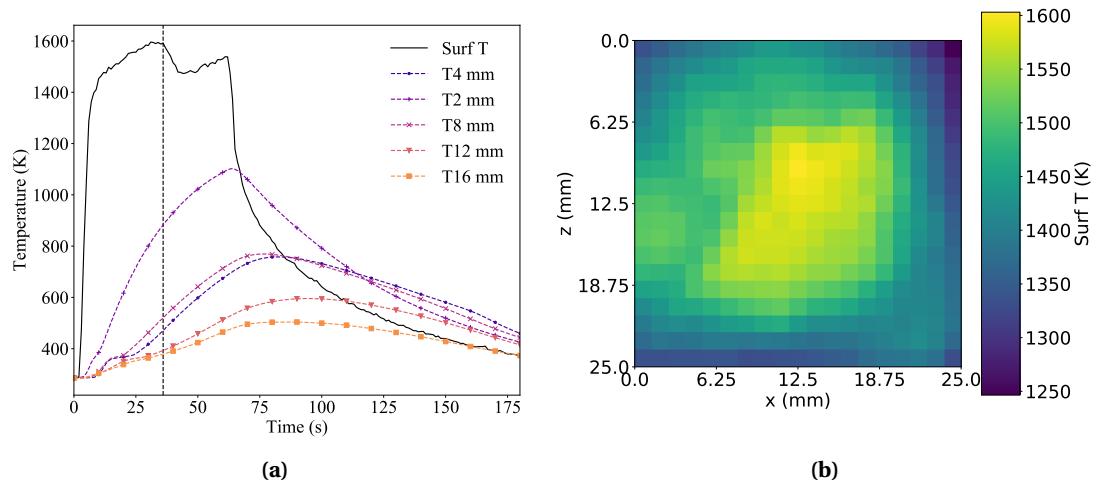


**Figure 6.18** – Temperature measurements of a ZURAM test in the HFSS at a peak heat flux of  $1.004 \text{ MW m}^{-2}$  (see Figure 6.17). (a) presents the surface temperature on the center point and all TC measurements. The TC at 4 mm is centered, while the others are arranged on a square centered on the sample. (b) shows the surface temperature measured by the IR camera 33 s after the lamps were turned on (vertical black dashed line in (a)).

measurement during the heating phase (2.3 % relative difference at 63 s, which corresponded to the end of the heating phase). The match between numerical and measured temperature at 4 mm is very good up until 15 s, time where the experimental data slowly rose from 360 to 373 K until 24 s. This clearly indicates that the TC measurement was influenced by the evaporation of water contained inside the sample. This observation is valid for all TCs, except that the smaller the heating rate at a given position the longer the evaporation time. Nevertheless, the slope of the numerical temperature profile at 4 mm was close to the experimental one. These remarks on the two shallowest TCs suggest that the model performed well at predicting heat transfer through the ZURAM sample. However, the comparison of measurements to numerical value for the other three TCs (8, 12 and 16 mm) demonstrates otherwise. Indeed, the deviations at the end of the heating phase are 39, 42, and 44 % at 8, 12 and 16 mm respectively. The temperature even decreases below ambient temperature for the two deepest TCs.

The analysis of whole temperature field showed that temperatures below 273 K occurred on the side surfaces, which is unexpected and most probably due to the expansion of gas leaving the sample. The comparison with surface temperatures of ZU1 and ZU3, for which the rebuilding was successful, proposes that the sides faces should be heated. In fact, the HFSS heat flux incident on the front face did vanish at the edge of the sample, which implies that an incoming heat flux should also be considered on the side faces whereas only cooling was taken into account.

### Flux BC on front and side faces

Considering the lamps used for this experiment (1, 2 and 3, see Figure 2.1(a)), and their positions relatively to the position of the sample (see Figure 2.1(c)) side faces can actually be irradiated, especially as the sample was not placed in the focal plane of the HFSS. It was

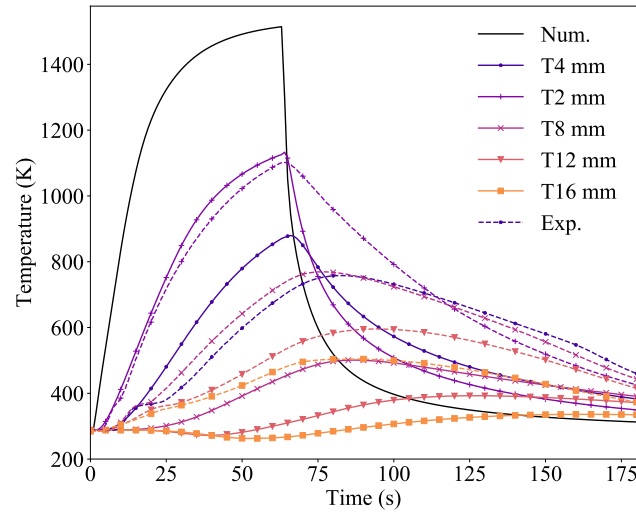


**Figure 6.19** – Comparison of numerical results (in plain lines) to experimental TC data (solid lines), when a radiative heat flux BC with a peak heat flux of  $1.004 \text{ MW m}^{-2}$ , and which distribution is shown in Figure 6.17, was applied on the exposed surface

assumed that the side faces received a flux that is homogeneous on their whole surface. The top face is expected to receive radiation from lamps 1 and 2, the bottom face from lamp 3, the side face on the left in Figure 2.1(c) from the three lamps, and the other slightly from lamp 1. According to this, the flux magnitudes that were applied on each side face are given in Table 6.7.

**Table 6.7** – Flux magnitudes set on the sides faces of the ZURAM sample to account for irradiation on the sides due to the small size of the sample. The left face correspond to the side face on the left in Figure 2.1(c), the right face to the other side.

Face	Top	Left	Bottom	Right
Flux ( $\text{kW m}^{-2}$ )	70.0	100.0	60.0	20.0

It can be seen in Figure 6.20 that the numerical simulation of temperatures corresponding to the deepest TCs was significantly improved when applying these incoming radiative fluxes on the side faces. Some discrepancies remained as the numerical profiles underestimated the slopes for TC 8, 12 and 16 mm during the heating phase. However, the temperatures at 2 mm matched in the heating phase, whereas the numerical profile at 4 mm still overestimated the temperature because of water evaporation.

The cooling phase was not as well predicted as for the ZU1 case. This can be explained by the much better controlled atmosphere in the VKI Plasmatron, where the gas was at rest when the torch was turned off. On the contrary, the room and lamps ventilations were still incident on the sample and they are sources of uncertainties for the numerical modeling of that type of test.

More generally, the fitting of numerical results to experimental measurements is dependent

on the BCs during both heating and cooling phases, and on the ETC that changes between the heating and cooling phases due to the change of material state. To better estimate the ETC using HFSS tests, the BCs should be better controlled.

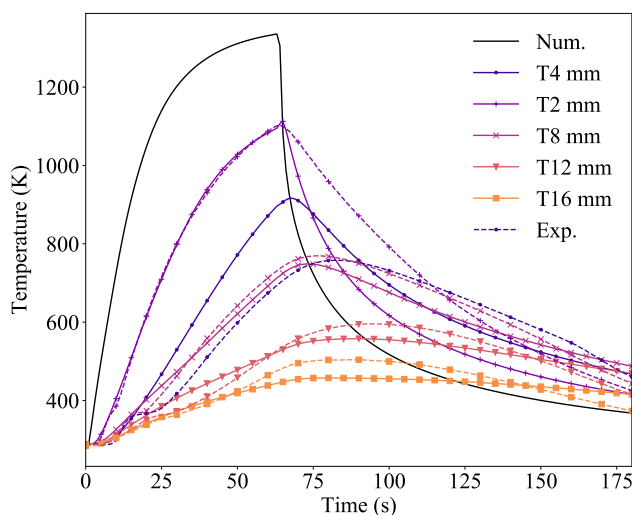


**Figure 6.20** – Comparison of numerical results (solid lines) to experimental TC data (in dashed lines), when a radiative heat flux BC with a peak heat flux of  $1.004 \text{ MW m}^{-2}$ , and which distribution is shown in Figure 6.17, was applied on the exposed surface. Radiative heat fluxes BCs, which detailed values can be found in Table 6.7 were also applied on the side faces.

### 6.3 Conclusions

Tests in the VKI's Plasmatron provided experimental data and good quality tested samples. TGA, XPS and SEM measurements were successfully performed to determine the charring degree profile through the thickness of those tested samples. ZU1 and ZU3 tests were successfully numerically rebuilt using material thermochemical properties and time-dependent surface temperatures retrieved by the VKI. As the determination of the properties of materials such as ZURAM is an on-going process, an "ad hoc" factor was applied to the ETC thermal conductivity given in the database. It led to numerical results that showed very good agreement with the thermocouple data given the complexity of processes occurring in this type of material. The lower temperature ZU1 test simulation produced errors on the temperatures of less than 5 % for all the hotter thermocouples during the heating phase. The deviations for the hotter ZU3 tests were more important (up to 25 % for the hottest thermocouple), but still very good for 2 thermocouple. The comparison of the charring degree measured using TGA and that provided by the numerical simulations showed that PATO's thermochemical model performs well to reproduce the material state, which is very important for the accurate prediction of thermal properties during the simulations.

The rebuilding of the proposed test in the HFSS was also successful as the model attained reasonable discrepancies compared to thermocouple measurements. The "ad hoc" factor was applied to be consistent with VKI tests. However, it needed substantial adjustments on BCs

in the numerical simulations. In opposition to VKI's experiments, where surface temperatures could be accurately measured over all the exposed surface because the plasma flow blows the pyrolysis gas away, IR camera measurements in the HFSS were disrupted by the outgoing pyrolysis gases. No data could be recorded on the sides faces either, which required extra assumptions on radiative heating of these faces. For a material with such complex thermo-chemical processes, the BCs have to be better controlled and/or known to allow accurate numerical simulations. Nevertheless, this experiment showed that high radiative flux artificial solar facilities such as HFSS are a good alternative for testing space materials like ZURAM. The environmental chamber described in Chapter 2 can allow to better control the atmosphere around the tested sample. However, the radiative flux inside the chamber would need to be characterized since borosilicate can absorb part of the light and that the chamber walls are 5 mm thick. It is also recommended to design an experiment where the BCs on the sides of the sample are known, such as the sample holder described by White<sup>(97)</sup> that prevented incoming radiation from uncontrollably heating the sample.





## 7 Summary and Outlook

### 7.1 Summary

This thesis deals with the testing and modeling of heat transfer in complex heterogeneous materials. The evaluation of their thermal properties has been achieved. Two types of materials are considered in this work: ceramic foams for concentrated solar applications and a carbon-phenolic material called ZURAM, for space applications. They have been tested in extreme environments, i.e. high-temperature and high-flux environments. The High-Flux Solar Simulator (HFSS) is a powerful and versatile facility that allows testing materials and devices in a wide range of concentrated radiative solar-like fluxes. ZURAM has been tested in a convective flux environment, the VKI Plasmatron, in order to compare the testing capabilities of the HFSS, which is a radiative environment. A novel approach to evaluate the effective thermal conductivity (ETC) of ceramic foams is proposed. A fully radiation-conduction coupled method is implemented in order to quantify the limitations of an ETC model, and to dispose of a tool capable of simulating accurately heat transfer through highly porous materials in the presence of strong external irradiation. The thermochemical response of a material like ZURAM is successfully simulated using the PATO code, to which a new library to account for time varying spatially resolved boundary conditions is added.

In Chapter 2, the experimental tools are described. The HFSS, the associated equipment and the flux measurement procedure are detailed. The design of the environmental chamber brings new testing possibilities in the HFSS. Indeed, it allows for a better control of the test environment for multiple reasons. First, the lamps' fans produce an air flow towards the tested samples but the characteristics of this flow, namely its magnitude, its direction, its cross-section, are still unknown. The use of the chamber would block it. Second, the chamber offers the possibility to perform test under a non-air atmosphere, which helps limiting phenomena like oxidation for instance. Finally tests can be done at pressures as low as 1.0 mbar, which is a strong asset in the case of testing space application materials like ZURAM intended for space applications..

Chapter 3 introduces the numerical tools developed and implemented in this work. The PATO

code is extended with a new library that permits the use of a time varying spatially resolved Dirichlet or Neumann boundary condition (BC). Such conditions already existed in PATO, but it was only possible to use a constant or axisymmetrical distribution of BC values. A novel numerical-experimental approach to retrieve the ETC of ceramic foams from tests in the HFSS is implemented. It is based on an iterative process that take advantage of the transient and steady-state thermal behavior of the material. It uses surface temperature distributions that are measured by the infrared camera as BC. A fully parallelised path-length based Monte-Carlo (MC) ray-tracing (RT) code is then developed to resolve the radiative transfer equation and effectively treat conduction and radiation separately. It uses a continuum approach considering two semi-transparent phases, which effective radiative properties are known or assumed. Scattering is taken into account and the scattering phase function can be used even though it was not in this work. The MC solver is coupled to PATO within an algorithm called PATORAC. PATO provides the temperature field to the MCRT code which solves for the divergence of the radiative heat flux in all cells of the finite volume mesh. The divergence of radiative flux is incorporated in the energy equation as an extra source term. The coupling frequency can be adapted depending on the thermal inertia of the considered material. The change of effective radiative properties in the case of state changing materials like ZURAM can thus be considered.

ETCs retrieved for five different types of ceramic foams using the iterative process described in Chapter 3 are presented in Chapter 4. The proposed approach proves to give ETC values that are consistent with those found in literature. The ETC increases as the porosity decreases. The results are especially convincing for an alumina sample exhibiting a high extinction coefficient (small pore size). It is mainly noticed that incoming radiation -and its magnitude- has a strong influence on ETC values. Indeed, a coated sample exhibited an ETC up to 46 % smaller at low temperature than an uncoated sample in the presence of a  $1.0 \text{ MW m}^{-2}$  peak flux. Similarly, the ETC retrieved with an incoming flux eight times lower was significantly lower.

The PATORAC algorithm is then used to simulate the radiation-conduction heat transfer with a more advanced approach (in Chapter 5). The temperature profiles through the thickness of the sample confirmed how the ETC of a sample with low extinction coefficient can be overestimated in the presence of external irradiation. A parametric study on the porosity, extinction coefficient and thermal bulk conductivity allows to suggest a range of applications where the ETC model is sufficient to accurately predict the thermal response of heterogeneous materials, and where it is not sufficient.

Finally, Chapter 6 presents material analyses and numerical rebuilding of ZURAM tests performed in extreme environments. A ZURAM sample tested in the VKI Plasmatron, an arc-jet facility providing a convective flux environment, is analysed to quantify its charring degree, which is compared to numerically rebuilt values. The simulations of VKI Plasmatron tests provided temperature profiles showing good agreement with experimental data, given the thermal properties of ZURAM measured by the VKI to which an ad-hoc factor was applied. The same properties are used to rebuild a ZURAM experiment in the HFSS. This numerical simulation highlights the fact that the sides of cuboidal samples are irradiated during experiments in the HFSS. However, the flux levels on these sides are unknown and difficult to

estimate. The recommendation would be to better control, or directly measure the sides' surface temperatures. Nevertheless, temperature measurements using the infrared camera show to be inaccurate because they are strongly disrupted by pyrolysis gases ejected from the decomposing ZURAM sample.

## 7.2 Achievements

The experimental setup and methodology described in Chapter 2 enabled testing porous heterogeneous materials in high radiative flux conditions with an excellent reproducibility, therefore meeting objective O.1. This achievement provides a consistent methodology for future tests in the HFSS.

The pseudo-inverse experimental-numerical approach described in Chapter 3 and the results presented in Chapter 4 guarantee the achievement of objective O.2. This innovative engineering method allows to retrieve temperature dependent ETCs of highly porous materials for a large temperature range using only one test in the HFSS.

The successful implementation of the MC code described in Chapter 3 meets objective O.3. The code is capable of considering scattering and also offers the possibility to account for different states of the simulated materials, like in the case of decomposing space-application materials.

The implementation of the coupled conduction-radiation algorithm described in Chapter 3 meets objective O.4. This more advanced approach provides a tool to accurately simulate heat transfer in highly porous materials in the presence of strong irradiation, when an ETC model is not adapted.

The sensitivity study detailed in Chapter 5 provided guidelines to assess the limits of application of an ETC model in the presence of strong irradiation. Objective O.5 is therefore met. The guidelines offer the possibility to save resources as they give the range of application of both approaches, depending on the requirements on the accuracy of the simulated temperatures.

The comparison of the numerical rebuilding of tests in the HFSS and the VKI Plasmatron, showed that the HFSS is a reliable alternative to conventional testing of space-application materials. Consequently, objective O.6 is met. The material analyses to quantify the char degree of tested samples in the VKI Plasmatron allowed to show that the kinetics implemented in PATO can describe carbon-phenolic material decomposition with a good accuracy.

## 7.3 Outlook

The HFSS is a powerful and versatile facility that is now proven to be capable of testing a large number of different heterogeneous materials. However, it is imperative to improve the experimental setups. Indeed, material characterization in the HFSS cannot be done without

accurately modeling the heat transfer in the tested sample. Therefore, it is essential to know precisely the boundary conditions on all faces, whether in terms of temperature or flux. Characterizing the flow created by the fans cooling the HFSS lamps would clearly help evaluating the convective heat flux on the front face. The sides BCs are still poorly characterized. The first suggestion is to directly measure the surface temperature on those faces using the infrared camera, but it probably would not work with ZURAM. Designing a new sample holder (or a complement to the existing water-cooled sample holder) that block external irradiation on the sides, as presented by White<sup>(97)</sup>, would certainly be ideal, especially when testing ZURAM-like materials. It would offer the possibility to control the incoming flux, but also to measure the temperature on the side faces using thermocouples.

In addition to offering the possibility to perform tests in a controlled atmosphere, with different gases and pressures, the environmental chamber can provide a good solution to avoid the flow from the lamps' fans from reaching the tested sample. Nevertheless, the flux reaching a sample inside the chamber must be characterized too. On one hand, the bubble made of borosilicate might slightly act as a concentrating lens. On the other hand, the borosilicate transmittance is known to be between 0.9 and 0.95, which hence decreases the radiative flux reaching the sample. Temperature measurement inside the chamber with the infrared camera is possible through a small ZnSe window. It requires adapting the measurement technique as the camera must be placed much closer to the chamber if any spatial resolution of the temperature is needed.

Temperature measurements using thermocouples in heterogeneous highly porous insulators, as performed in Chapter 4, is often questioned. Due to their higher thermal conductivity compared to the tested samples, they can act as heat sinks. It was attempted to investigate the difference between setups where the TCs were inserted from the sides and from the back. However, it was done without the thermocouple holder, and the sample position was not consistent between tests. It led to discrepancies that could not be explained by the difference in thermocouples setup. It is recommended to try another campaign to determine precisely the heat sink effect of the TCs. This effect could also be investigated numerically. Indeed, the simulation domain could include a sub-domain assigned with the conductivity on the thermocouples. The heat flux transported by the thermocouples could be quantified. Both thermocouples configurations (from the back and the sides) could be investigated, taking advantage of numerical simulations to avoid costly experiments.

The method used to determine the ETCs in Chapter 4 was done by manually adapting the ETC at every iteration. This approach allowed to successfully retrieve ETCs, but it was tedious. Automating the procedure would improve importantly the efficiency of the method. Special care should be taken to make sure that heating rates are accounted for, which is the way that the pseudo-inverse method described in this work took advantage of the transient thermal behavior of the materials. Implementing an inverse method could be considered. However, one limitation of inverse methods is that it is difficult to show the uniqueness of the retrieved solution. Taking into consideration the measurements of five thermocouples in an inverse method can also be problematic.

Convection was neglected in Chapters 4 and 5. This heat transfer mode also interacts with

conduction and radiation. In the case of the ceramic foams studied in this thesis, convection was certainly negligible given their small pore sizes. Nevertheless, for materials that exhibit extinction coefficients as low as  $256 \text{ m}^{-1}$ , the pore size is of the order of 4 mm, and convection would be significant. PATO is capable of taking into account convection, like it was done in Chapter 6 for the simulation of the thermal response of ZURAM.

Moreover, with such pore sizes, the assumption of local thermal equilibrium would not be guaranteed anymore. PATO also features the possibility of considering non-equilibrium between the solid and gas phases. However, the MC code does not. It is recommended to upgrade the MC code where the solid and gas temperatures should be given as input for each cell of the domain.

The radiative transfer model implemented in the MCRT code could be improved. The materials studied in this thesis are assumed gray. Spectrally resolving the absorption and extinction coefficients would help further and better understand the macroscopic radiative transfer in heterogeneous semi-transparent media. Studying the influence of the scattering phase function on the radiative transfer, of which the MCRT code is capable, is also suggested to improve the model. The investigation of the radiative transfer at the pore level, especially for materials like ZURAM, is proposed to assess the validity of assumptions made at the macroscale. The pore-level study would also help to assess the local thermal (non-) equilibrium.

The results presented in Chapter 5 are purely numerical and experimental data would be very valuable to validate the numerical results and refine the model. Specifically designed experiments in the HFSS could help provide this data. It is suggested to perform a test on samples of varying porosity and pore sizes, with the peak flux positioned on the edge of the sample. This way the intensity variation through the sample can be measured using the CCD camera. The side surface temperature can also be recorded with the infrared camera.

This thesis shows that the HFSS is a good alternative to arc-jet facilities to test carbon-phenolic materials like ZURAM in order to collect data to improve thermochemical response models. However, as already explained, it requires setup adjustments to the control boundary conditions. Nonetheless, in addition to quantifying the mass loss, which would also be possible in arc-jet facilities, recession velocity can easily be measured with the CCD camera as a first approach. As the environmental chamber gives the possibility to work under a controlled atmosphere, measuring the composition of the pyrolysis gases ejected from the samples could be performed with the gas chromatograph available at the Laboratory of Renewable Energy Science and Engineering. This type of data could prove to be very valuable for the validation of chemical models implemented in advanced codes such as PATO.

Finally, the HFSS heat flux flexibility and the controlled environment provided by the environmental chamber could help develop new specific materials manufacturing processes. Indeed, varying the gas composition and temperature during a process such as the sintering of ceramics could create new ways to achieve special designs and properties of materials.



# Appendix

## A Manufacturing drawings

Figure A.1 shows the technical drawing of the holes to be machined according to the thermocouple arrangement presented in Section 2.1.3.

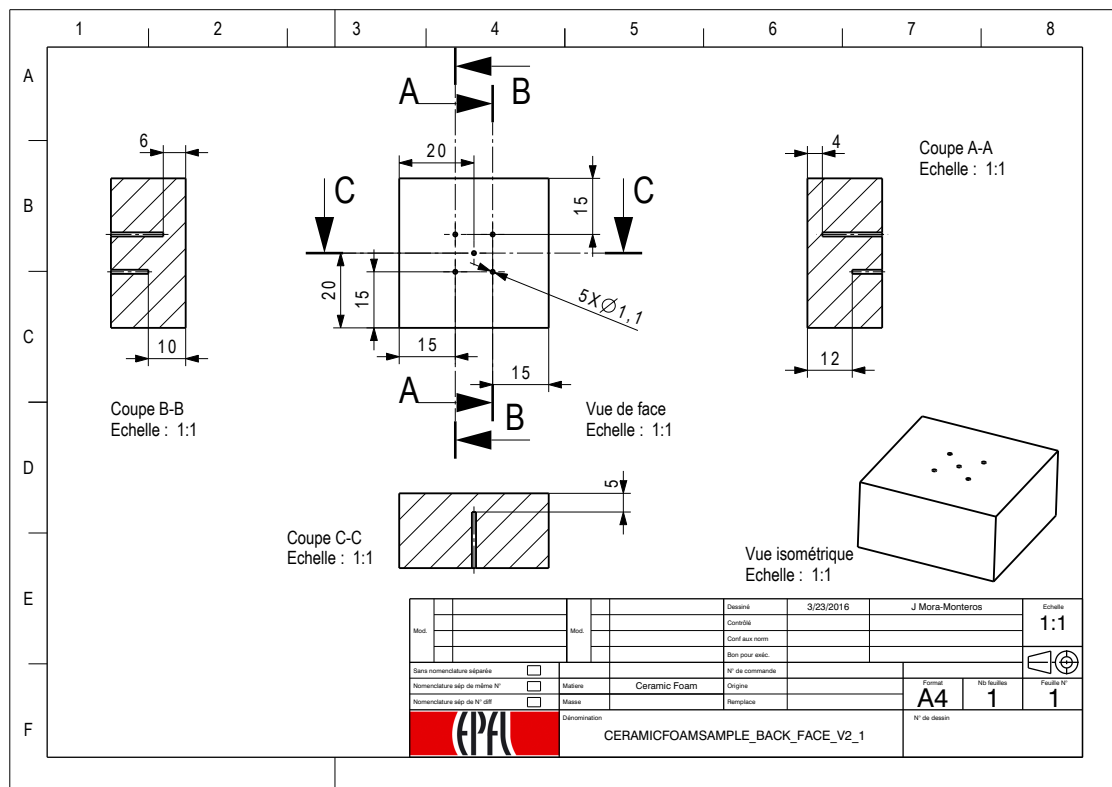


**Figure A.1** – Technical drawing of holes to be machined in tested samples. The holes are arranged according to the thermocouples arrangement fixed by the thermocouple mounting block (see Section 2.1.3)

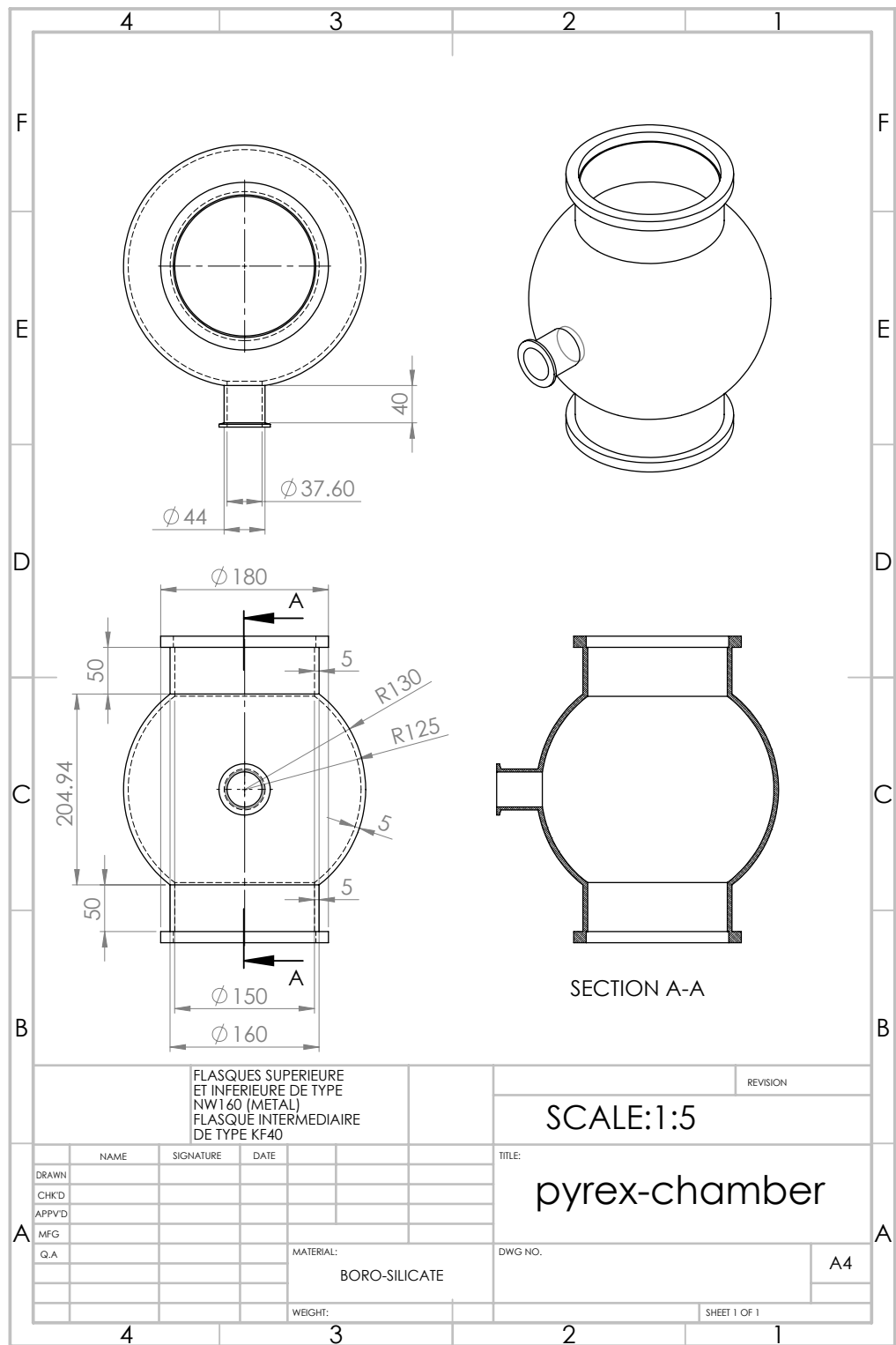


Figure A.2 – Spherical chamber with ISO160 flanged ends and a KF40 flange window port



## B Temperature profiles for conduction-radiation modeling

This appendix contains several extra plots obtained with the PATORAC algorithm in Chapter 5 to help understand the thermal behavior of the studied material in function of the porosity, extinction coefficient and bulk conductivity factor.

### B.1 Temperature dependent bulk conductivity, $1449.5 \text{ kW m}^{-2}$ peak heat flux value

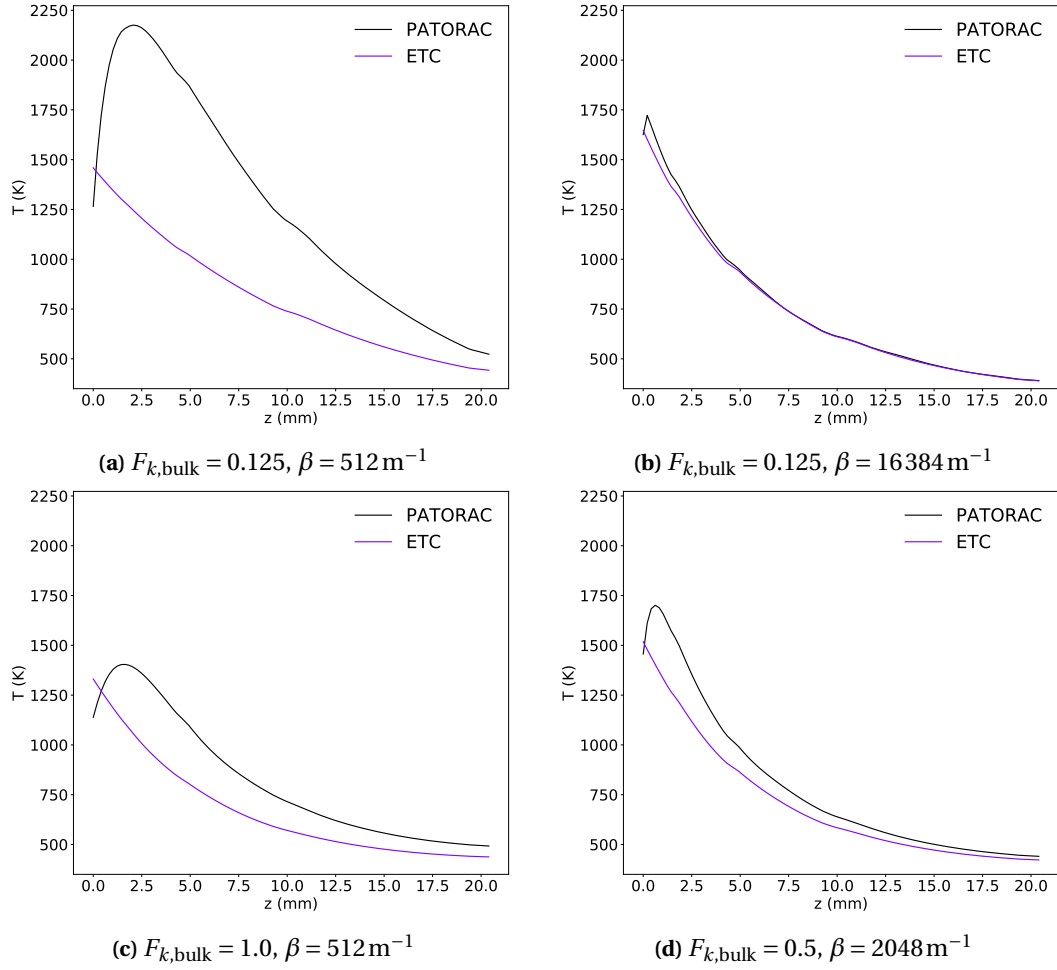


**Figure B.3** – Temperature profiles obtained with the PATORAC algorithm with a peak value of incoming radiative heat flux of  $1449.5 \text{ kW m}^{-2}$  through a 95 % porosity sample with temperature dependent thermal properties, for four  $(F_{k,bulk}, \beta)$  couples.

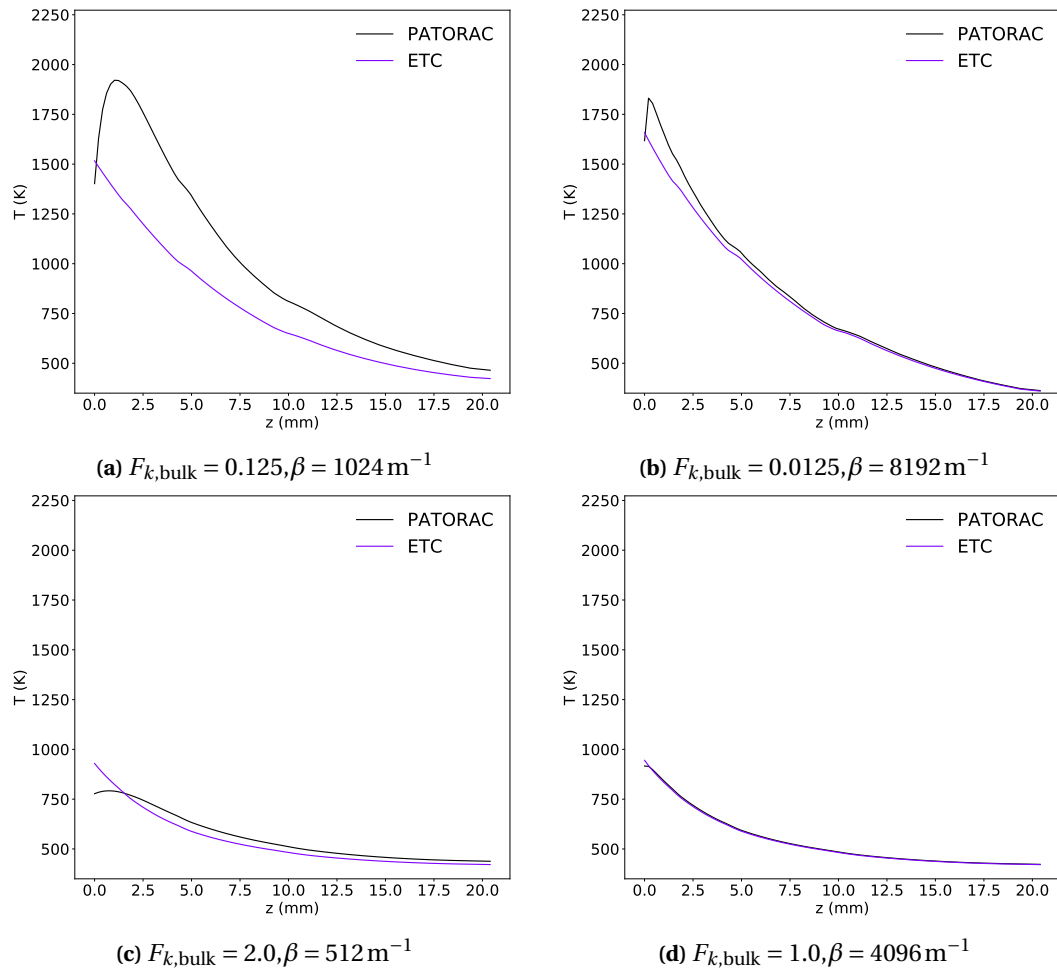


**Figure B.4** – Temperature profiles obtained with the PATORAC algorithm with a peak value of incoming radiative heat flux of  $1449.5 \text{ kW m}^{-2}$  through a 90 % porosity sample with temperature dependent thermal properties, for four  $(F_{k,bulk}, \beta)$  couples.

## B. Temperature profiles for conduction-radiation modeling

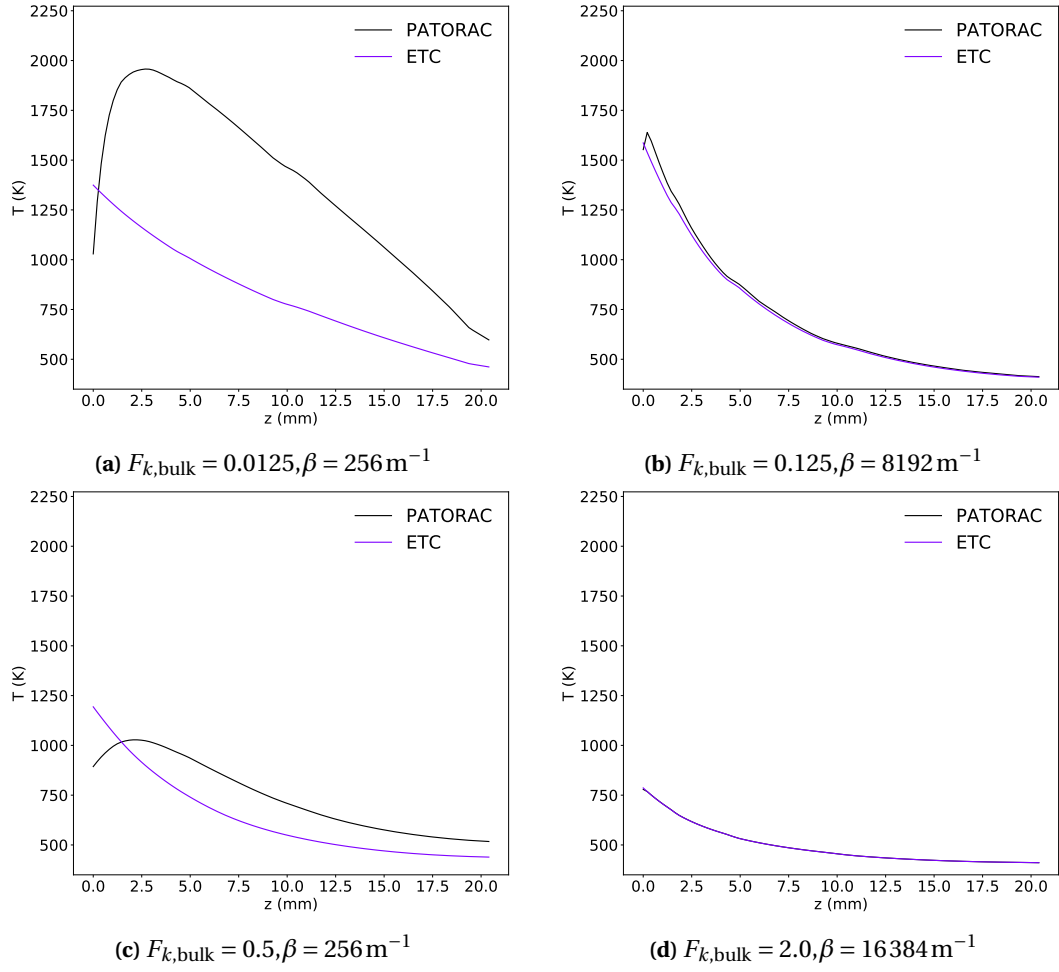


**Figure B.5** – Temperature profiles obtained with the PATORAC algorithm with a peak value of incoming radiative heat flux of  $1449.5 \text{ kW m}^{-2}$  through a 85 % porosity sample with temperature dependent thermal properties, for four  $(F_{k,bulk}, \beta)$  couples.

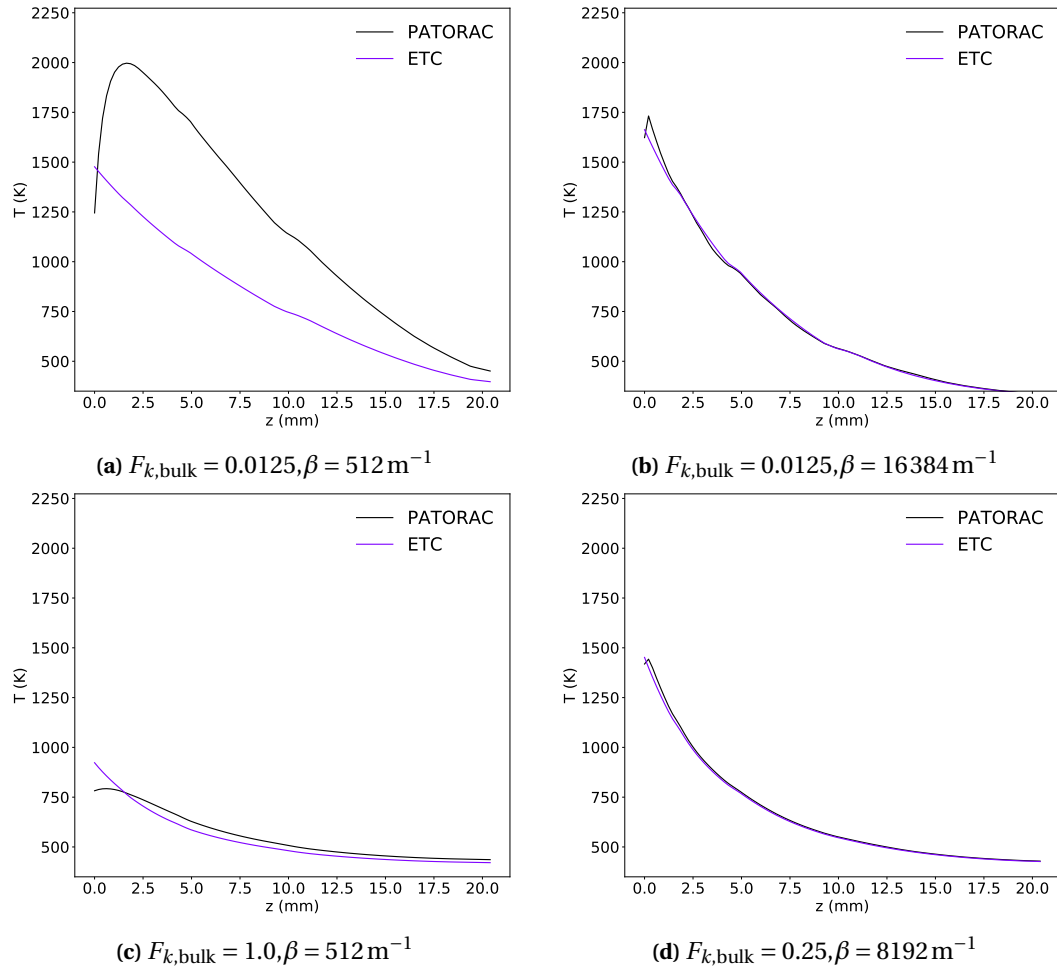


**Figure B.6** – Temperature profiles obtained with the PATORAC algorithm with a peak value of incoming radiative heat flux of  $1449.5 \text{ kW m}^{-2}$  through a 80 % porosity sample with temperature dependent thermal properties, for four  $(F_{k,bulk}, \beta)$  couples.

## B. Temperature profiles for conduction-radiation modeling

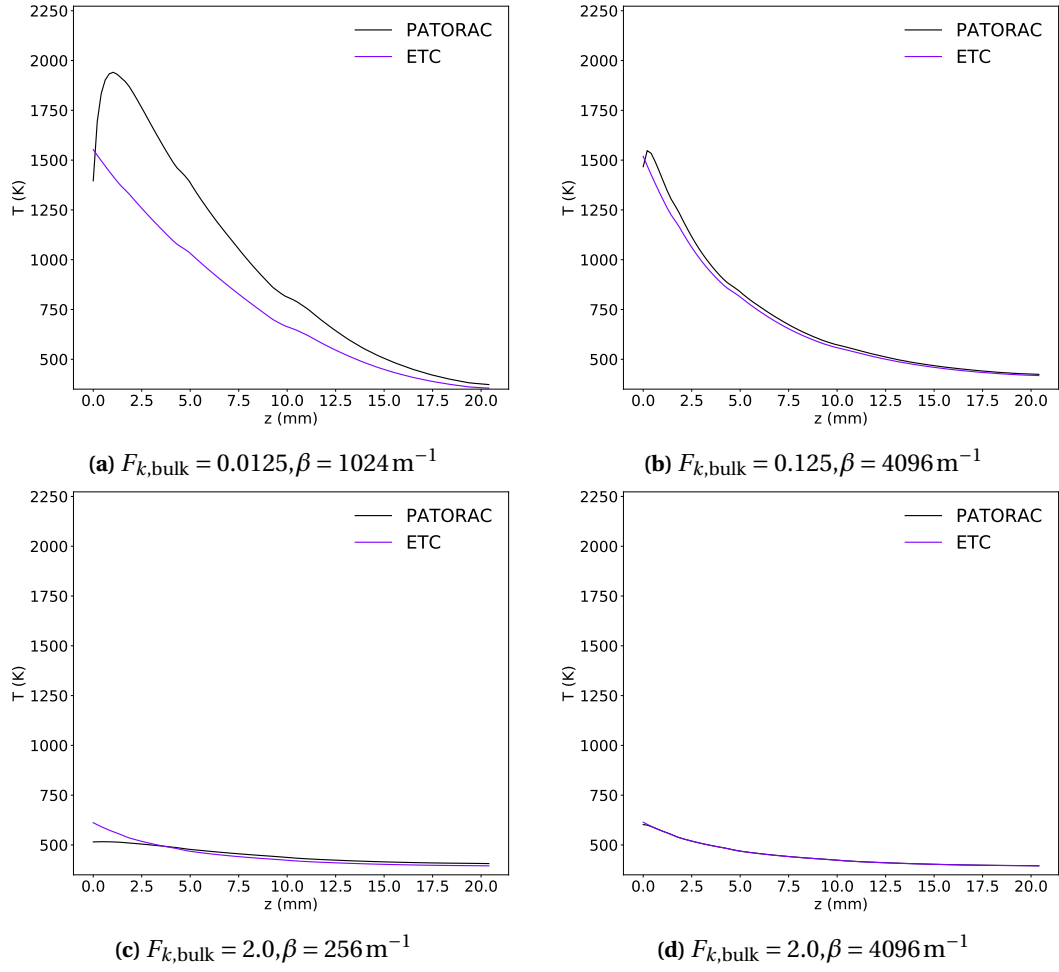


**Figure B.7** – Temperature profiles obtained with the PATORAC algorithm with a peak value of incoming radiative heat flux of  $1449.5 \text{ kW m}^{-2}$  through a 75 % porosity sample with temperature dependent thermal properties, for four  $(F_{k,bulk}, \beta)$  couples.

## B.2 Temperature independent thermal properties, $1449.5 \text{ kW m}^{-2}$ peak heat flux value

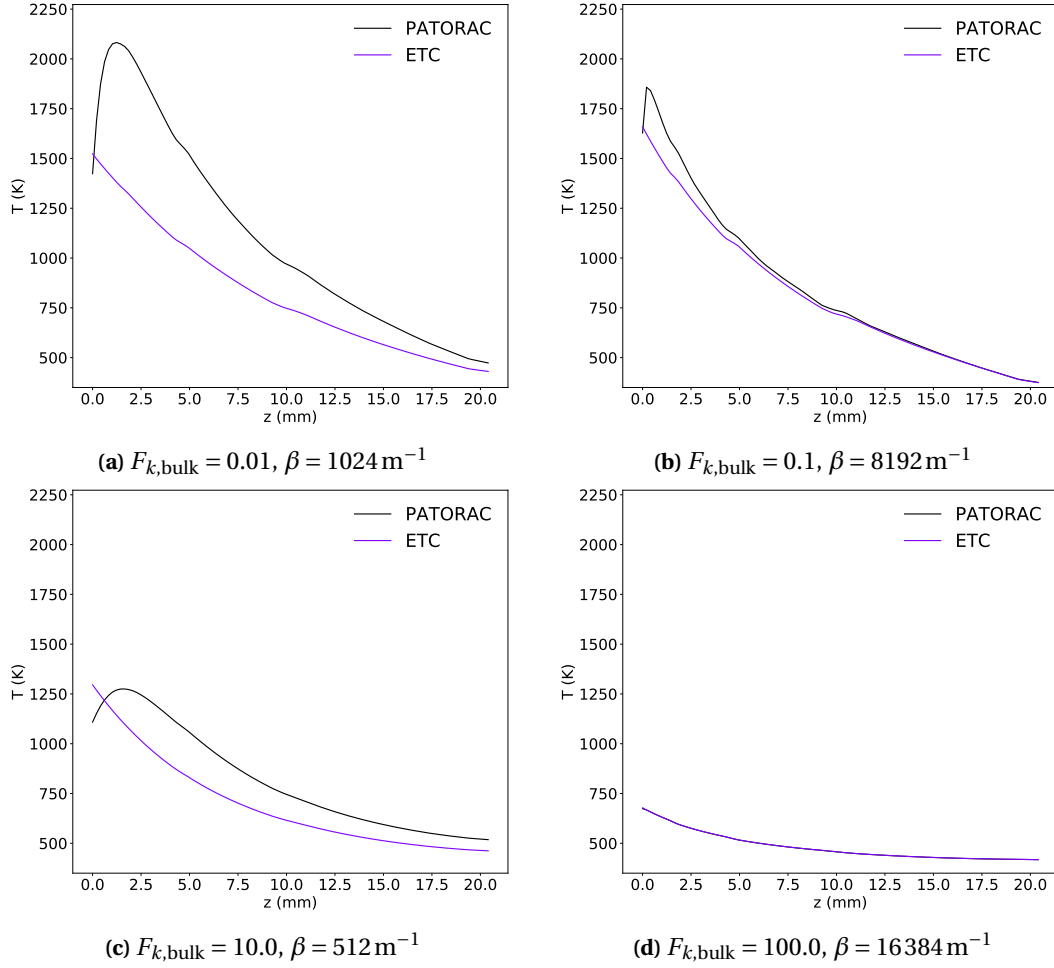


**Figure B.8** – Temperature profiles obtained with the PATORAC algorithm with a peak value of incoming radiative heat flux of  $1449.5 \text{ kW m}^{-2}$  through a 95 % porosity sample with temperature independent thermal properties, for four  $(F_{k,bulk}, \beta)$  couples.

## B. Temperature profiles for conduction-radiation modeling

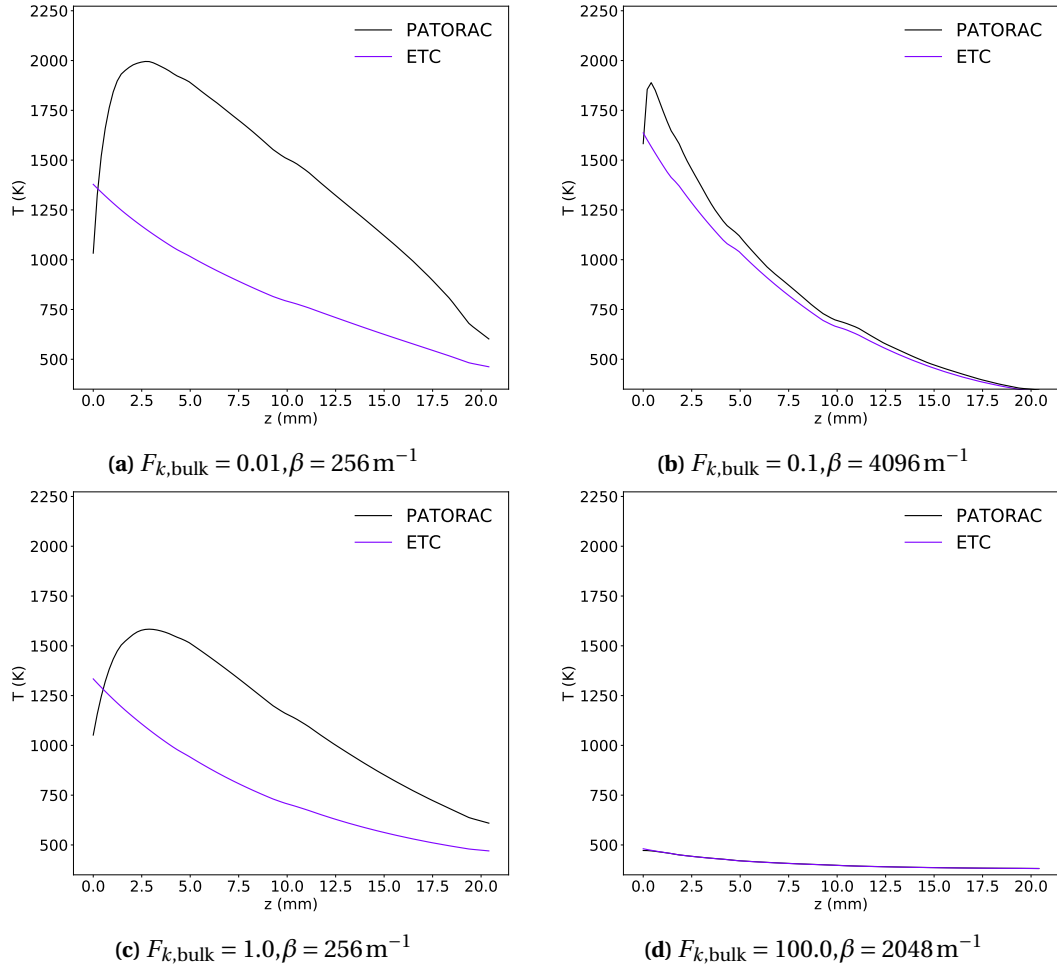


**Figure B.9** – Temperature profiles obtained with the PATORAC algorithm with a peak value of incoming radiative heat flux of  $1449.5 \text{ kW m}^{-2}$  through a 85 % porosity sample with temperature independent thermal properties, for four  $(F_{k,bulk}, \beta)$  couples.

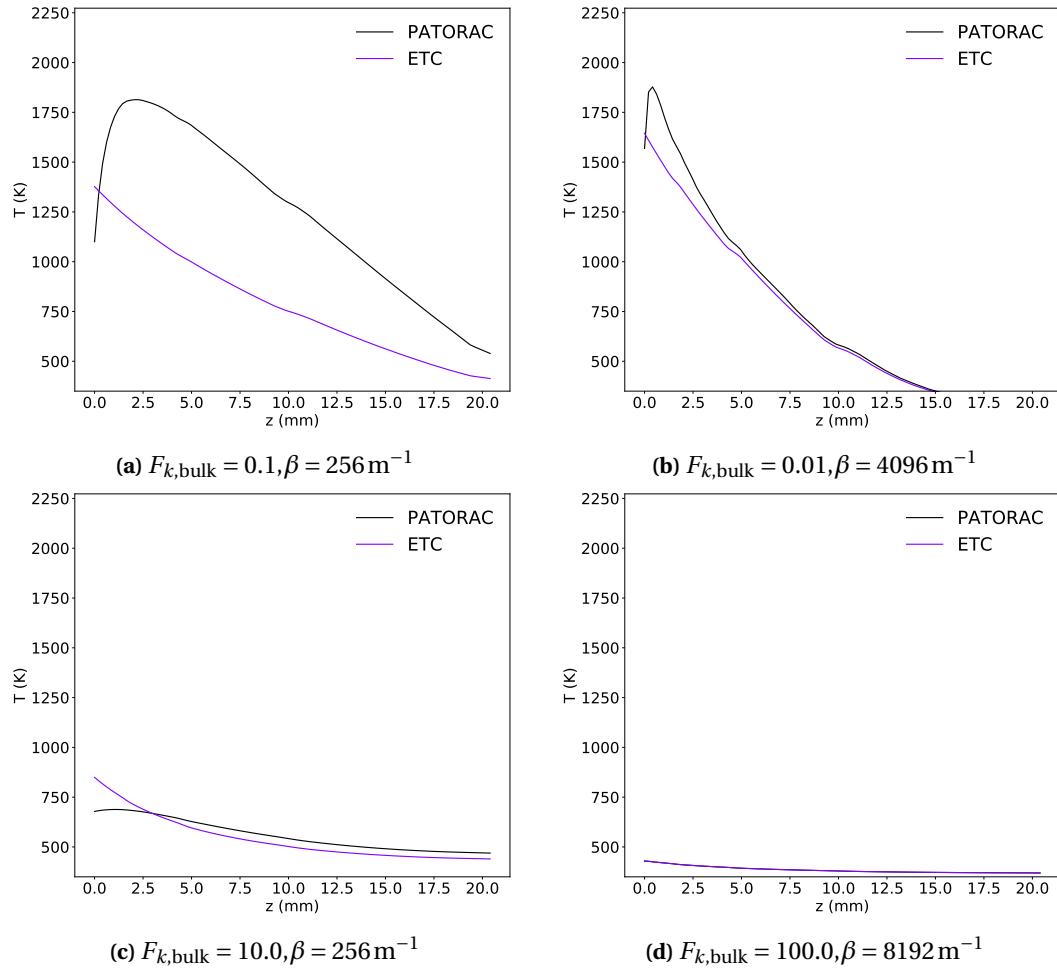


**Figure B.10** – Temperature profiles obtained with the PATORAC algorithm with a peak value of incoming radiative heat flux of  $1449.5 \text{ kW m}^{-2}$  through a 75 % porosity sample with temperature independent thermal properties, for four  $(F_{k,bulk}, \beta)$  couples.



### B.3 Temperature dependent bulk conductivity, $2222.6 \text{ kW m}^{-2}$ peak heat flux value

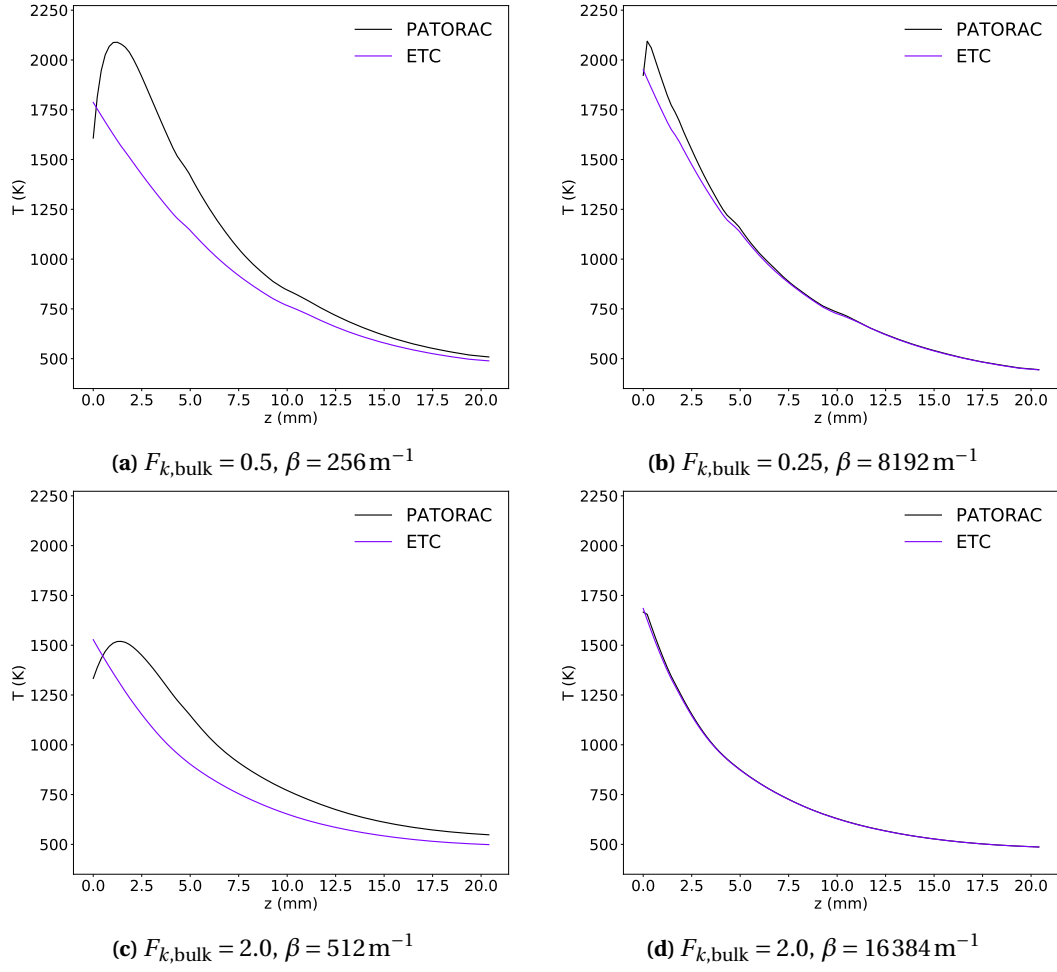


**Figure B.11** – Temperature profiles obtained with the PATORAC algorithm with a peak value of incoming radiative heat flux of  $2222.6 \text{ kW m}^{-2}$  through a 95 % porosity sample with temperature dependent thermal properties, for four  $(F_{k,bulk}, \beta)$  couples.

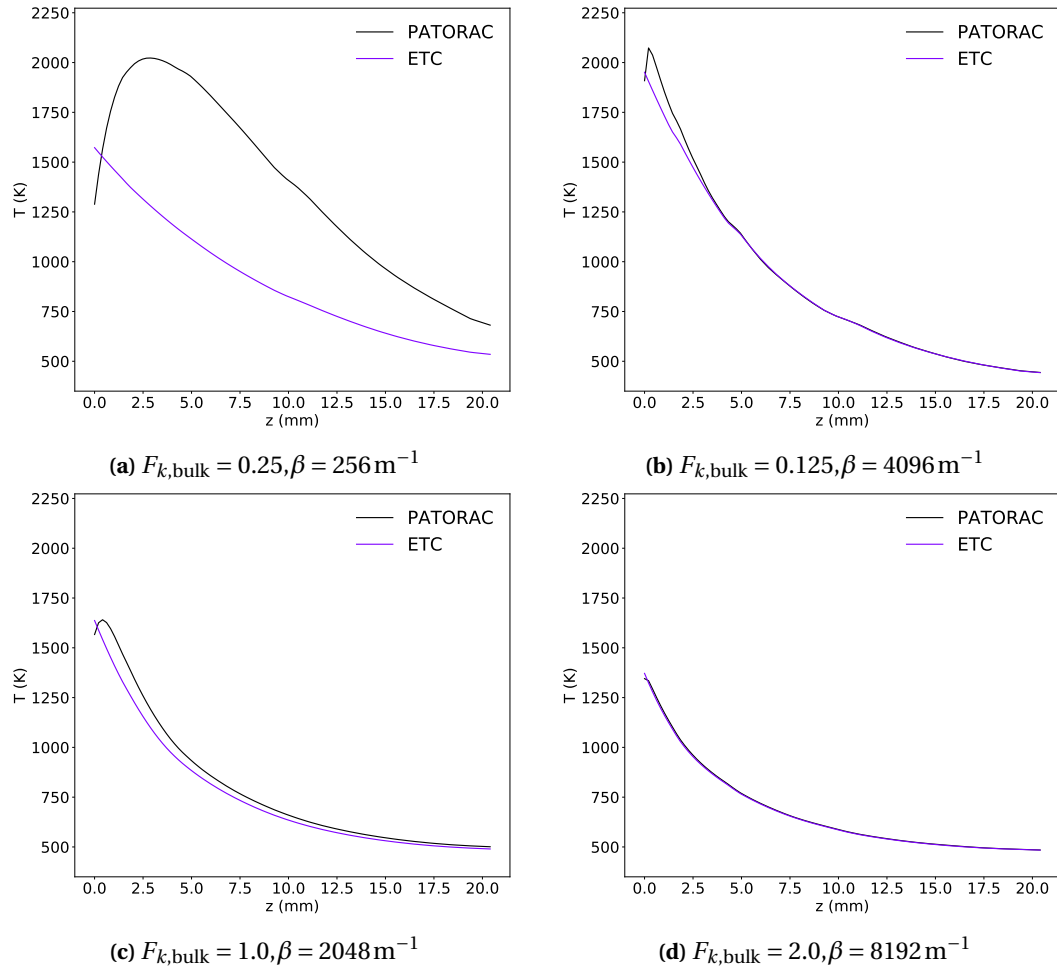


**Figure B.12** – Temperature profiles obtained with the PATORAC algorithm with a peak value of incoming radiative heat flux of  $2222.6 \text{ kW m}^{-2}$  through a 90 % porosity sample with temperature dependent thermal properties, for four  $(F_{k,bulk}, \beta)$  couples.

## B. Temperature profiles for conduction-radiation modeling

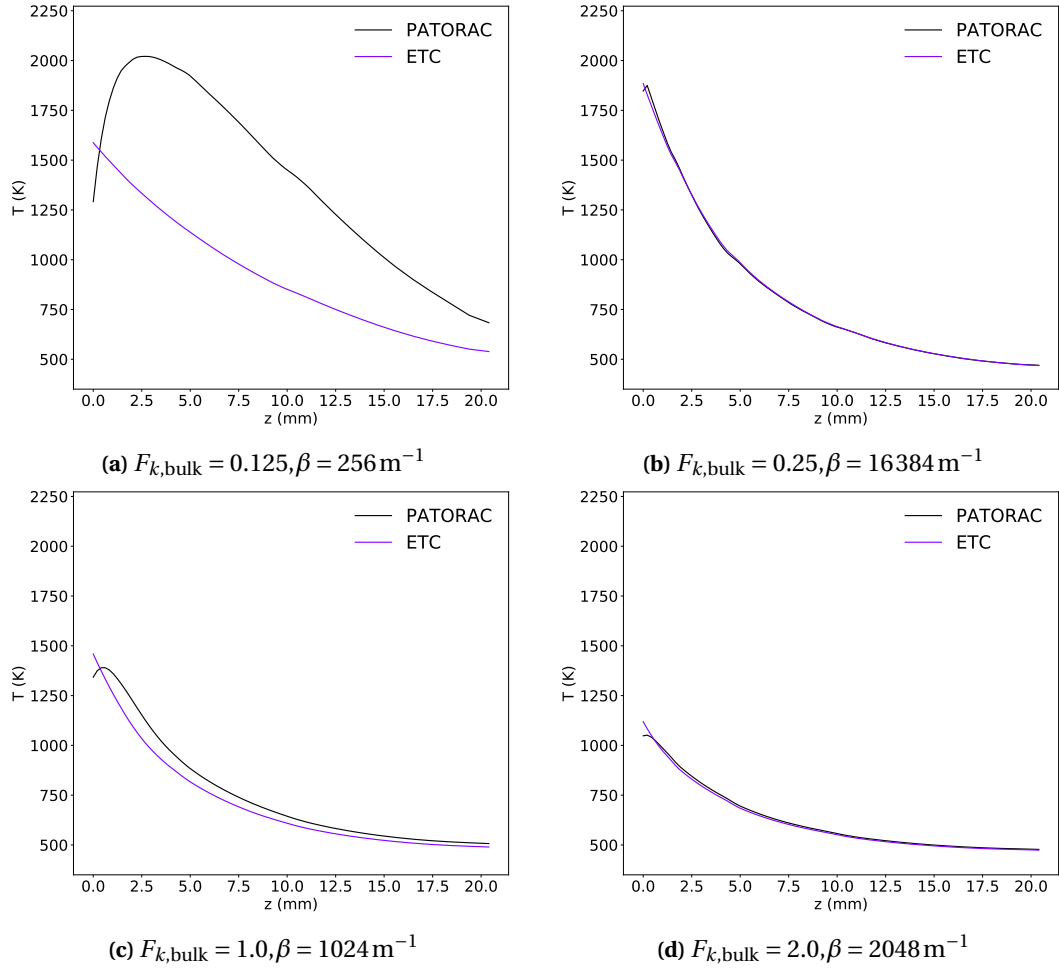


**Figure B.13** – Temperature profiles obtained with the PATORAC algorithm with a peak value of incoming radiative heat flux of  $2222.6 \text{ kW m}^{-2}$  through a 85 % porosity sample with temperature dependent thermal properties, for four  $(F_{k,bulk}, \beta)$  couples.

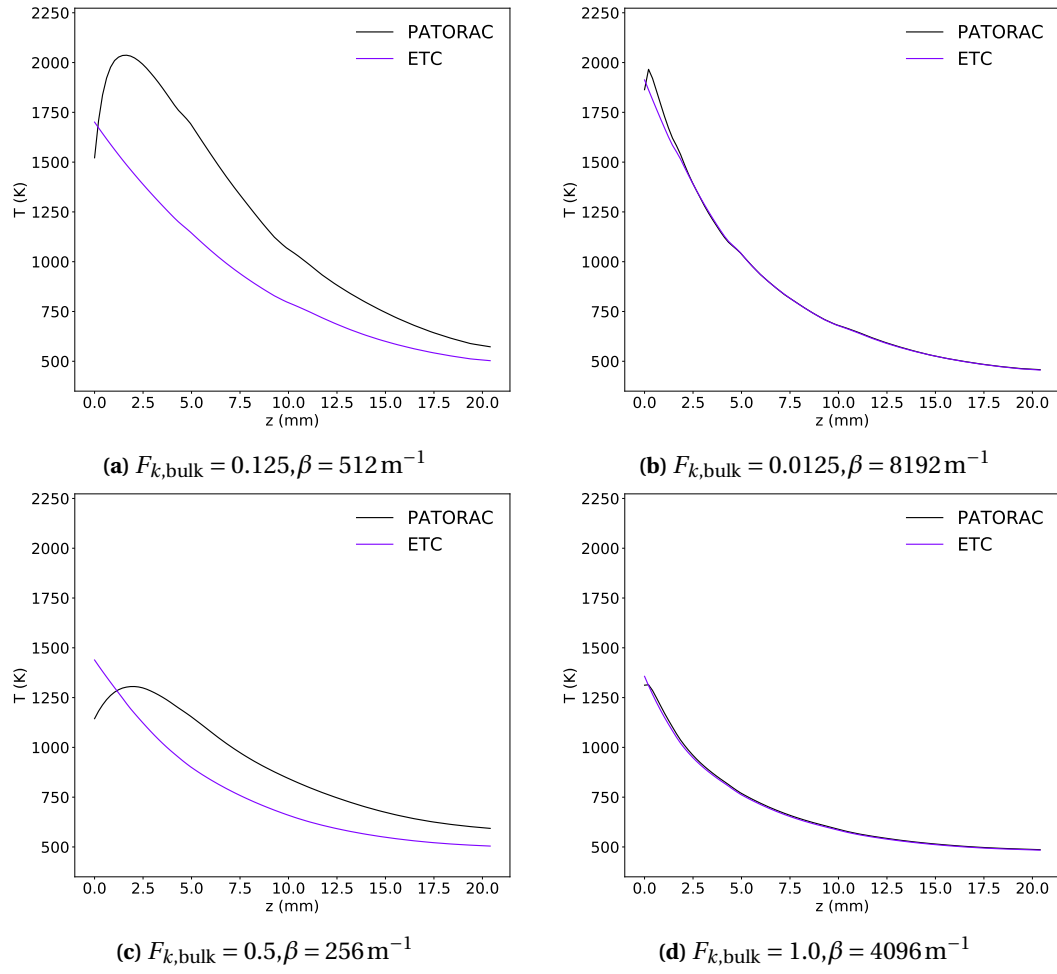


**Figure B.14** – Temperature profiles obtained with the PATORAC algorithm with a peak value of incoming radiative heat flux of  $2222.6 \text{ kW m}^{-2}$  through a 80 % porosity sample with temperature dependent thermal properties, for four  $(F_{k,bulk}, \beta)$  couples.

## B. Temperature profiles for conduction-radiation modeling

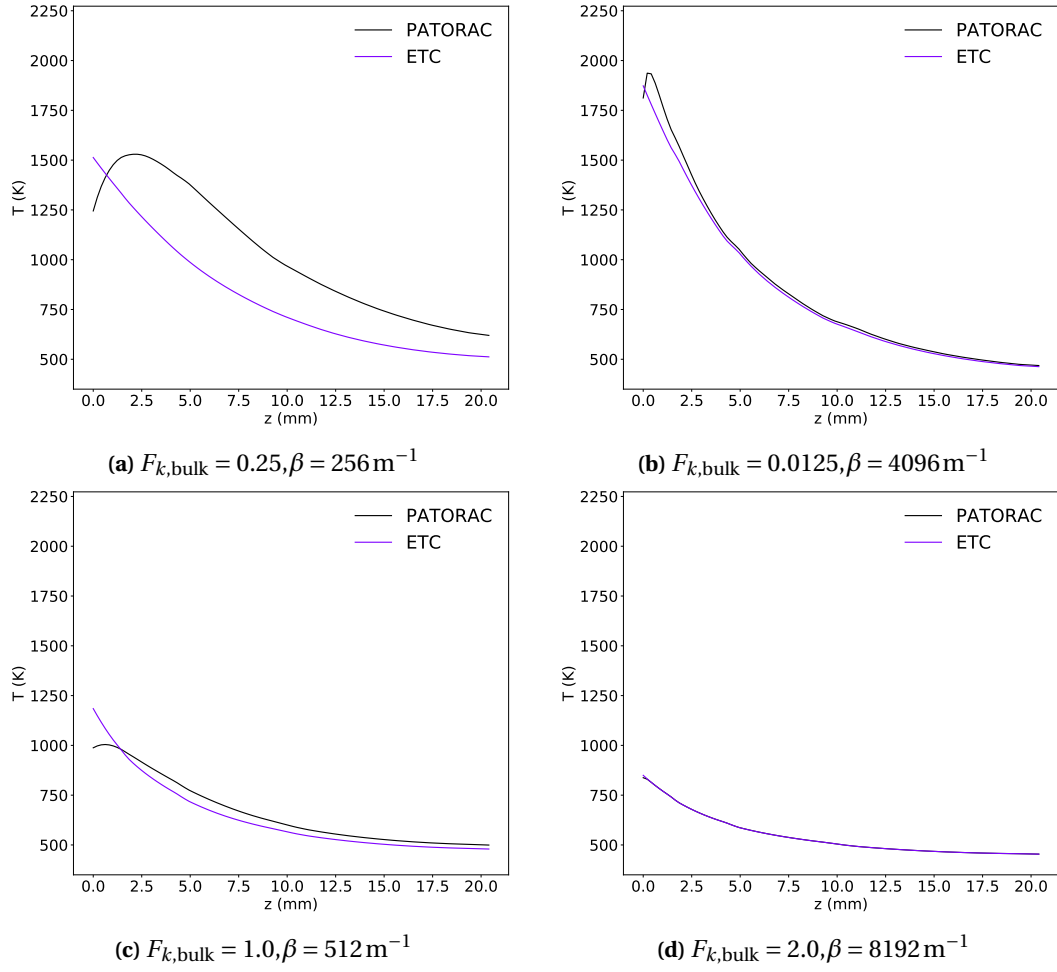


**Figure B.15** – Temperature profiles obtained with the PATORAC algorithm with a peak value of incoming radiative heat flux of  $2222.6 \text{ kW m}^{-2}$  through a 75 % porosity sample with temperature dependent thermal properties, for four  $(F_{k,bulk}, \beta)$  couples.

#### B.4 Temperature independent thermal properties, $2222.6 \text{ kW m}^{-2}$ peak heat flux value

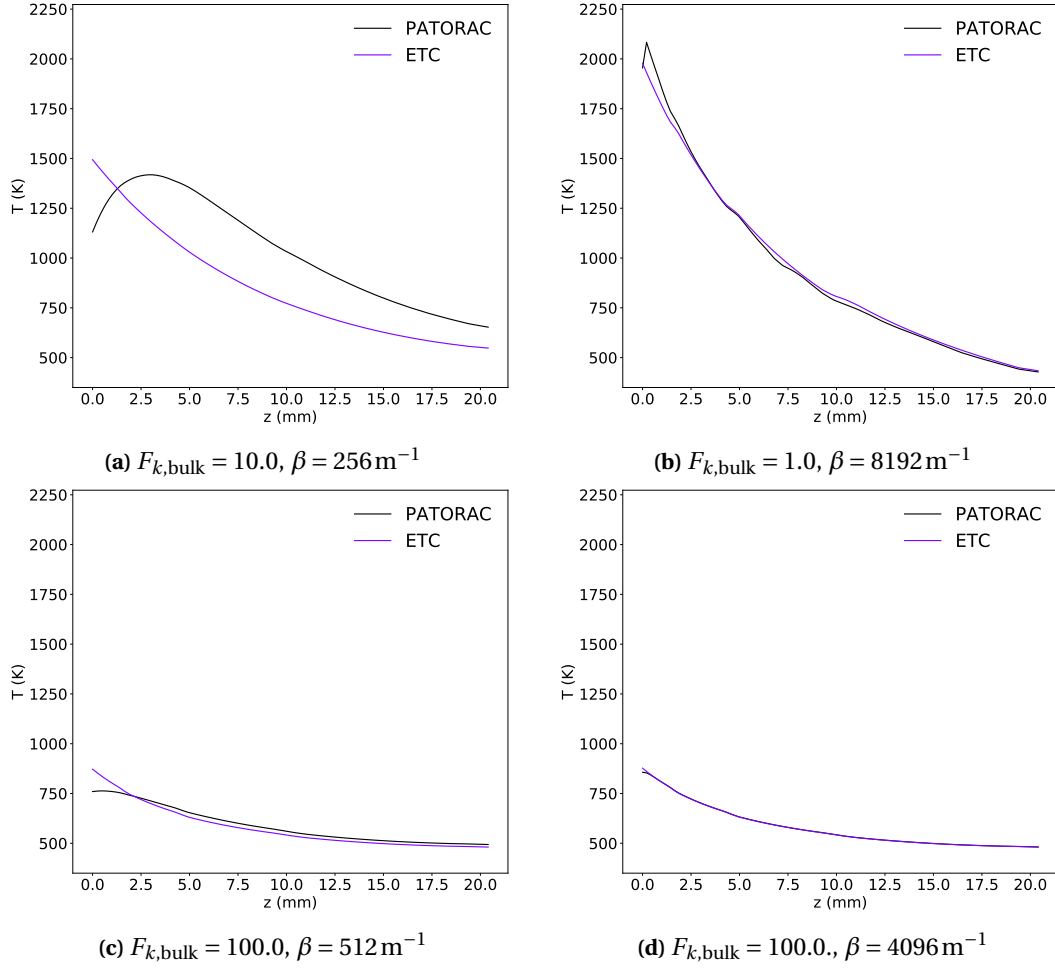


**Figure B.16** – Temperature profiles obtained with the PATORAC algorithm with a peak value of incoming radiative heat flux of  $2222.6 \text{ kW m}^{-2}$  through a 95 % porosity sample with temperature independent thermal properties, for four  $(F_{k,bulk}, \beta)$  couples.

## B. Temperature profiles for conduction-radiation modeling

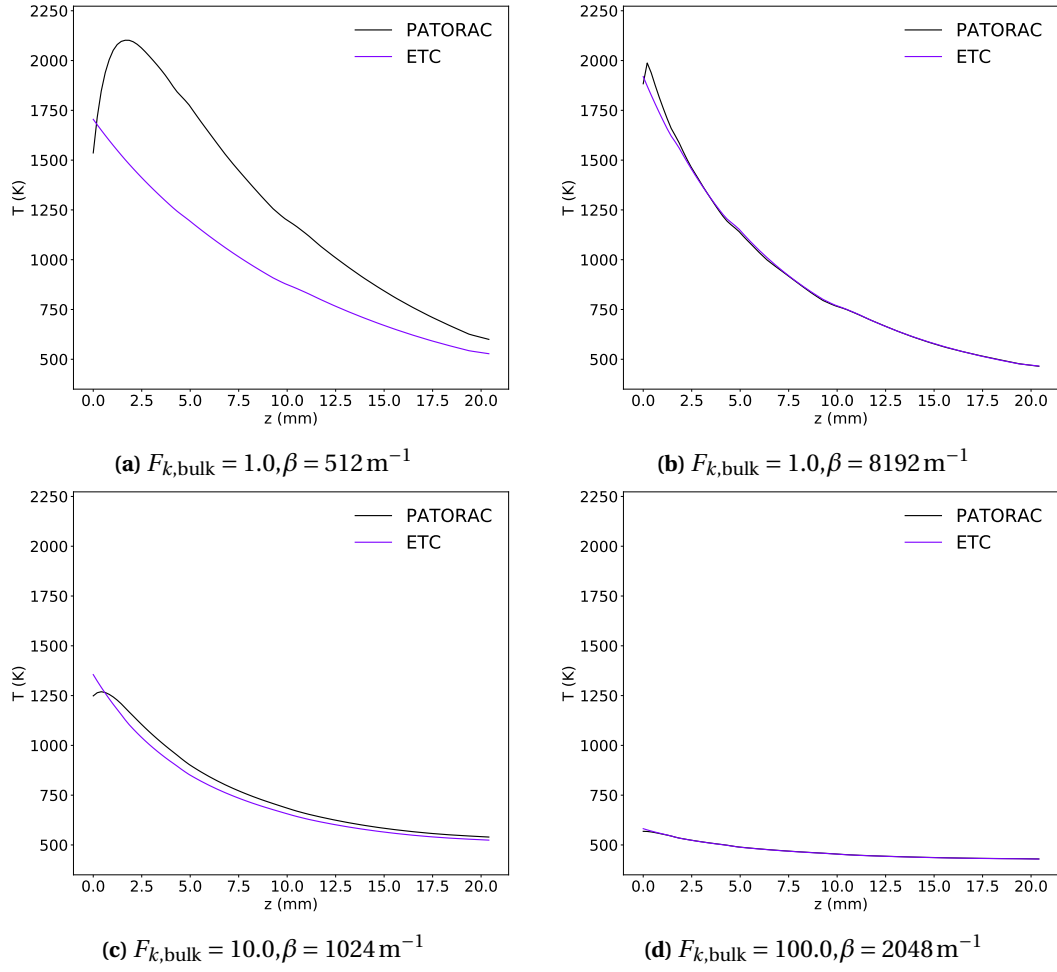


**Figure B.17** – Temperature profiles obtained with the PATORAC algorithm with a peak value of incoming radiative heat flux of  $2222.6 \text{ kW m}^{-2}$  through a 85 % porosity sample with temperature independent thermal properties, for four  $(F_{k,bulk}, \beta)$  couples.

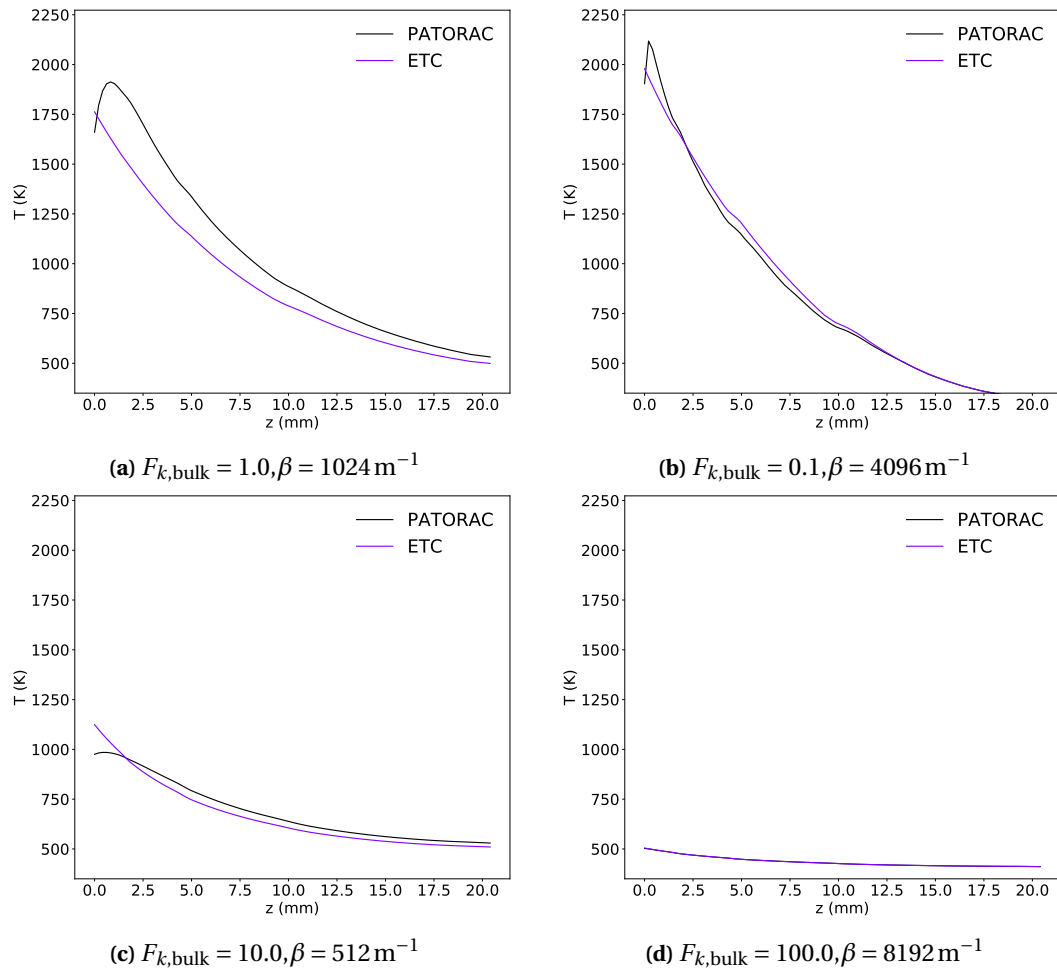


**Figure B.18** – Temperature profiles obtained with the PATORAC algorithm with a peak value of incoming radiative heat flux of  $2222.6 \text{ kW m}^{-2}$  through a 75 % porosity sample with temperature independent thermal properties, for four  $(F_{k,bulk}, \beta)$  couples.



# Bibliography

- [1] van de Krol, R. and Grätzel, M., editors, *Photoelectrochemical Hydrogen Production*, Vol. 102 of *Electronic Materials: Science & Technology*, Springer US, Boston, MA, 2012. [1]
- [2] Lewis, N. S., Crabtree, G., Nozik, A. J., Wasielewski, M. R., and Alivisatos, A. P., “Basic Research Needs for Solar Energy Utilization,” *Basic Energy Sciences Workshop on Solar Energy Utilization*, 2005. []
- [3] Lewis, N. S. and Nocera, D. G., “Powering the planet: Chemical challenges in solar energy utilization,” *Proceedings of the National Academy of Sciences*, 2006. [1]
- [4] Singh, G. K., “Solar power generation by PV (photovoltaic) technology: A review,” 2013. [1]
- [5] Cotal, H., Fetzer, C., Boisvert, J., Kinsey, G., King, R., Hebert, P., Yoon, H., and Karam, N., “III-V multijunction solar cells for concentrating photovoltaics,” 2009. [1]
- [6] Vossier, A., Chemisana, D., Flamant, G., and Dollet, A., “Very high fluxes for concentrating photovoltaics: Considerations from simple experiments and modeling,” *Renewable Energy*, 2012. []
- [7] Philipps, S. P., Bett, A. W., Horowitz, K., and Kurtz, S., “Current status of concentrator photovoltaic (CPV) technology,” Tech. rep., National Renewable Energy Lab.(NREL), Golden, CO (United States), 2015. [1]
- [8] Royne, A., Dey, C. J., and Mills, D. R., “Cooling of photovoltaic cells under concentrated illumination: A critical review,” *Solar Energy Materials and Solar Cells*, 2005. [1]
- [9] Kodama, T., “High-temperature solar chemistry for converting solar heat to chemical fuels,” 2003. [1]
- [10] Haussener, S. and Steinfeld, A., “Effective Heat and Mass Transport Properties of Anisotropic Porous Ceria for Solar Thermochemical Fuel Generation,” *Materials*, 2012. []
- [11] Maag, G., Lipiński, W., and Steinfeld, A., “Particle-gas reacting flow under concentrated solar irradiation,” *International Journal of Heat and Mass Transfer*, 2009. []

## Bibliography

---

- [12] Levêque, G., Bader, R., Lipiński, W., and Haussener, S., “High-flux optical systems for solar thermochemistry,” *Solar Energy*, 2017. [1]
- [13] Karni, J., Kribus, A., Rubin, R., and Doron, P., “The “Porcupine”: A Novel High-Flux Absorber for Volumetric Solar Receivers,” *Journal of Solar Energy Engineering*, 1998. [1]
- [14] Ávila-Marín, A. L., “Volumetric receivers in Solar Thermal Power Plants with Central Receiver System technology: A review,” *Solar Energy*, 2011. []
- [15] Wu, Z., Caliot, C., Flamant, G., and Wang, Z., “Coupled radiation and flow modeling in ceramic foam volumetric solar air receivers,” *Solar Energy*, 2011. [1]
- [16] Lachaud, J., van Eekelen, T., Scoggins, J. B., Magin, T. E., and Mansour, N. N., “Detailed chemical equilibrium model for porous ablative materials,” *International Journal of Heat and Mass Transfer*, Vol. 90, nov 2015, pp. 1034–1045. [2, 23, 24]
- [17] Mendes, M. A., Ray, S., and Trimis, D., “A simple and efficient method for the evaluation of effective thermal conductivity of open-cell foam-like structures,” *International Journal of Heat and Mass Transfer*, Vol. 66, nov 2013, pp. 412–422. [2, 3]
- [18] Coquard, R., Rochais, D., and Baillis, D., “Experimental investigations of the coupled conductive and radiative heat transfer in metallic/ceramic foams,” *International Journal of Heat and Mass Transfer*, Vol. 52, No. 21-22, oct 2009, pp. 4907–4918. [4, 48, 49, 50]
- [19] Petrasch, J., Schrader, B., Wyss, P., and Steinfeld, A., “Tomography-Based Determination of the Effective Thermal Conductivity of Fluid-Saturated Reticulate Porous Ceramics,” *Journal of Heat Transfer*, Vol. 130, No. 3, mar 2008, pp. 32602–32610. [2, 3]
- [20] Salmon, D., “Thermal conductivity of insulations using guarded hot plates, including recent developments and sources of reference materials,” *Measurement Science and Technology*, Vol. 12, No. 12, dec 2001, pp. R89–R98. [2]
- [21] Yüksel, N., “The Review of Some Commonly Used Methods and Techniques to Measure the Thermal Conductivity of Insulation Materials,” *Insulation Materials in Context of Sustainability*, 2016. [2]
- [22] Parker, W. J., Jenkins, R. J., Butler, C. P., and Abbott, G. L., “Flash Method of Determining Thermal Diffusivity, Heat Capacity, and Thermal Conductivity,” *Journal of Applied Physics*, Vol. 32, No. 9, sep 1961, pp. 1679–1684. [2]
- [23] Ranjith, S., Kallaev, A., and Bakmaev, P., “Thermal-Diffusivity and Heat-Capacity Measurements of Sandstone at High Temperatures Using Laser Flash and DSC Methods,” *International Journal of Thermophysics*, 2015, pp. 658–691. [2]
- [24] Gross, U. and Tran, L.-T.-S., “Radiation effects on transient hot-wire measurements in absorbing and emitting porous media,” *International Journal of Heat and Mass Transfer*, Vol. 47, No. 14-16, jul 2004, pp. 3279–3290. [3]

- [25] Coquard, R., Baillis, D., and Quenard, D., "Experimental and theoretical study of the hot-wire method applied to low-density thermal insulators," *International Journal of Heat and Mass Transfer*, Vol. 49, No. 23-24, nov 2006, pp. 4511–4524. [3]
- [26] Coquard, R. and Baillis, D., "Application of the Hot-Plane Method to Low-Density Thermal Insulators," *Journal of Thermophysics and Heat Transfer*, 2007. [3]
- [27] Coquard, R., Coment, E., Flasquin, G., and Baillis, D., "Analysis of the hot-disk technique applied to low-density insulating materials," *International Journal of Thermal Sciences*, Vol. 65, mar 2013, pp. 242–253. [3]
- [28] Mendes, M. A., Goetze, P., Talukdar, P., Werzner, E., Demuth, C., Rössger, P., Wulf, R., Gross, U., Trimis, D., and Ray, S., "Measurement and simplified numerical prediction of effective thermal conductivity of open-cell ceramic foams at high temperature," *International Journal of Heat and Mass Transfer*, Vol. 102, nov 2016, pp. 396–406. [3, 4, 43, 49]
- [29] Mendes, M. A., Ray, S., and Trimis, D., "An improved model for the effective thermal conductivity of open-cell porous foams," *International Journal of Heat and Mass Transfer*, Vol. 75, aug 2014, pp. 224–230. [3]
- [30] Coquard, R. and Baillis, D., "Numerical investigation of conductive heat transfer in high-porosity foams," *Acta Materialia*, Vol. 57, No. 18, oct 2009, pp. 5466–5479. [3]
- [31] Bracconi, M., Ambrosetti, M., Maestri, M., Groppi, G., and Tronconi, E., "A fundamental analysis of the influence of the geometrical properties on the effective thermal conductivity of open-cell foams," *Chemical Engineering and Processing - Process Intensification*, Vol. 129, jul 2018, pp. 181–189. [3]
- [32] Mendes, M. A., Talukdar, P., Ray, S., and Trimis, D., "Detailed and simplified models for evaluation of effective thermal conductivity of open-cell porous foams at high temperatures in presence of thermal radiation," *International Journal of Heat and Mass Transfer*, Vol. 68, jan 2014, pp. 612–624. [3]
- [33] Loretz, M., Maire, E., and Baillis, D., "Analytical Modelling of the Radiative Properties of Metallic Foams: Contribution of X-Ray Tomography," *Advanced Engineering Materials*, Vol. 10, No. 4, apr 2008, pp. 352–360. [4]
- [34] Wulf, R., Mendes, M., Skibina, V., Al-Zoubi, A., Trimis, D., Ray, S., and Gross, U., "Experimental and numerical determination of effective thermal conductivity of open cell FeCrAl-alloy metal foams," *International Journal of Thermal Sciences*, Vol. 86, dec 2014, pp. 95–103. [4]
- [35] Mendes, M. A., Skibina, V., Talukdar, P., Wulf, R., Gross, U., Trimis, D., and Ray, S., "Experimental validation of simplified conduction–radiation models for evaluation of Effective Thermal Conductivity of open-cell metal foams at high temperatures," *International Journal of Heat and Mass Transfer*, Vol. 78, nov 2014, pp. 112–120. [4]

## Bibliography

---

- [36] Zake-Tiluga, I., Svinka, V., Svinka, R., Zierath, B., Greil, P., and Fey, T., "Thermal conductivity and microstructure characterisation of lightweight alumina and alumina–mullite ceramics," *Journal of the European Ceramic Society*, Vol. 36, No. 6, may 2016, pp. 1469–1477. [4, 48, 49, 50]
- [37] Viskanta, R. and Grosh, R. J., "Heat Transfer by Simultaneous Conduction and Radiation in an Absorbing Medium," *Journal of Heat Transfer*, Vol. 84, No. 1, feb 1962, pp. 63–72. [4]
- [38] Lick, W., "Transient energy transfer by radiation and conduction," *International Journal of Heat and Mass Transfer*, 1965. [4]
- [39] Heinemann, U., Caps, R., and Fricke, J., "Radiation-conduction interaction: an investigation on silica aerogels," *International Journal of Heat and Mass Transfer*, Vol. 39, No. 10, jul 1996, pp. 2115–2130. [4]
- [40] Soufiani, A., Hartmann, J., and Taine, J., "Validity of band-model calculations for CO<sub>2</sub> and H<sub>2</sub>O applied to radiative properties and conductive-radiative transfer," *Journal of Quantitative Spectroscopy and Radiative Transfer*, Vol. 33, No. 3, mar 1985, pp. 243–257. [4]
- [41] Tan, H., Ruan, L., Xia, X., Yu, Q., and Tong, T. W., "Transient coupled radiative and conductive heat transfer in an absorbing, emitting and scattering medium," *International Journal of Heat and Mass Transfer*, Vol. 42, No. 15, aug 1999, pp. 2967–2980. [4]
- [42] Wang, L. S. and Tien, C.-L., "STUDY OF THE INTERACTION BETWEEN RADIATION AND CONDUCTION BY A DIFFERENTIAL METHOD," *Proceeding of International Heat Transfer Conference 3*, Begellhouse, Connecticut, 1966, pp. 190–199. [4]
- [43] Hazzah, A. and Beck, J., "Unsteady combined conduction-radiation energy transfer using a rigorous differential method," *International Journal of Heat and Mass Transfer*, Vol. 13, No. 3, mar 1970, pp. 517–522. []
- [44] Ratzel, A. C. and Howell, J. R., "Heat Transfer by Conduction and Radiation in One-Dimensional Planar Media Using the Differential Approximation," *Journal of Heat Transfer*, Vol. 104, No. 2, 1982, pp. 388. []
- [45] Wu, C.-Y. and Ou, N.-R., "Transient two-dimensional radiative and conductive heat transfer in a scattering medium," *International Journal of Heat and Mass Transfer*, Vol. 37, No. 17, nov 1994, pp. 2675–2686. []
- [46] Li, H., "Estimation of thermal properties in combined conduction and radiation," *International Journal of Heat and Mass Transfer*, Vol. 42, No. 3, feb 1999, pp. 565–572. []
- [47] Wu, J.-W. and Chu, H.-S., "Combined Conduction and Radiation Heat Transfer in Plane-Parallel Packed Beds with Variable Porosity," *Journal of Quantitative Spectroscopy and Radiative Transfer*, Vol. 61, No. 4, mar 1999, pp. 443–452. [4]

- [48] Bergquam, J. B. and Seban, R. A., "Heat Transfer by Conduction and Radiation in Absorbing and Scattering Materials," *Journal of Heat Transfer*, Vol. 93, No. 2, 1971, pp. 236. [4]
- [49] Matthews, L. K., Viskanta, R., and Incropera, F. P., "Combined Conduction and Radiation Heat Transfer in Porous Materials Heated by Intense Solar Radiation," *Journal of Solar Energy Engineering*, Vol. 107, No. 1, 1985, pp. 29. []
- [50] Campo, A. and Tremante, A., "Two-flux model applied to combined conduction-radiation in a gray planar medium," *Wärme- und Stoffübertragung*, Vol. 21, No. 4, jul 1987, pp. 221–225. []
- [51] Siegel, R. and Spuckler, C., "Approximate solution methods for spectral radiative transfer in high refractive index layers," *International Journal of Heat and Mass Transfer*, Vol. 37, mar 1994, pp. 403–413. []
- [52] Andre, S. and Degiovanni, A., "A New Way of Solving Transient Radiative-Conductive Heat Transfer Problems," *Journal of Heat Transfer*, Vol. 120, No. 4, 1998, pp. 943. [4]
- [53] Tremante, A. and Malpica, E., "Analysis of the Temperature Profile of Ceramic Composite Materials Exposed to Combined Conduction–Radiation Between Concentric Cylinders," *Journal of Engineering for Gas Turbines and Power*, Vol. 120, No. 2, 1998, pp. 271. []
- [54] Siegel, R., "Radiative exchange in a parallel-plate enclosure with translucent protective coatings on its walls," *International Journal of Heat and Mass Transfer*, Vol. 42, No. 1, jan 1999, pp. 73–84. [4]
- [55] Doermann, D. and Sacadura, J. F., "Heat Transfer in Open Cell Foam Insulation," *Journal of Heat Transfer*, Vol. 118, No. 1, 1996, pp. 88. [4]
- [56] J. Kowalski, G., "Transient response of an optically thick medium exposed to short pulses of laser radiation," *Fundamentals and Applications in Radiation Heat Transfer*, 1987. []
- [57] Petrov, V. A., "Combined radiation and conduction heat transfer in high temperature fiber thermal insulation," *International Journal of Heat and Mass Transfer*, Vol. 40, No. 9, jun 1997, pp. 2241–2247. [4]
- [58] Lin, J.-D. and Tsai, J.-H., "Transient combined conduction and radiation with anisotropic scattering," *Journal of Thermophysics and Heat Transfer*, Vol. 4, No. 1, jan 1990, pp. 92–97. [4]
- [59] Baek, S. W. and Kim, T. Y., "THE CONDUCTIVE AND RADIATIVE HEAT TRANSFER IN RECTANGULAR ENCLOSURE USING THE DISCRETE ORDINATES METHOD," *Proceeding of International Heat Transfer Conference 9*, Begellhouse, Connecticut, 1990, pp. 433–438. []

## Bibliography

---

- [60] Chung-Jen, T. and Hsin-Sen, C., "Transient combined conduction and radiation in an absorbing, emitting and anisotropically-scattering medium with variable thermal conductivity," *International Journal of Heat and Mass Transfer*, Vol. 35, No. 7, jul 1992, pp. 1844–1847. []
- [61] Kamiuto, K., Iwamoto, M., and Nagumo, Y., "Combined conduction and correlated-radiation heat transfer in packedbeds," *Journal of Thermophysics and Heat Transfer*, Vol. 7, No. 3, jul 1993, pp. 496–501. []
- [62] Baek, S. W., Kim, T. Y., and Lee, J. S., "Transient cooling of a finite cylindrical medium in the rarefied cold environment," *International Journal of Heat and Mass Transfer*, Vol. 36, No. 16, nov 1993, pp. 3949–3956. []
- [63] Jones, P. D., McLeod, D. G., and Dorai-Raj, D. E., "Correlation of Measured and Computed Radiation Intensity Exiting a Packed Bed," *Journal of Heat Transfer*, Vol. 118, No. 1, 1996, pp. 94. []
- [64] Sakami, M., Charette, A., and Le Dez, V., "Application of the discrete ordinates method to combined conductive and radiative heat transfer in a two-dimensional complex geometry," *Journal of Quantitative Spectroscopy and Radiative Transfer*, Vol. 56, No. 4, oct 1996, pp. 517–533. []
- [65] Lee, K. H. and Viskanta, R., "Transient conductive-radiative cooling of an optical quality glass disk," *International Journal of Heat and Mass Transfer*, Vol. 41, No. 14, jul 1998, pp. 2083–2096. []
- [66] H. Lee, K. and Viskanta, R., "Comparison of the Diffusion Approximation and the Discrete Ordinates Method for the Investigation of Heat Transfer in Glass," *Glass Science and Technology-Glastechnische Berichte*, Vol. 72, 1999, pp. 254–265. []
- [67] Park, H., Kim, T., and Lee, J., "Dynamic simulation of thermal radiation in participating media by means of mode reduction," *Journal of Quantitative Spectroscopy and Radiative Transfer*, Vol. 62, No. 2, may 1999, pp. 141–166. []
- [68] Park, H. and Yoon, T., "Solution of the inverse radiation problem using a conjugate gradient method," *International Journal of Heat and Mass Transfer*, Vol. 43, No. 10, may 2000, pp. 1767–1776. [4]
- [69] Hutchison, J. E. and Richards, R. F., "Effect of Nongray Gas Radiation on Thermal Stability in Carbon Dioxide," *Journal of Thermophysics and Heat Transfer*, Vol. 13, No. 1, jan 1999, pp. 25–32. [4]
- [70] Lazard, M., André, S., and Maillet, D., "Transient coupled radiative–conductive heat transfer in a gray planar medium with anisotropic scattering," *Journal of Quantitative Spectroscopy and Radiative Transfer*, Vol. 69, No. 1, apr 2001, pp. 23–33. [4]

- 
- [71] Smith, T. F., Al-Turki, A. M., Byun, K., and Kim, T. K., "Radiative and conductive transfer for a gas/soot mixture between diffuse parallel plates," *Journal of Thermophysics and Heat Transfer*, Vol. 1, No. 1, jan 1987, pp. 50–55. [4]
- [72] Abed, A. A. and Sacadura, J.-F., "A Monte Carlo-finite difference method for coupled radiation-conduction heat transfer in semitransparent media," *ASME Transactions Journal of Heat Transfer*, Vol. 105, 1983, pp. 931–933. [4]
- [73] Kholodov, N. M., Flom, Z. G., and Koltun, P. S., "Calculation of radiative-conductive heat transfer in a semitransparent plate by the Monte Carlo method," *Journal of Engineering Physics*, Vol. 42, No. 3, mar 1982, pp. 333–338. [4]
- [74] Götz, T., "Coupling heat conduction and radiative transfer," *Journal of Quantitative Spectroscopy and Radiative Transfer*, Vol. 72, No. 1, jan 2002, pp. 57–73. [4]
- [75] Petrasch, J., Wyss, P., and Steinfeld, A., "Tomography-based Monte Carlo determination of radiative properties of reticulate porous ceramics," *Journal of Quantitative Spectroscopy and Radiative Transfer*, Vol. 105, No. 2, jun 2007, pp. 180–197. [4, 29]
- [76] Haussener, S., Lipiński, W., Petrasch, J., Wyss, P., and Steinfeld, A., "Tomographic Characterization of a Semitransparent-Particle Packed Bed and Determination of its Thermal Radiative Properties," *Journal of Heat Transfer*, 2009. [4, 29]
- [77] Randrianalisoa, J. and Baillis, D., "Radiative properties of densely packed spheres in semitransparent media: A new geometric optics approach," *Journal of Quantitative Spectroscopy and Radiative Transfer*, Vol. 111, No. 10, jul 2010, pp. 1372–1388. [4]
- [78] Perraudin, D. Y. and Haussener, S., "Numerical quantification of coupling effects for radiation-conduction heat transfer in participating macroporous media: Investigation of a model geometry," *International Journal of Heat and Mass Transfer*, Vol. 112, sep 2017, pp. 387–400. [4]
- [79] Leroy, V., Goyeau, B., and Taine, J., "Coupled Upscaling Approaches For Conduction, Convection, and Radiation in Porous Media: Theoretical Developments," *Transport in Porous Media*, Vol. 98, No. 2, jun 2013, pp. 323–347. [5]
- [80] Lipiński, W., Petrasch, J., and Haussener, S., "Application of the spatial averaging theorem to radiative heat transfer in two-phase media," *Journal of Quantitative Spectroscopy and Radiative Transfer*, Vol. 111, No. 1, jan 2010, pp. 253–258. [5]
- [81] Petrasch, J., Haussener, S., and Lipiński, W., "Discrete vs. continuum-scale simulation of radiative transfer in semitransparent two-phase media," *Journal of Quantitative Spectroscopy and Radiative Transfer*, Vol. 112, No. 9, jun 2011, pp. 1450–1459. [5, 28]
- [82] Wendlandt, B. C. H., "Temperature in an irradiated thermally conducting translucent medium," *Journal of Physics D: Applied Physics*, Vol. 6, No. 6, apr 1973, pp. 308. [5]

## Bibliography

---

- [83] Viskanta, R. and Hirleman, E. D., “Combined Conduction-Radiation Heat Transfer Through an Irradiated Semitransparent Plate,” *Journal of Heat Transfer*, Vol. 100, No. 1, 1978, pp. 169. [5]
- [84] Hahn, O., Raether, F., Arduini-Schuster, M., and Fricke, J., “Transient coupled conductive/radiative heat transfer in absorbing, emitting and scattering media: application to laser-flash measurements on ceramic materials,” *International Journal of Heat and Mass Transfer*, Vol. 40, No. 3, feb 1997, pp. 689–698. [5]
- [85] Heping, T., Maestre, B., and Lallemand, M., “Transient and Steady-State Combined Heat Transfer in Semi-Transparent Materials Subjected to a Pulse or a Step Irradiation,” *Journal of Heat Transfer*, Vol. 113, No. 1, 1991, pp. 166. [5]
- [86] Liu, L., Tan, H., and Tong, T., “Non-Fourier effects on transient temperature response in semitransparent medium caused by laser pulse,” *International Journal of Heat and Mass Transfer*, Vol. 44, No. 17, sep 2001, pp. 3335–3344. [5]
- [87] Duffa, G., *Ablative Thermal Protection Systems Modeling*, American Institute of Aeronautics and Astronautics, Inc., Washington, DC, may 2013. [5]
- [88] Natali, M., Kenny, J. M., and Torre, L., “Science and technology of polymeric ablative materials for thermal protection systems and propulsion devices: A review,” *Progress in Materials Science*, Vol. 84, dec 2016, pp. 192–275. [5]
- [89] Mottram, J. T. and Taylor, R., “Thermal conductivity of fibre-phenolic resin composites. Part I: Thermal diffusivity measurements,” *Composites Science and Technology*, 1987. [5]
- [90] Sykes, G. F., “Decomposition Characteristics of a Char-Forming Phenolic Polymer Used for Ablative Composites,” Tech. rep., NASA TN D-3810, 1967. [5]
- [91] April, G. C., Pike, R. W., and Del Valle, E. G., “Modeling reacting gas flow in the char layer of an ablator,” *AIAA Journal*, Vol. 9, No. 6, jun 1971, pp. 1113–1119. [5]
- [92] Covington, M. A., Heinemann, J. M., Goldstein, H. E., Chen, Y.-K., Terrazas-Salinas, I., Balboni, J. A., Olejniczak, J., and Martinez, E. R., “Performance of a Low Density Ablative Heat Shield Material,” *Journal of Spacecraft and Rockets*, Vol. 45, No. 2, mar 2008, pp. 237–247. [5]
- [93] Cheatwood, F. M., Bose, D., Karlgaard, C. D., Kuhl, C. A., Santos, J. A., and Wright, M. J., “Mars Science Laboratory (MSL) Entry, Descent, and Landing Instrumentation (MEDLI): Complete Flight Data Set,” 2014. [5, 6]
- [94] Meurisse, J. B. E. and Mansour, N. N., “Inverse Determination of Aeroheating and Charring Ablator Response,” *15th Annual International Planetary Probe Workshop*, Boulder, CO; United States, 2018. [5]
- [95] Banerji, N., Leyland, P., and Haussener, S., “Tomography-based radiative characterisation of decomposing carbonaceous heat shield materials,” *Carbon*, 2017. [6, 8, 28]



- [96] Helber, B., Turchi, A., Scoggins, J. B., Hubin, A., and Magin, T. E., "Experimental investigation of ablation and pyrolysis processes of carbon-phenolic ablators in atmospheric entry plasmas," *International Journal of Heat and Mass Transfer*, Vol. 100, sep 2016, pp. 810–824. [6]
- [97] White, S., "Radiation Testing of PICA at the Solar Power Tower," 2012. [6, 84, 90, 95, 100]
- [98] Lachaud, J., Magin, T. E., Cozmuta, I., and Mansour, N. N., "A Short Review of Ablative-Material Response Models and Simulation Tools," *7th Aerothermodynamics Symposium*, European Space Agency, 2011. [6]
- [99] Mora-Monteros, J., Suter, C., and Haussener, S., "Internal Radiation Effects on the Thermal Response of Highly Porous Materials in Radiative Environment," *9th International Symposium on Radiative Transfer*, Athens, 2019. [8]
- [100] Bader, R., Schmidt, L., Haussener, S., and Lipiński, W., "A 45 kWe Multi-Source High-Flux Solar Simulator," 2014. [9]
- [101] Bader, R., Haussener, S., and Lipinski, W., "Optical Design of Multisource High-Flux Solar Simulators," *Journal of Solar Energy Engineering*, Vol. 137, No. April, 2015, pp. 021012. [9, 10, 31, 39]
- [102] Levêque, G., Bader, R., Lipiński, W., and Haussener, S., "Experimental and numerical characterization of a new 45 kWel multisource high-flux solar simulator," *Optics Express*, Vol. 24, No. 22, 2016, pp. A1360–A1373. [9, 10, 11, 39]
- [103] Krueger, K. R., Lip, and Davidson, J. H., "Operational Performance of the University of Minnesota 45kWe High-flux Solar Simulator," *Journal of Solar Energy Engineering*, 2013. [10]
- [104] Sarwar, J., Georgakis, G., LaChance, R., and Ozalp, N., "Description and characterization of an adjustable flux solar simulator for solar thermal, thermochemical and photovoltaic applications," *Solar Energy*, 2014. [10]
- [105] Haussener, S., Fahy, E. J., Mora-Monteros, J., Sturzenegger, P., and Gonzenbach, U. T., "Lightweight Ceramic Foam Composites and Novel Environmental Testing for Satellite Applications," Tech. rep., Ecole Polytechnique Federale de Lausanne, Lausanne, 2017. [13]
- [106] Mora-Monteros, J., Leyland, P., Haussener, S., Mischler, S., and Gonzenbach, U. T., "Ceramic Foams for High Temperature Applications in Space and Energy Storage and Conversion Applications," Tech. rep., Ecole Polytechnique Federale de Lausanne, Lausanne, 2016. [13]
- [107] Mora-Monteros, J., Suter, C., and Haussener, S., "Effective conductivity of porous ceramics in a radiative environment," *Submitted to Ceramics International*. [14, 39]

## Bibliography

---

- [108] S. Touloukian, Y. and P. Dewitt, D., *Thermal radiative properties: Nonmetallic solids.*, Vol. 8, feb 1972. [16, 54, 55]
- [109] “Verre and Quartz Technologies SA,” 2017. [17]
- [110] Bottin, B., Chazot, O., Carbonaro, M., van der Haegen, V., and Paris, S., “The VKI Plasma-tron Characteristics and Performance,” *RTO AVT Course on Measurement Techniques for High Enthalpy and Plasma Flows, Rhode-Saint-Genèse (Belgium), RTO EN-8*, 1999. [18]
- [111] Lachaud, J. and Mansour, N. N., “Porous-Material Analysis Toolbox Based on Open-FOAM and Applications,” *Journal of Thermophysics and Heat Transfer*, Vol. 28, No. 2, apr 2014, pp. 191–202. [23]
- [112] Puiroux, N., Prat, M., and Quintard, M., “Non-equilibrium theories for macroscale heat transfer: ablative composite layer systems,” *International Journal of Thermal Sciences*, Vol. 43, No. 6, jun 2004, pp. 541–554. [24]
- [113] Ene, H. and Sanchez-Palencia, E., “On thermal equation for flow in porous media,” *International Journal of Engineering Science*, Vol. 20, No. 5, jan 1982, pp. 623–630. [24]
- [114] Tancrez, M. and Taine, J., “Direct identification of absorption and scattering coefficients and phase function of a porous medium by a Monte Carlo technique,” *International Journal of Heat and Mass Transfer*, 2004. [29]
- [115] Modest, M. F., *Radiative Heat Transfer*, Elsevier, 2013. [29]
- [116] Gonzenbach, U. T., Studart, A. R., Steinlin, D., Tervoort, E., and Gauckler, L. J., “Processing of Particle-Stabilized Wet Foams Into Porous Ceramics,” *Journal of the American Ceramic Society*, Vol. 90, No. 11, sep 2007, pp. 3407–3414. [39]
- [117] OpenFOAM, “OpenFOAM - The Open Source CFD Toolbox - User Guide,” Tech. rep., 2014. [42]
- [118] Shimizu, T., Matsuura, K., Furue, H., and Matsuzak, K., “Thermal conductivity of high porosity alumina refractory bricks made by a slurry gelation and foaming method,” *Journal of the European Ceramic Society*, Vol. 33, No. 15-16, dec 2013, pp. 3429–3435. [47, 48, 49]
- [119] Shackelford, J. F. and Alexander, W., *Materials Science and Engineering Handbook, Third Edition*, 2010. [48, 49, 50, 54]
- [120] Barea, R., Osendi, M. I., Ferreira, J. M., and Miranzo, P., “Thermal conductivity of highly porous mullite material,” *Acta Materialia*, Vol. 53, No. 11, jun 2005, pp. 3313–3318. [48, 49, 50]
- [121] Litovsky, E., Shapiro, M., and Shavit, A., “Gas Pressure and Temperature Dependences of Thermal Conductivity of Porous Ceramic Materials: Part 2, Refractories and Ceramics with Porosity Exceeding 30%,” *Journal of the American Ceramic Society*, Vol. 79, No. 5, may 1996, pp. 1366–1376. [48]

- [122] Pelissari, P. I., Angélico, R. A., Salvini, V. R., Vivaldini, D. O., and Pandolfelli, V. C., “Analysis and modeling of the pore size effect on the thermal conductivity of alumina foams for high temperature applications,” *Ceramics International*, Vol. 43, No. 16, nov 2017, pp. 13356–13363. [48]
- [123] Reimer, T., Zuber, C., Rieser, J., and Rothermel, T., “Determination of the Mechanical Properties of the Lightweight Ablative Material Zuram,” John Wiley & Sons, feb 2018, pp. 311–326. [71]
- [124] Magnin, V., Mischler, S., Mora-Monteros, J., and Leyland, P., “Material Characterisation Protocol and Characterisation Results (AblaRadAbla TR3),” Tech. rep., 2018. [77]
- [125] Turchi, A., Torres, F., and Magin, T., “Ablation and radiation in the presence of light ablators: Consolidated ablative material database package (AblaRadAbla TR5),” Tech. rep., Von Karman Institute, 2018. [81]
- [126] Scoggins, J. B. and Magin, T. E., “Development of Mutation++: MUlticomponent Thermodynamics And Transport properties for IONized gases library in C++,” *11th AIAA/ASME Joint Thermophysics and Heat Transfer Conference*, Atlanta, 2014, pp. 1–15. [82]
- [127] Banerji, N., *The effects of radiation on ablative heat shields during atmospheric entry*, Ph.D. thesis, 2017. [84]
- [128] Mora-Monteros, J., Leyland, P., Mischler, S., Turchi, A., and Fagnani, A., “Ablation code validation (AblaRadAbla TR9),” Tech. rep. [91]

## Jérémy Mora-Monteros

Address: Chemin de la Comba 10, 1616 Attalens  
Mobile: 076 819 09 89  
Email : j.moramonteros@gmail.com

Date of Birth: 09.09.1989  
Nationality: French  
Civil status: Married with two children

---

PhD in energy and Master of Science in Mechanical Engineering at EPFL.

Perseverance, flexibility and creativity highlighted by developing coupled numerical-experimental tools for an engineering approach to research. Excellent organization and communication skills enhanced by working on collaborative international projects. Ability to work under pressure strengthened by managing multiple projects at once.

---

### Work experience

#### **PhD in energy at EPFL in the laboratory LRESE, Lausanne. 2015-2019**

- Development of coupled experimental-numerical approach for the evaluation of thermal properties of high temperature porous materials, based on an OpenFOAM toolbox (PATO)
- Development of a coupled radiation-conduction algorithm based on the Monte-Carlo method
- Provided guidelines for the choice of the method to evaluate temperature field in porous materials in radiating environment
- Design of experimental procedures in the High Flux Solar Simulator (HFSS) at LRESE
- Material testing to reconcile numerical data with experimental measurements
- Design of Borosilicate vacuum chamber in collaboration with a glass blowing company in order to perform experiment in the HFSS under a controlled atmosphere
- Supervisor for master students in projects that I developed

#### **Research engineer at Interdisciplinary Aerodynamics Group, EPFL, Lausanne. 2012-2015**

- Worked on the atmospheric re-entry of space vehicles for inter-planetary missions. Experience in ablation, radiation, aerothermodynamics, material testing and re-entry physics.
- Focus on numerical simulations of plasma flow around space capsules, and thermochemical response of thermal protection system material

#### **Engineering internship at Osmoblue, EPFL campus, Lausanne. 2014**

- Design of experimental procedures
- Evaluation of range of measurement and uncertainty of flow-meters
- Assembly of prototype to convert industrial waste heat into electricity

#### **Research internship at Center for Hypersonics, The University of Queensland, Brisbane, Australia. 2012-2013**

- Testing under vacuum of a hemicylindrical steel model heated by the Joule effect, to develop a protocol for a successful experimental campaign in the X2 expansion tunnel. Conducted testing under vacuum, learnt to operate expansion tunnel, post-processed resultant radiation spectra.

### Education

Swiss Federal Institute of Technology (EPFL), PhD in energy 2015-2019

Swiss Federal Institute of Technology (EPFL), master in mechanics 2011-2014

Swiss Federal Institute of Technology (EPFL), bachelor in mechanics 2009-2011

Intensive two-year courses preparing for the competitive entrance examinations to the French 'Grandes Ecoles', Lycée du Parc, Lyon, France 2007-2009

French Scientific Baccalaureate, Lycée du Mont-Blanc, France 2004-2007

<b>Publications</b>	<b>Journal articles:</b>	
	Mora-Monteros, J., Suter, C., and Haussener, S., "Effective conductivity of porous ceramics in a radiative environment," accepted in <i>Ceramics International</i> .	<b>2019</b>
	Mora-Monteros, J., Suter, C., and Haussener, S., "Radiation effects on the thermal response of highly porous materials in radiative environment," in preparation	<b>2019</b>
	<b>Conference proceedings:</b>	
	Mora-Monteros, J., Suter, C., and Haussener, S., "Internal Radiation Effects on the Thermal Response of Highly Porous Materials in Radiative Environment," <i>9th International Symposium on Radiative Transfer</i> , Athens.	<b>2019</b>
	Mora-Monteros, J., Leyland, P., Hannema, G., Sheikh, U., Fahy, E., Morgan, R., and McIntyre, T., "Analysis and rebuilding of experiments on a heated carbon graphite model in the X2 expansion tube," <i>46th AIAA Thermophysics Conference. 46th AIAA Thermophysics Conference, Washington, DC, United States</i>	<b>2016</b>
<b>Extra-professional activities</b>	Mora-Monteros, J., Fahy, E., Banerji, N., Joiner, N., Duffa, G., and Leyland, P., "Rebuilding Thermal Response and Ablation Radiation Coupling for Superorbital Return," <i>8th European Symposium on Aerothermodynamics for Space Vehicles, Lisbon, Portugal</i>	<b>2015</b>
	Mora-Monteros, J., Fahy, E., Banerji, N., and Leyland, P., "Ablation Radiation Coupling for the Hayabusa Trajectory," <i>6th International Workshop on Radiation of High Temperature Gases in Atmospheric Entry, St Andrews, UK</i>	<b>2014</b>
	<b>2017-now</b>	
<b>Hard skills</b>	<b>Player-coach of ice-hockey at amateur level</b>	
	<ul style="list-style-type: none"> <li>Organized on and off-ice practices to help the team improve</li> <li>Improvement of my team management skills and leadership</li> </ul>	
	<b>Simulation software</b>	OpenFOAM, CFD++, basics in ANSYS Fluent
	<b>CAD tools</b>	Solidworks and Catia
	<b>Programming</b>	Python, Fortran, c++, MPI standards, Matlab, basics in Labview
	<b>Equipment</b>	High Flux Solar Simulator (Custom made), Infrared Camera (FLIR), Charge-coupled device (CCD) camera, Vacuum setups, Thermogravimetric Analysis (TGA, Perkin Elmer)
<b>Languages</b>	<b>Others</b>	Microsoft office, Linux distributions
	French	mother tongue
	English	fluent, presentation in international conferences, collaboration in international projects